UNIQUE CLUSTER EXPANSION FOR RELIABLE FIRST-PRINCIPLES PREDICTION OF ALLOY THERMODYNAMICS AND PHASE DIAGRAMS

BY

TECK LEONG TAN

DISSERTATION

Submitted in partial fulfillment of the requirements
for the degree of Doctor of Philosophy in Materials Science and Engineering
in the Graduate College of the
University of Illinois at Urbana-Champaign, 2011

Urbana, Illinois

Doctoral Committee:

Professor Duane D. Johnson, Chair
Professor Pascal Bellon
Assistant Professor Dallas Trinkle
Professor Jian-Min Zuo

ABSTRACT

A theoretical multi-scale approach based on the cluster expansion (CE) has been developed to aid materials design and discovery for scientific and engineering applications. Using structural energies from first-principles electronic theory, an effective (CE) Hamiltonian that is suitable for large scale systems is constructed, enabling the calculation of thermodynamic quantities and prediction of phase diagrams. The CE Hamiltonian is expanded in terms of correlation functions of all geometric cluster entities on a fixed lattice, forming a basis set that spans the entire alloy configuration space on the lattice. The coefficients in the CE are the system's effective cluster interactions (ECI), which are physically well-defined and have unique values for each alloy system.

Yet the CE is useful only when the ECI are truncated, permitting the ECI to be obtained from known energies in a configuration subspace. Such ECI are biased by those ECI not in the truncated set, because when projected onto an arbitrarily selected subspace (by truncation), linear dependencies exist between cluster functions. The dependencies are overlooked in current methods, resulting in non-unique truncated CE sets that are extracted from an unnecessarily large number of first-principles data.

In fact, the CE is directly related to the well-studied Walsh transformation and the Hadamard matrices, whose properties are utilized in fractional factorial design principles (also known as Design of Experiment) to evaluate reliably the variables from only a selected subset of known data. Via these concepts, we develop a systematic choice of configuration subspaces that identify clearly the linear dependencies, allowing a unique truncation of CE that keeps the critical ECI. These concepts lead to the subspace projection (SSP) method, which gives a physically and mathematically sound approach to select a unique alloy CE via structural inversion (SI), starting from a subset of known energies evaluated from first-

principles methods such as Density Functional Theory (DFT).

In contrast, current methods for optimally truncated CE set are based on some "chosen" statistical measure of predictive capability of structural energies. This leads to non-unique truncated CE sets, although the issue, as we had shown, is partially addressed when the CE basis is enforced to be compact and locally complete. The theoretical methods we proposed were implemented in the Thermodynamics Toolkit (TTK). We use TTK to construct a CE for various phase-segregating and ordering alloys via SI, using DFT-determined structural energies from a selected set of ordered structures as input. The optimal CE set is used in Monte Carlo (MC) simulations and/or mean-field theories (MFTs) to construct temperature-composition phase diagrams for FCC Ca-Sr, Pd-Rh and Ag-Au (ordering), explaining various features and comparing them to available experiment data. The ECI of Ag-Au system also compare well to those extracted directly from the DFT electronic charge density at the dilute limit, elucidating their electronic structure origins. We also use our SSP method to construct a CE for Ag-Au to illustrate how critical ECI become systematically linearly independent with augmentation of configuration subspaces. Importantly, with only one-third the number of DFT structural energies to extract ECI, we achieve a unique and physical set of ECI via SSP, significantly reducing the amount of computational effort required.

Lastly, a cluster-based MFT, generalized to arbitrary cluster sizes, is introduced to serve as a quick and reliable way to calculate phase diagram. Via a cluster-lattice Fourier transform, the cluster MFT obeys self-consistent relations between cluster and coarse-grained lattice correlations. Already with a single-site cluster, the proposed MFT results in topologically correct phase diagrams for Ising models on frustrated systems, which traditional MFTs fail to achieve. Phase transition temperatures from MC and series expansion are recovered upon finite-size scaling. Together these techniques permit a rapid, unique and reliable approach to materials characterization, design and discovery. In the future we will apply these novel methods and tool to more complex alloy systems.

To my family.

ACKNOWLEDGMENTS

This work would not have been possible without the valuable guidance of Professor Duane D. Johnson and Doctor Nikolai Zarkevich, and valuable feedbacks and support from Professors Pascal Bellon, Dallas Trinkle and Jian-Min Zuo. I particularly thank Professors David E. Goldberg and Michael Stone for helpful and extended discussions leading to the subspace projection method, Professor Vasyl Tokar and Doctor Thomas Maier for clarifying ideas related to the Dynamical Cluster Approximation and improved mean-field theories. I sincerely thank Doctors Lin-Lin Wang, Thierry Auger, Kumara Sastry and Mr. Jonas Funke for extending and helping out with the Thermodynamic ToolKit (TTK) software that performs cluster expansion and Monte Carlo simulations. I also extend my heartfelt appreciation to an incomplete list of people, including my fellow and ex-group members, Suffian Khan, Aftab Alam, Dominic Biavia, Jason Reich, Dan Finkenstadt and Brent Kraczek, whom I learnt a lot from via daily exchanges, professors who had taught me, secretaries in the Department of Materials Science and Engineering, and my group of friends who had made this a more enjoyable process.

I acknowledge financial support in part from National Science Foundation through grant DMR-0705089, the Materials Computation Center at the University of Illinois through DMR-0325939 and a Computational Sciences and Engineering Fellowship at the University of Illinois.

TABLE OF CONTENTS

LIST OF ABBREVIATIONS

BZ: Brillouin Zone

BCC or bcc: Body-centered Cubic

cDMFT: Cellular Dynamical Mean-field Theory

CE: Cluster Expansion

CG: Coarse-grain

CV: Cross-validation

DCA: Dynamical Cluster Approximation

DFT: Density Functional Theory

ECI: Effective Cluster Interactions

FCC or fcc: Face-centered Cubic

GGA: Generalized Gradient Approximation

LDA: Local Density Approximation

LRO: Long-range Order

MC: Monte Carlo

MFT: Mean-field Theory

SI: Structural Inversion

SRO: Short-range Order

T: Temperature

$\mathbf{T_c}$: Order-Disorder Transition Temperature

TTK: Thermodynamics Toolkit

VASP: Vienna Ab-initio Simulation Package

CHAPTER 1

INTRODUCTION

Alloy phase diagrams are of great use in materials design for both scientific and engineering purposes. In science and engineering applications, the desired material properties are often not achievable with a single pure element alone. By combining two or more elements in different ratios, alloyed materials can be designed and tuned to meet specific requirements. Examples are rife in the real world; the addition of carbon in iron to make steel with high strength, the alloying of tin and lead for low-temperature solders, the alloying of semiconductor elements to design LEDs of different colors, etc. Moreover, materials are designed to operate in certain conditions, e.g., under certain temperature and pressure. It is thus important to know if the intended phase of an alloy is stable in the given conditions, otherwise a change in phase would result in a property change, compromising the original design requirement. Alloy phase diagrams thus comes in handy to indicate the thermodynamically stable phases for a given temperature and pressure, and these stable phases are expected to last for a long time.

Conventionally, alloy phases are constructed from experimental input (e.g., via CALPHAD methods [1]), and the process is expensive and time consuming. Given the huge combinatorial possibilities of alloying different elements, it is not surprising that only a small fraction (mainly binary alloys) of conceivable alloy phase diagrams are determined. Moreover, low-temperature phases are often inaccessible experimentally due to slow kinetics. As such it is of great interest to develop computational methods capable of producing reliable alloy phase diagrams *without* any experimental input, thus speeding up the process of materials design and discovery.

In this work we detail a computational method that creates an effective alloy Hamiltonian using the cluster expansion (CE) basis [2], starting from a selected set of first-principles

structural energies. The CE Hamiltonian is utilized in statistical simulations to efficiently and reliably compute thermodynamic quantities for constructing phase diagrams in the solid state. The CE method is an evolving research area and has been actively applied to various alloys [2–24]. To show its validity and usefulness, the CE method is applied in this work to study a class of phase-segregating metallic alloys and the ordering system. Given an alloy system, the issue of uniqueness in the CE interactions is often overlooked by the community. We show that the truncated CE basis approaches a unique set, only when important basis set coefficients (i.e., cluster interactions) are independent via appropriate choice of clusters (arranged in a physics-based hierarchy) and structural subspace; this results in reliable alloy energetics while keeping minimal the number of first-principles structural energies utilized. Keeping in mind that we are interested in the solid state part of the alloy phase diagram, we first define some rudimentary terms and concepts common to metallic alloys and their phase diagrams.

1.1 Phase Diagram Essentials

A metallic alloy is a mixture or solution (either liquid or solid) of two or more metallic elements, which are also called the *components* of the alloy. The ratio of the number of atoms for a given component to the total number of atoms in the alloy system is called the *composition* or *concentration*. In a solid solution, the atoms of the minority component (solute) are mixed with or 'dissolved' into the majority component (host), either via substituting a position originally occupied by the host atom (e.g., A_xB_{1-x}) or via inserting into interstitial positions between host atoms, in which case an originally vacant interstitial site is substituted by a solute (e.g., $A_x\square_{1-x}B$).

Defining a *phase* to be a homogenous region in a materials system with uniform physical and chemical characteristics, a solid solution forms a single phase which can either be *ordered* or *disordered*. In a disordered solution, the solute atoms are randomly arranged among the host atoms with no long-range order. In an ordered solution, there is a perceived long-range order and the solute atoms are arranged in a certain fixed spatial pattern with respect to the host atoms. When the compositions of components are comparable, the distinction

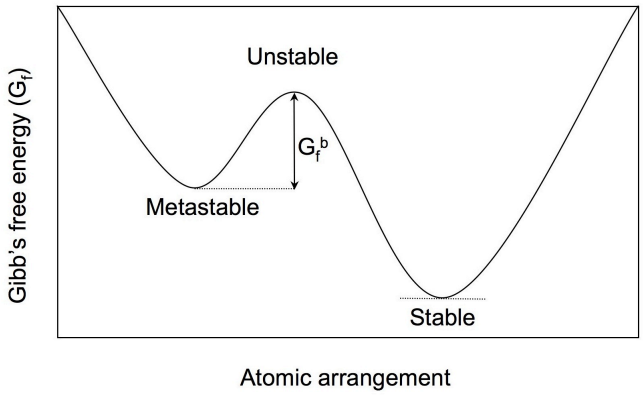

Figure 1.1: Illustration of stable, metastable and unstable states of equilibrium using G_f v.s. atomic arrangement. G_f^b is the activation barrier.

between solute and host blurs out, and such solutions are called *intermediate phases*. An intermediate phase, both ordered and disordered, can remain homogeneous across a composition range. When an ordered phase has no or limited homogeneity range and is centered about a fixed stoichiometric composition, they are called *intermetallic compounds*.

The concept of equilibrium and stability for an alloy system is described using the thermodynamic quantity Gibb's free energy,

$$G_f = E + PV - TS \quad , \tag{1.1}$$

where E is the internal energy of the alloy system, P is the pressure, V is the volume, T is the absolute temperature and S is the entropy. Figure 1.1 illustrates three states of equilibrium: stable, metastable and unstable, where dG_f=0. At stable or metastable equilibrium, G_f corresponds to a minima and the equilibrium atomic arrangement is stable with respect to small perturbations. The opposite happens for an unstable equilibrium (maxima). Although locally stable, a metastable state can achieve the truly stable atomic arrangement when additional energy is supplied to overcome the activation barrier, G_f^b.

In most cases, an alloy phase diagram shows the relationship between *stable* phases subject to changes in state variables such as temperature (T) and composition (c). For alloys, it is customary to show the thermodynamically stable phases on a T-c phase diagram

with pressure fixed at 1 atmosphere [25]. A thermodynamically stable phase is one which has reached stable equilibrium state and will remain so 'forever', under a given T and c. Because

$$dE = TdS - PdV + \sum_i \mu_i dN_i \quad , \tag{1.2}$$

where μ_i is the chemical potential associated with the N_i atoms from component i, the total differential of G_f (from (1.1)) is,

$$dG_f = -SdT + VdP + \sum_i \mu_i dN_i \quad . \tag{1.3}$$

An alloy system would always change to lower its Gibb's free energy, hence dG_f is necessary zero (corresponding to a minima) for a stable system, which, from (1.3), is indeed the case at fixed T, P and c. Phases can also coexist in thermodynamic equilibrium and the degree of freedom, f, of such region in the T-c phase diagram (at fixed P) is determined by the Gibb's phase rule,

$$f = n_c - n_p + 1 \quad , \tag{1.4}$$

where n_c is the number of components and n_p is the number of coexisting phases. For binary alloy phase diagrams ($n_c = 2$), a single phase ($n_p = 1$) has 2 degrees of freedom and is thus defined by an area in the T-c diagram. Two-phase regions ($f = 1$) and three-phase regions ($f = 0$) are thus defined by lines and points respectively.

1.2 Crystal Structures

Many alloys exist as *crystalline* solids, where the atomic positions are repeated infinitely in space in a well-defined spatial pattern. This repetition is described by the *lattice* − a collection of points in space constructed by repeating infinitely a set of *translation vectors* $\{\mathbf{a}_1, ..., \mathbf{a}_d\}$, where d is the dimensionality. Thus for a 3-D lattice, a lattice point, p, is

located by

$$\mathbf{r}_p = l\mathbf{a}_1 + m\mathbf{a}_2 + n\mathbf{a}_3 \quad , \tag{1.5}$$

with l, m, n being any integer between $-\infty$ and ∞. To describe a crystal system, one would need a lattice and a *basis*; a basis is a finite set of sites whose coordinates are defined with respect to a lattice point, forming a unit cell. This unit cell is repeated infinitely using (1.5) to generate the crystal. Of great importance, is the symmetry group a crystal belongs to. A 3-D crystal with primitive unit cell, i.e., one that contains only a single site, has to belong to 1 of the 14 possible Bravais lattice [26], where each Bravais lattice satisfy a unique set of symmetry operations . Phases of metals and their alloys, are commonly found to be in the face-centred cubic (fcc), body-centred cubic (bcc) or hexagonal-closed-pack (hcp) crystal structure. Both fcc and bcc are primitive lattices while hcp requires a 2-site basis.

Associated with each real space lattice is a reciprocal space lattice, whose translation vectors can be constructed from $\{\mathbf{a}_1, \mathbf{a}_2, \mathbf{a}_3\}$,

$$\mathbf{a}_i^* = 2\pi \frac{\mathbf{a}_j \times \mathbf{a}_k}{\mathbf{a}_i \cdot (\mathbf{a}_j \times \mathbf{a}_k)} \quad , \forall i = 1, 2, 3 \quad , \tag{1.6}$$

where $j = (i \mod 3) + 1$ and $k = [(i+1) \mod 3] + 1$. The reciprocal space is useful for direct comparison with structural data from X-ray diffraction experiments [27], where for a primitive lattice, Bragg spots will only be observed at the reciprocal lattice points,

$$\mathbf{r}_p^* = h\mathbf{a}_1^* + k\mathbf{a}_2^* + l\mathbf{a}_3^* \quad , \tag{1.7}$$

with h, k, l being integers. It is interesting to note that the fcc lattice in real space becomes bcc in reciprocal space and vice-versa.

Occupation variables: In addition to knowing the crystal structure, one would also need to know the atomic occupation at each of the crystal site to completely describe an alloy structure. In the general case of a P-component alloy, each lattice site is occupied by only one of the P atomic types. Using *occupation* variables, ξ_p^α=1 if site p is occupied by

atomic type α and 0 otherwise. The atomic type, α, can represent a true element from the periodic table (e.g., Cu or Au in Cu-Au alloy system) or entities such as vacancies in defect studies. For a fixed site in a P-component alloy structure,

$$\sum_{\alpha}^{P} \xi_p^{\alpha} = 1 \quad , \tag{1.8}$$

hence there are only P − 1 independent occupation variables for any given site. Each *configuration* is then a certain ordering of P atomic types on the lattice and can be represented by a set of occupation variables $\{\xi_p^{\alpha}\}$. An alternative and equally valid representation using *spin* variables, σ_p, which enables the construction of orthogonal cluster expansion basis [2] (via Chebyshev polynomials), is discussed in the next chapter. For a binary alloy (P=2) where each lattice site is either occupied by A or B atomic type, $\xi_p^A = 1(0)$, while $\sigma_p = 1(-1)$, when A(B) occupies lattice site p.

The concept of derivative lattice or *superlattice* [28] is used in our work to generate alloy structures. Given a lattice, such as fcc, one can derive a new alloy structure by first defining three non-parallel vectors of the form in (1.5) as translation vectors, which are also used to construct a parallelepiped unit cell; such unit cells are called *supercells* and atomic types are assigned to each site in the cell. The supercells are thus repeated using,

$$\mathbf{r}_{\text{cell}} = L\left(l_1\mathbf{a}_1 + m_1\mathbf{a}_2 + n_1\mathbf{a}_3\right) + M\left(l_2\mathbf{a}_1 + m_2\mathbf{a}_2 + n_2\mathbf{a}_3\right) + N\left(l_3\mathbf{a}_1 + m_3\mathbf{a}_2 + n_3\mathbf{a}_3\right) \quad , \tag{1.9}$$

with L, M, N being integers between $-\infty$ and ∞. The ordering of atoms is thus repeated infinitely, giving rise to long-range order. Some examples of derived fcc structures are shown in Figure 1.2 for an A-B alloy, labelled using *Strukturbericht* designation. The translation vectors, which are also used to form a parallelepiped unit cell, are shown with arrows. The A_1 structure is essentially the primitive fcc lattice because all sites are occupied by single elements (pure A or B). A possible structure for an AB compound is the $L1_0$ structure, constructed by a 2-site (body-centered tetragonal) supercell, with one site occupied by A and the other by B. Each supercell site individually forms a sublattice, when its is infinitely

repeated with the supercell vectors. The $L1_0$ structure can thus be described as composing of two interpenetrating (tetragonal) sublattices, one completely occupied by A and the other by B. Two possible structures for AB_3 are $L1_2$ and DO_{22}, whose translation vectors are different (hence different supercell shapes). Despite having the same composition and four sublattices, the two structures exhibit different long range order, have different symmetries and typically give different energies. In addition, *frustration* in ordering is often encountered in closed pack lattices such as fcc and hcp. For example in the case of AB alloy, there is no way of arranging the atoms such that no A atoms are of nearest neighbor to each other (see $L1_0$ structure in fig. 1.2) while this is possible for a bcc lattice. Frustration often results in more competing phases and hence, phase diagrams with richer features, even when interactions are short-range.

Long-range order: To characterize the long-range order (LRO), a one-site correlation function, which quantifies the site-dependent concentration fluctuation, is often used:

$$\begin{aligned} \delta c_p^\alpha &= c_p^\alpha - \bar{c}^\alpha \\ &\equiv \left\langle \xi_p^\alpha \right\rangle - \frac{1}{N_q} \sum_q^{N_q} \left\langle \xi_q^\alpha \right\rangle \quad , \end{aligned} \tag{1.10}$$

where c_p^α is the concentration of α at site p, given by the thermodynamic average of ξ_p^α and is a function of temperature, T; $\bar{c}^\alpha$ is the average concentration of α for the entire alloy system consisting of N_q sites. At T=0, perfect LRO exists and hence,

$$\delta c_p^\alpha (T=0) = \begin{cases} 1 - \bar{c}^\alpha, & \text{if } p \in \alpha\text{-rich sublattice} \\ -\bar{c}^\alpha, & \text{otherwise.} \end{cases} \tag{1.11}$$

This sets an upper-bound (lower-bound) for δc_p^α at the α-rich (α-depleted) sublattice. In relation to diffraction experiments, it is pertinent to expressed δc_p^α as concentration waves [29] to describe the periodicity of atomic occupation; the wave vectors are related to 'new' satellite reflections (in addition to the usual Bragg spots from the underlying lattice structure of the disordered A_1 phase, see Figure 1.2).

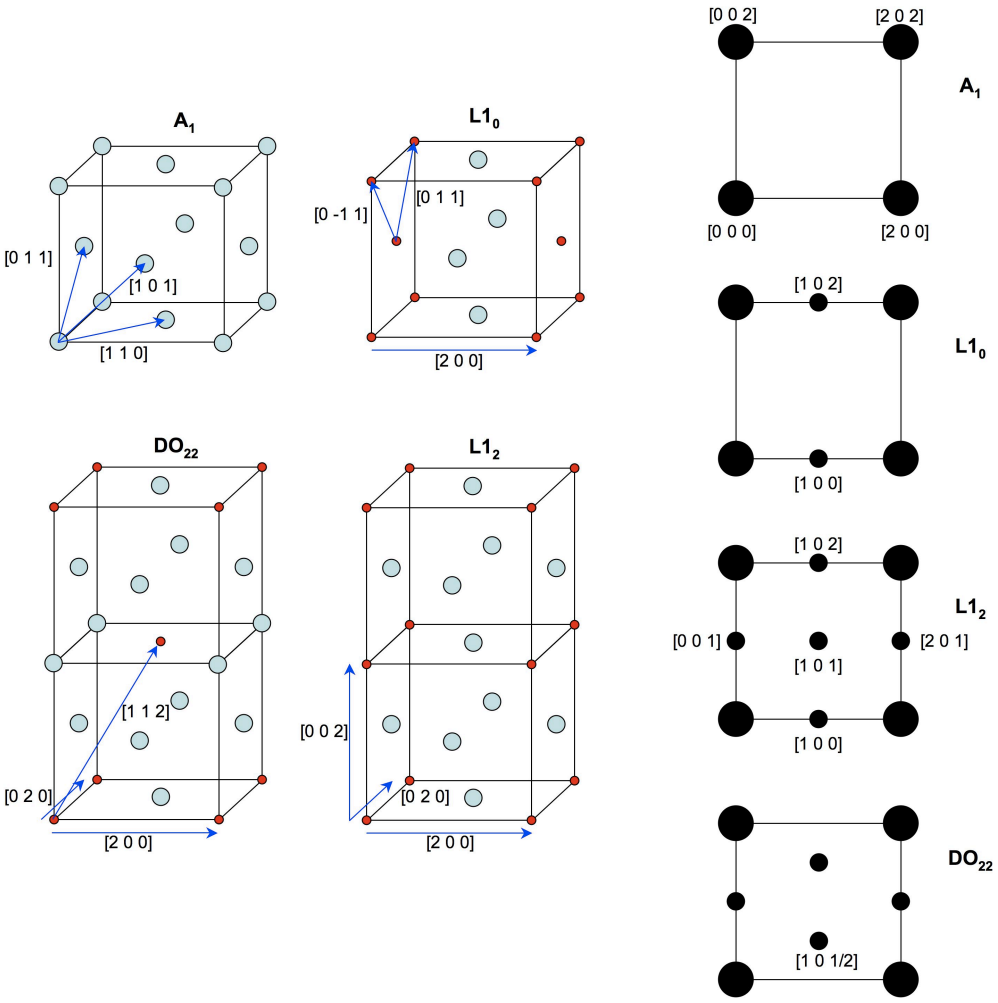

Figure 1.2: Examples of binary alloy structures derived from fcc lattice, labelled using *Strukturbericht* designation, along with diffraction spots in the reciprocal space (right column). The translation vectors are labelled and drawn as arrows. The A_1 structure is that of single-component phases or completely disordered phase, and is essentially the primitive fcc lattice. The A_1 structure results in Bragg spots (big spots) in the reciprocal space (at bcc lattice sites). Additional satellite reflections (small spots), which are indicative of long-range ordering, are observed for $L1_0$, $L1_2$ and DO_{22} structures.

Short-range order: Typically for a structure with a given LRO, one can define a order-disorder transition temperature, T_c, above which the LRO is lost, i.e., $\delta c_p^\alpha \to 0$ regardless of site p and for all α, resulting in a disordered (A_1) phase. However, the disordered phase still exhibits short-range order (SRO), which can be characterized by the Warren-Cowley SRO parameters [27, 30, 31],

$$\alpha_{pq}^{\alpha\beta} = \frac{\left\langle \xi_p^\alpha \xi_q^\beta \right\rangle - c_p^\alpha c_q^\beta}{\bar{c}^\alpha \left(\delta_{\alpha\beta} - \bar{c}^\beta\right)} \quad , \tag{1.12}$$

where the numerator is a two-site correlation function that quantifies the thermodynamically averaged pair correlation beyond the uncorrelated part (complete disorder), $c_p^\alpha c_q^\beta$; the denominator, which gives the correlation at complete disorder, serves as a normalizing factor. At complete disorder ($T \to \infty$), ξ_p^α and ξ_q^β are uncorrelated for $p \neq q$, hence $\left\langle \xi_p^\alpha \xi_q^\beta \right\rangle \to c_p^\alpha c_q^\beta$ and $\alpha_{pq}^{\alpha\beta} = 0$. For the disordered phase ($T > T_c$), it is noted that as $|\mathbf{r}_p - \mathbf{r}_q| \to \infty$, we have $\alpha_{pq}^{\alpha\beta} \to 0$, as opposed to non-zero values for LRO phases ($T < T_c$). To facilitate comparison with diffuse scattering experiments, the SRO parameter is Fourier transformed,

$$\alpha^{\alpha\beta}(\mathbf{k}) = \sum_q^{N_q} \alpha_{pq}^{\alpha\beta} \exp i\mathbf{k}(\mathbf{r}_q - \mathbf{r}_p) \quad , \tag{1.13}$$

where $\alpha_{pq}^{\alpha\beta}$ depends only on the difference in the lattice site coordinates $\mathbf{r}_p - \mathbf{r}_q$ (as given in (1.5)) in the disordered phase. Because the SRO intensity is proportional to the difference in the scattering factor of the atomic types α and β, $\alpha_{pq}^{\alpha\beta}$ is measurable only when $\alpha \neq \beta$. In addition, $\alpha_{pp}^{\alpha\beta} = 1$ (regardless of α and β) from (1.12). Hence, the Fourier coefficients must obey the following sum rule to conserve the total number of atomic particles,

$$\alpha_{pp} = \frac{1}{V_{BZ}} \int_{BZ} d\mathbf{k}\ \alpha(\mathbf{k}) = 1 \quad , \tag{1.14}$$

where the integration is over the first Brillouin zone of volume V_{BZ}.

1.3 Thesis Outline

The thesis is organized as follows. In Chapter 2, the various computation methods are introduced, showing how first-principles calculated energies of alloy structures are used to construct an effective cluster expansion Hamiltonian for multi-component alloys. The CE Hamiltonian is suitably used by atomistic level methods to calculate thermodynamic quantities used for constructing phase diagrams; two such methods are introduced, Monte Carlo (MC) and a version of mean-field theory (MFT) which obeys the sum-rule in (1.14).

In Chapter 3, we discuss how the various methods in Chapter 2 forms a multi-scaling procedure and its implementation in a C++ software package, Thermodynamics Toolkit (TTK). In addition, we discuss issues regarding the selection of a truncated (yet reliable) CE basis. Importantly, a reliable CE has to be convergent, unique and enables good prediction of structural energies. In particular, uniqueness is often overlooked in current implementations of CE, because currently, optimally truncated CE are selected based on some statistical measure of predictive capability (e.g., leave-one-out cross validation score). Importantly, there is the tendency of treating effective cluster interactions as mere coefficients to obtain a good CE fit to DFT structural energies. Due to the huge search space, several optimal CE sets (with similar cross-validation error) are possible, especially when cluster interactions are simply treated as mere stochastic parameters. The problem of non-uniqueness is improved when the basis set is enforced to be compact and locally complete basis, resulting in a physical hierarchy to rank cluster importance apriori. This provides a motivation for the new subspace projection method discussed in Chapter 6.

In the next two chapters, we showcase applications of CE on various alloys, using current procedures (based on cross-validation score) to select the optimally truncated CE set. In Chapter 4, we apply TTK to phase segregating alloys. Phase segregating boundaries are constructed for the Pd-Rh and the Ca-Sr alloy systems using MC and are compared with rapid mean-field estimates of phase-segregating boundaries, based on free-energy arguments at first order phase transitions. In both alloys, the MC and mean-field phase boundaries are similar; the results are in agreement with experiment data, which are available for Pd-Rh. As MFT estimates are often thought to be qualitative, we explain when and why the

proposed mean-field gives quantitative estimates for certain phases-segregating alloys and not others.

In Chapter 5, we apply TTK to Ag-Au alloy, where ordered phases $L1_0$ and $L1_2$ are obtained at low temperatures. The nearest-neighbor (NN) pair CE interaction is dominant and we compare the phase diagram with that from the fcc Ising model, where degenerate structures, due to lattice frustration, result in narrow coexistent regions between $L1_0$ and $L1_2$ phases. In addition, we show that interactions from CE are physical by comparing their values to direct calculations from first-principles, derived directly from the energies of embedded clusters of atoms, and we can visualize these interactions from the calculated electronic density differences.

In Chapter 6, we address the issue of uniqueness in the selection of a truncated CE basis. Currently, optimal truncated CE sets are selected based on some statistical measure of predictive capability, as discussed in Chapter 3. To address the uniqueness issue directly, we explain how the choice of structural sets (used to construct the truncated CE) impact the linear dependencies between the cluster basis, using fractional factorial design principles (from the statistics discipline). This led to the subspace projection method that allows the cluster interactions of the truncated CE basis to approach the exact (unique and not truncated) one, requiring the use of only a minimal set of DFT structural energies.

As an alternative to expensive (but exact) Monte Carlo simulations, we highlight, in Chapter 7, a mean-field theory (MFT) that produces good quantitative estimates of phase boundaries. We further extend it to clusters of general sizes and show that predicted transition temperatures approach that of (exact) Monte Carlo via finite-size scaling (versus the cluster size). Like most MFT, the phase diagrams are constructed based on comparison of free energies between competing phases. However, traditional MFTs, such as the single-site Weiss model (also known as Bragg-Williams theory), completely ignores atomic correlations and higher order entropy terms. The proposed cluster MFT uses a cluster-lattice Fourier transform to construct a set of static, self-consistent equations relating cluster and lattice correlations. For the single-site cluster, the relation ensures the conservation of particle number (see (1.14)), and its free energy expression includes Gaussian contributions from

the pair correlations. This results in a much improved phase diagram for frustrated system, and we use it to study phase transitions and boundaries for the Ising model, comparing results to that from Monte Carlo simulations.

CHAPTER 2

METHODOLOGY

We use a number of computational methods to study alloy structures and thermodynamics, with the ultimate aim of constructing reliable phase diagrams from first-principles. Due to the ever-increasing computation power, first-principles methods, such as density functional theory (DFT) [32] aimed at solving the many-electron Schrödinger equation containing a periodic potential, are now commonplace in evaluating energies of alloy structures. Although accurate DFT methods are computationally expensive and typically restricted to structures containing < 100 atoms. However, to compute thermodynamic quantities, methods such as Monte Carlo (MC) typically involve supercells with $\sim 10^3$ to 10^6 atoms and the evaluation of $\sim 10^3$ to 10^4 configurations, inaccessible by direct DFT calculations. To achieve this while still using first-principles calculated energies as input, we make use of the cluster expansion (CE) [2] as a multiscaling tool to construct an effective cluster Hamiltonian suitable for multi-component alloys. By coarse-graining out the electronic degrees of freedom, the CE constructs an effective Hamiltonian using atomic cluster (or geometric based) entities in the alloy as an expansion basis set, whose coefficients are called effective cluster interactions (ECI). The CE Hamiltonian reduces to the Ising model (or equivalently the lattice gas model) [33] when the basis set contains only single-site and nearest-neighbor pair clusters. Because the interactions associated with each cluster are significant only within a certain spatial extent in many cases, one retains only a finite and manageable number of clusters, whose interactions are then obtained via the structural inversion of typically ~ 30 to 100 structural DFT energies. The CE Hamiltonian permits direct use of MC for efficient calculation of alloy thermodynamics, construction of phase diagrams, and enables efficient search for new alloy ground states over a large configuration space.

2.1 Density Functional Theory

We employ the Vienna Ab-initio Simulation Package (VASP) [34] to determine all first-principles DFT structural energies, which are used for deriving the effective cluster interactions in CE. The VASP software package is essentially a plane wave based pseudo-potential DFT code, and uses the Projected-Augmented Wave (PAW) [35, 36] method to approach the accuracy of all-electron DFT calculations. This section provides a brief outline of DFT, whose details are covered in various literature (e.g., see [37,38]). For a given structure consisting of N_a ions and N electrons, the Schrödinger equation in atomic units (i.e., $\frac{\hbar}{m_e} \rightarrow 1$ and $\frac{e^2}{4\pi\epsilon_o} \rightarrow 1$) is

$$\hat{H}\Psi\left(\mathbf{r}_1, ..., \mathbf{r}_N\right) = \mathrm{E}\Psi\left(\mathbf{r}_1, ..., \mathbf{r}_N\right) \quad , \tag{2.1}$$

with

$$\hat{H} = -\frac{1}{2}\sum_{i}^{N}\nabla^2 - \sum_{I}^{N_a}\sum_{i}^{N}\frac{Z_I}{|\mathbf{r}_i - \mathbf{R}_I|} + \sum_{i<j}^{N}\frac{1}{|\mathbf{r}_i - \mathbf{r}_j|} \quad , \tag{2.2}$$

where the terms on the right, constituting the $\hat{H}$ operator, are the kinetic energy of the electrons, the ion-electron attraction and the electron-electron repulsion respectively; $\mathbf{R}_I$ and $\mathbf{r}_i$ are coordinates of ions and electrons respectively, and Z_I is the number of positive charges (protons) in an ion. When only the ground state electronic energy of a structure (or atomic arrangement) is of interest, one can avoid solving the above many-body problem, which is complicated and time consuming.

Via the Hohenburg and Kohn theorem [32], the electron density $\rho(\mathbf{r})$ uniquely determines $\hat{H}$ and thus the energy of the structure, $E[\rho(\mathbf{r})]$, is a functional of electron density alone and the ground state energy is obtainable via variational principle. Kohn and Sham [39] proposed expressing the functional in the following form,

$$E[\rho(\mathbf{r})] = T[\rho(\mathbf{r})] + \frac{1}{2}\int\int\frac{\rho(\mathbf{r})\rho(\mathbf{r}')}{|\mathbf{r} - \mathbf{r}'|}d\mathbf{r}d\mathbf{r}' - \sum_{I}^{N_a}\int\frac{Z_I}{|\mathbf{r} - \mathbf{R}_I|}\rho(\mathbf{r})d\mathbf{r} + E_{xc}[\rho(\mathbf{r})] \quad , \tag{2.3}$$

where the first three functional terms on the right are known exactly; $T[\rho(\mathbf{r})]$ is the kinetic

energy of a non-interacting electron gas with density $\rho(\mathbf{r})$; the second term is the classical Coulombic electron-electron interactions; the third term is the energy arising from ion-electron interaction. The many-body effect neglected in the above terms are then lumped into the so-called exchange-correlation functional, $E_{xc}[\rho(\mathbf{r})]$, whose exact form is unknown. Consequently, by assuming an explicit form for $E_{xc}[\rho(\mathbf{r})]$ and via the variational principle, $\rho(\mathbf{r})$ is found by solving the following set of self-consistent equations for ϕ_i (orbitals of non-interacting particles),

$$\left[-\frac{1}{2}\nabla^2 + \int \frac{\rho(\mathbf{r}')}{|\mathbf{r}-\mathbf{r}'|}d\mathbf{r}' - \sum_I^{N_a} \frac{Z_I}{|\mathbf{r}-\mathbf{R}_I|} + \frac{\delta E_{xc}[\rho(\mathbf{r})]}{\delta[\rho(\mathbf{r})]}\right]\phi_i(\mathbf{r}) = \epsilon_i\phi_i(\mathbf{r}) \quad , \tag{2.4}$$

and the ground state electron density is given by $\rho(\mathbf{r}) = \sum_i |\phi_i(\mathbf{r})|^2$.

Because the exact form of $E_{xc}[\rho(\mathbf{r})]$ is unknown, its form has to be approximated for practical implementation, the earliest of which is the local density approximation (LDA) [40–42] and is still commonly used. In LDA, $E_{xc}[\rho(\mathbf{r})]$ is a function of the local electron density, i.e., $E_{xc}[\rho(\mathbf{r})] \approx \int d\mathbf{r}\rho(\mathbf{r})\epsilon_{xc}(\rho(\mathbf{r}))$, where $\epsilon_{xc}(\rho(\mathbf{r}))$ is the exchange and correlation energy density of the homogeneous electron gas. A natural progression beyond LDA is to incorporate information regarding the gradient of the electron density, as is done in the generalized gradient approximation (GGA) [43], where $E_{xc}[\rho(\mathbf{r})] \approx \int d\mathbf{r}\rho(\mathbf{r})\epsilon_{xc}(\rho(\mathbf{r}), \nabla\rho(\mathbf{r}))$. Further improvements to DFT functional are highly active areas of research, but will not be addressed here. The DFT energies of alloy structures in this thesis are calculated using the VASP-PAW package within the GGA.

2.2 Cluster Expansion Method

As DFT calculations are computationally demanding and expensive, the goal is then to construct an effective Hamiltonian via cluster expansion (CE) for efficient calculation of alloy configuration energies, in order to achieve meaningful and reliable estimates of thermodynamic quantities. For a fixed lattice having N sites, any the atomic configuration of an alloy structure is described by a set of occupation variables $\{\xi_p^\alpha\}$, where ξ_p^α=1 if site p is occupied by atomic type α and 0 otherwise as discussed in section 1.2. For a fixed site in

a P-component alloy structure, there are only P − 1 independent occupation variables because of the sum rule in (1.8). For an N-site lattice, the atomic configuration is completely described by a set of occupation variables, $\vec{\sigma} = \{(\xi_1^1, ..., \xi_1^{P-1}), ..., (\xi_N^1, ..., \xi_N^{P-1})\}$.

The CE Hamiltonian for an alloy configuration described by $\vec{\sigma}$ is given by

$$H(\vec{\sigma}) = V_0 + \sum_{\eta} V_\eta \Phi_\eta(\vec{\sigma}) \quad , \tag{2.5}$$

where $\eta = \{p_1, ..., p_n; \alpha_{p_1}, ..., \alpha_{p_n}\}$, a collection of n sites making the cluster with each site having the occupation variable $\xi_{p_i}^{\alpha}$; the summation is thus over all possible clusters in the N-site lattice and over all possible combinations of $\{\alpha_p\}$ for each cluster, with each α_p having P − 1 possibilities. Hence for binary alloys (extensively discussed in the thesis), the notation is reduced to $\eta = \{p_1, ..., p_n\}$. The V_η are the effective cluster interactions with V_0 corresponding to that of the constant term $\Phi_\emptyset \equiv 1$. The cluster correlation function for an n-site cluster is defined as

$$\Phi_\eta(\vec{\sigma}) = \prod_{p_i \in \eta}^{n} \xi_{p_i}^{\alpha} \quad . \tag{2.6}$$

As expressed in (2.5), the $\Phi_\eta(\vec{\sigma})$ thus serve as the all important basis set for the CE, whose coefficients, V_η, are effective cluster interactions (ECI). In principle, with a proper and converged CE, the ECI represent physical interactions, not just expansion coefficients. Indeed, the thesis provides a methodology to guarantee the uniqueness and physical relevance of the ECI, which have not been the case previously.

Spin versus occupation variables: It is also equally valid and common to express the atomic occupation in a P-component alloy in 'spin' variables, $\{\sigma_p\}$, where σ_p takes on integer values between -P/2 to P/2 (skipping 0) or $-(\mathrm{P}-1)/2$ to $(\mathrm{P}-1)/2$ for even and odd P, respectively. When Chebyshev polynomials, with $\{\sigma_p\}$ as variables, are used to construct the cluster correlation functions, Φ_η, the set of $\{\Phi_\eta\}$ forms a complete and orthogonal basis set [2] for representing the P^{N} configurations. While the use of $\{\xi_p^{\alpha}\}$ for constructing cluster correlation functions results in a non-orthogonal (but nonetheless complete) basis set, this representation is physically more intuitive and suited for Monte Carlo simulations. It is

emphasized that both $\{\xi_p^\alpha\}$ and $\{\sigma_p\}$ are equally valid for representing alloy structures and the transformation between the two variables is straightforward, e.g., for a 2-component alloy (A-B), $\sigma_p = 2\xi_p^{\mathrm{B}} - 1$.

Cluster symmetry: In practice, it is desirable to classify clusters using the underlying lattice symmetry [6], because clusters with the same symmetry have the same ECI; e.g., for a face-centered cubic (fcc) lattice, all 12 nearest-neighbor pairs have the same ECI, which has a different value from that of the 6 next-nearest-neighbor pairs, etc. Thus, one only need to solve for symmetry distinct clusters, which are obtained from the DFT energies of symmetry unique structures via structural inversion.

2.2.1 Structural Inversion

When all clusters are included in the N-site lattice (a subspace of the infinite lattice), the CE expansion basis spans the full P^{N}-dimension configuration space for an alloy; however, for it to be practical and useful, only clusters with significant ECI should be kept. Important ECI need to be obtained from a manageable set of DFT energies via structural inversion. Writing $H(\vec{\sigma})$ as a vector, with each configuration, $\vec{\sigma}$, occupying a different row, Eq. (2.5) is expressed as

$$\begin{bmatrix} \vec{H}_1^{\mathrm{DFT}} \\ \vec{H}_2 \end{bmatrix} = \begin{bmatrix} \mathbf{\Phi}_{11} & \mathbf{\Phi}_{12} \\ \mathbf{\Phi}_{21} & \mathbf{\Phi}_{22} \end{bmatrix} \begin{bmatrix} \vec{V}_1 \\ \vec{V}_2 \end{bmatrix} \quad . \tag{2.7}$$

Each column of the correlation matrix, $\mathbf{\Phi}$, is a basis vector, and together they span the P^{N} configuration space. Here, I have specifically chosen $\vec{V}_1$ as the significant ECI while those in $\vec{V}_2$ are zero or assumed to be negligible. However, the specific ECI in $\vec{V}_1$ or $\vec{V}_2$ are not known apriori. The known quantities are $\mathbf{\Phi}$ and $\vec{H}_1^{\mathrm{DFT}}$. Because $\vec{H}_1^{\mathrm{DFT}}$ and $\vec{V}_1$ have M and L components respectively, with $\mathrm{M} \geq \mathrm{L}$, $\mathbf{\Phi}_{11}$ is an M-by-L matrix and via structural inversion (SI), which is also the general linear least square method [44],

$$\vec{V}_1 = \left(\mathbf{\Phi}_{11}^{\mathrm{T}}\mathbf{\Phi}_{11}\right)^{-1}\mathbf{\Phi}_{11}^{\mathrm{T}}\vec{H}_1^{\mathrm{DFT}} \quad , \tag{2.8}$$

provided $\mathbf{\Phi}_{11}^{\mathrm{T}}\mathbf{\Phi}_{11}$ is invertible. Note that if $\mathbf{\Phi}_{11}$ is a full rank matrix, the above equation is reduced to a matrix inversion problem [5]. Once $\vec{V}_1$ is obtained (and because ECI in $\vec{V}_2$ are assumed to be zero), all structural energies in $\vec{H}_2$ are obtained via (2.7). Obviously, if a significant ECI is in $\vec{V}_2$ (the ones assumed negligible), the truncated CE set will have a significant error.

The unresolved issue in literature is then to determine reliably the significant ECI for inclusion in $\vec{V}_1$, a significant accomplishment in achieving this goal using fractional factor design principles is discussed in great length in Chapter 6.

2.3 Methods for Alloy Phase Diagram Construction

Eventually, with a reliable set of ECI, the next step is to make use of the CE Hamiltonian for calculations at the atomistic level. With construction of temperature versus composition (T vs. c) alloy phase diagrams as the goal in mind, there are two possible approaches. The first of which is to determine phase change via discontinuity in thermodynamically averaged quantities versus T or c, as is done in MC simulations. The other way is via comparing approximated free energies of competing phases, as is done in mean-field theories, which can be improved via consideration of the self-energy term to ensure particle conservation (Chapter 7) or via including sophisticated estimations of cluster entropy as done in CVM [45–47]. The alloy phase transitions of interest here are the order-disorder type and the phase segregation type [31].

2.3.1 Monte Carlo Simulation

Due to its efficiency in calculating energies of alloy structures, the CE Hamiltonian in (2.5) is well suited for calculating thermodynamic quantities. For an alloy property A, the thermodynamically averaged value is given by

$$\langle A \rangle = \frac{\mathrm{Tr}_{\vec{\sigma}} A\left(\vec{\sigma}\right) \exp\left(-\beta H\left(\vec{\sigma}\right)\right)}{\mathrm{Tr}_{\vec{\sigma}} \exp\left(-\beta H\left(\vec{\sigma}\right)\right)} \quad , \tag{2.9}$$

where the denominator on the right-hand side is the partition function Z; the trace is over all possible alloy structures (or configurations) on a fixed N-site lattice and $\beta = 1/k_B T$, the inverse temperature.

It is, of course, impossible to do a true thermodynamic average, which requires $\sim 10^{23}$ configurations. The strategy in MC simulation is then to sample important configurations [48, 49] that have higher probability of occurrence, as is achieved using the Metropolis algorithm [50], which obeys detailed balance. Configurations are typically sampled from a simulation box (with periodic boundary conditions) containing $\sim 10^4$ lattice sites for our studies. The algorithm works for both the canonical (fixed composition) and the grand-canonical (fixed chemical potential, variable composition) ensembles. For the grand-canonical ensemble, a site is chosen (one can do this sequentially or randomly) and an attempt is made to change the atom type occupying the site. For canonical ensemble, to maintain a fixed composition, only attempts to swap atoms between two randomly selected sites are made. At each MC step, an attempt is made and is accepted if it lowers the energy of the system. Otherwise the attempt is accepted with the probability $\exp(-\beta \Delta H)$, where ΔH is the energy difference between the configurations after the attempt and before the attempt. The quantity of interest, $\langle A \rangle$, is then averaged over $\sim 10^3$ to 10^4 MC steps.

To determine first and second order phase transitions, the thermodynamically averaged energy, $\langle H \rangle$, and the heat capacity, $(\langle H^2 \rangle - \langle H \rangle^2)/k_B T^2$ are calculated, respectively. Using first-order transitions as example, in the case of canonical ensemble, $\langle H \rangle$ is plotted against T at fixed c; for the grand-canonical case, $\langle H \rangle$ is plotted against c at fixed T. Discontinuities in the plots are then phase transition points on the T-c phase diagram, which are connected to form smooth phase boundaries according to Gibb's rule.

2.3.2 Mean-field Theory Approach

The exact free energy is defined as

$$F \equiv \langle H \rangle - TS \tag{2.10}$$

where the thermodynamically averaged energy, $\langle H \rangle$, is as defined in Eq. (2.9) and S is the entropy of the system. F is related to the partition function (see previous section), Z, by $F = -k_B T \ln \mathrm{Z}$. In mean-field approaches, the energy is averaged over all configurations in a small cluster, $\langle H \rangle_{\mathrm{cl}}$, with atoms outside the cluster providing an effective mean-field. The entropy is estimated from that of the cluster, $\hat{S}$, thus

$$F \approx \langle H \rangle_{\mathrm{cl}} - T \sum_{\mathrm{cl}} \hat{S}_{\mathrm{cl}} \quad , \tag{2.11}$$

where the sum is over all non-overlapping clusters in the lattice. The free energy is then approximated for competing phases (e.g., disordered versus ordered) and plotted v.s. variables T, c or μ to construct phase diagrams.

For a binary alloy, the simplest estimation of the free energy is given by the single-site Weiss model (also known as the Bragg-Williams approximation) where

$$\langle H \rangle_{\mathrm{cl}} = \mu \sum_{p} c_p + \frac{1}{2} \sum_{pq} V_{pq} c_p c_q + \frac{1}{3} \sum_{pqr} V_{pqr} c_p c_q c_r + ... \tag{2.12}$$

$$\hat{S}_{\mathrm{cl}} = -k_B \left(\sum_{p} c_p \ln c_p \right) \quad . \tag{2.13}$$

Because only one independent occupation variable, α, is needed for a binary, we have dropped the atomic type label, i.e., $\xi_p^{\alpha} \rightarrow \xi_p$ and $c_p^{\alpha} \rightarrow c_p$. Here the entropy term is composed of point entropy only and $c_p = \langle \xi_p \rangle_{\mathrm{cl}}$, which is averaged over a single-site; $\langle H \rangle$ is estimated without any consideration for pair-wise correlations,

$$G_{pq} \equiv \langle \xi_p \xi_q \rangle - c_p c_q \quad , \tag{2.14}$$

as is used in the definition of Warren-Cowley SRO in (1.12). From the above definition, $G_{pp} = c_p(1 - c_p)$ and must conserve the particle conservation rule in (1.14). However, this is not the case for the single-site Weiss model, hence phase diagrams obtained from this simple approximation are often inaccurate and gets the wrong phase boundaries for frustrated systems.

In Chapter 7, we will show how the single-site free energy approximation is improved, just by including diagonal terms in the self-enegy, ensuring that (1.14) is obeyed. The resulting single-site model yields a phase diagram which is close to the exact one and we show how the approximation can be improved systematically by extending to bigger n-site clusters. Other mean-field estimates are also discussed in Chapter 4 that works specifically for phase-segregating alloys with first-order transitions, at which the difference in F between the disordered and segregated phases is zero.

CHAPTER 3

IMPLEMENTING THE CLUSTER EXPANSION METHOD AS A MULTISCALING TOOL

The methods discussed in the previous chapter are linked up to form a multiscaling procedure for obtaining reliable alloy thermodynamics and is implemented in the Thermodynamics Toolkit (TTK), a C++ code package which I have developed. Given an alloy system, a (finite) set of structures is *somehow* selected and their energies are evaluated from DFT using the VASP software package. Both unit cell shape and atomic positions of a structure are allowed to relax, achieving a local minimum in energy. When relaxations are not drastic, a concentration independent effective CE Hamiltonian (for a fixed lattice) is then constructed via SI (see Section 2.2.1). Given that the CE is a complete basis set expansion [2] for the configuration space of the alloy on a fixed lattice, there should be one unique set of ECI for a given alloy. This is essentially a transformation of basis; instead of describing the alloy in terms of structural energy versus configuration (or structure), we represent them in terms of ECI versus cluster type. For an infinite lattice, one would need an infinite number of cluster functions to span the configuration space. The 'hope' is thus that the CE basis is convergent, thus allowing reliable alloy thermodynamic calculations from only a finite and tractable number of cluster functions. Because there are many ways to obtain a truncated CE, lying at the heart of the truncation problem are three inter-related issues,

1. *Convergence*: How quickly does the magnitude of the ECI diminish with cluster complexity?

2. *Uniqueness*: Is there a unique way of truncating the CE, ideally, retaining only significant ECI whose values are a priori unknown?

3. *Predictive* capability: Is the truncated CE able to predict structural energies not used in the SI?

These issues are further elaborated in the next section.

When the truncated CE satisfies the above conditions, it is reliable. This optimal set is then used for the efficient calculation of formation enthalpies of a large number of configurations, thus suitable for extensive alloy groundstate configuration searches [13,51,52] (see Section 5.3.2 too). The CE set can also be used for various atomistic-level computation methods such as Monte-Carlo for thermodynamics and phase diagram calculations [8, 16, 53–56]. The multiscaling procedure is illustrated in Fig. 3.1.

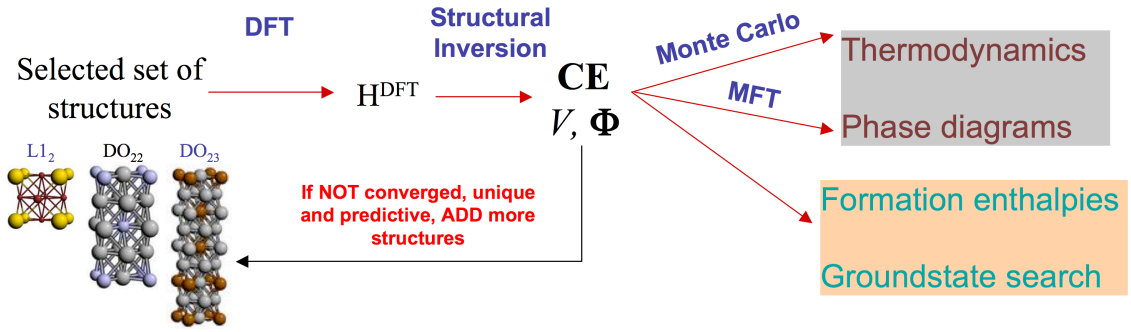

Figure 3.1: Cluster expansion (CE) approach as a multiscaling tool. Starting from first-principles DFT calculations, the CE Hamiltonian along with its ECI (V) are obtained via structural inversion (SI). The CE is also used to calculate thermodynamic properties and phase diagrams via atomistic-level computation such as Monte Carlo (MC) or mean-field theories (MFT). It can also be used to scan over large number of configurations for new alloy groundstates. The procedures are implemented in the TTK code.

3.1 Reliable Truncation of Cluster Expansion Basis

For an N-site lattice (where N is large), there are P^N possible configurations for a P-component alloy and hence the complete CE basis consist of P^N cluster entities. In many alloy cases, it has been demonstrated that the CE is convergent, [2, 5–8, 12, 16, 17, 20, 21, 56–58], thus the formation energies of ordered structures are reproduced well with a finite set of clusters, when judiciously selected. Because only a subset of M structural energies from DFT are evaluated, one can at most know M ECI via SI (out of the possible P^N ECI), hence a choice of ECI has to be made. Ideally, this choice should be unique and includes all important ECI, as pointed out in Section 2.2.1. In current literature, this choice is made

based on some measure of predictive capability. The M structural energies are divided into smaller sets consisting of m structures, and each set is selected in turn for validation, using ECI obtained from SI involving the other M/m − 1 sets. A popular choice is the leave-one-out cross validation (CV_1) [12], where m=1; the predictive capability of a set of ECI is then given by CV_1 score (see next section for details), via an average of the predictive errors from all validation sets. The set of truncated ECI with the lowest CV_1 score is then chosen and is often called the optimal CE set.

Existing methods: Now, if all ECI are treated as parameters to achieve a good fit to structural energies, we have a large search space (for the optimal ECI set), thus warranting methods such as genetic algorithm (G.A) [59,60]. Because of the large search space, several optimal sets of ECI (whose CV_1 scores are very close) are often found, leading to non-uniqueness. Thus the main criticism of such a treatment is that the optimal sets of ECI are void of any physical meaning; they are mere stochastic variables used for a good fit to a given structural data set (DFT energies). This often leads to the inclusion of physically less important (higher order and larger spatial extent) cluster at the expense of more important ones.

On the other hand, one could use rules based on physics to reduce the search space, partially addressing the problem of non-uniqueness. Importantly, if a cluster is included in the set of ECI to be determined, *all* its subclusters (of lower order and smaller spatial extent) have to be included, resulting in a compact and locally complete CE basis [6]. Based on this rule, the clusters are ordered in a physical hierarchy [6]; specifically, clusters with lesser sites (i.e., of lower order) and smaller spatial extent are more 'likely' to be associated with a significant ECI. The above criteria is implemented in the current version of the TTK code, and the selected optimal CE via CV_1 score had been shown to reproduce well experimental order-disorder T_c (e.g., Ni_3V [6], Pd-Rh (see Figure 4.2)).

New perspective: In addition, because a limited number of structural energies is used for SI, there are linear dependencies between the cluster functions, which should not be the case had all P^N possible structural energies been used. ECI of linearly dependent clusters are not distinguishable by SI, because it results in a singular inversion matrix. To avoid

cases where potentially significant ECI are linearly dependent, as a precaution, existing CE selection methods uses a relatively large number of structural energies for SI (M$\sim$ 30 to 100), which is not always necessary.

Using concepts from statistics, specifically fractional factorial design [61, 62], we elucidate how the choice of structures from a configuration subspace impact the linear dependencies between cluster functions. When all P^N structural energies are known (full factorial design), each ECI has a specific physical and mathematical definition; each ECI is an effect *contrast* given by a specific linear combination of structural energies, defined according to the corresponding rows or columns of a Hadamard matrix [61, 62]. The true ECI values are known exactly only if all P^N structural energies are used during SI. However, when only a subset of M structural energies are used, the M ECI evaluated are biased. This is because, for a given choice of M structures, we only require M cluster functions to span the configuration subspace. When projected onto this subspace, the remaining $(P^N - M)$ cluster functions are linearly dependent on the spanning set (of M cluster functions).

A potentially important cluster can be made linearly independent if the original subspace is enlarged with the addition of an appropriate structure, thus removing the bias arising from its associated ECI. When all important clusters are included, the evaluated ECI are biased only by the insignificant ones, hence we approach the unique ECI values of the complete non-truncated CE. This leads to the subspace projection method that uses a minimal set of judiciously selected structural energies for evaluating potentially important ECI via SI (e.g., requiring 3 times less structural energies for Ag-Au system to achieve comparable predictive capability). This insight together with new methods of selecting structures and clusters, based on subspace projection, are discussed in Chapter 6. Before that, I first discussed applications of CE based on currently existing methods to real alloy systems.

3.2 Current Implementation

Although the CE is broadly used and implemented in several packages, such as ATAT [63,64] and our TTK code, the various implementations differ in how they select the clusters and

assign weights to structures during SI. This may lead to different ECI for a given alloy system. For our TTK code (see Figure 3.1), we typically begin by using DFT energies of $\sim$ 30 structures from the "smallest-first" algorithm [65,66] to construct a compact and locally complete [6] truncated CE, using leave-one-out cross-validation (CV_1) as the fitness criteria. To test for convergence, the truncated ECI may be used to conduct a groundstate search over millions of configurations, and each suspected groundstate is verified via DFT calculations. The DFT verified structures are added to the previous set of known energies and a new set of truncated ECI is obtained. The process is repeated until the truncated ECI stops predicting new groundstates. Using occupation variables for the CE Hamiltonian, the converged and optimally truncated ECI is then used in Monte Carlo simulations (as described in Section 2.3.1) to obtain thermodynamic quantities for constructing phase diagrams.

3.3 Application to FCC Alloys

In this section, we detail the practical implementation of TTK to fcc alloys. The computation details for various stages shown in Figure 3.1 are discussed in turn and applied to real alloy systems in Chapters 4 and 5.

3.3.1 Selection of Alloy Structures

The TTK code uses the "smallest-first" algorithm [65, 66] to generate different fcc alloy configurations (structures), and supplement with long-period superstructures [6]. All the structures with different interatomic correlations are uniquely enumerated. Structures with the smaller number of sites (atoms) per primitive cell appear before larger ones. The first structure has one atom per fcc primitive cell designated as A1 cF4 (Cu) structure with $Fm\bar{3}m$ space group (no. 225). The second structure with two atoms per primitive cell is $L1_0$ tP2 (CuAu) structure with $P4/mmm$ space group (no. 123), with the translation vectors $(-2,0,0)$, $(0,-1,1)$, $(0,1,1)$. Within the same number of sites per cell, structures with shorter translation vectors appear first. The third structure has two atoms per primitive cell and the translation vectors $(-2,-1,-1)$, $(0,-1,1)$, $(-1,0,1)$. These vectors are sorted by length (longest first). Fourth and fifth are oI6 ($MoPt_2$) structures with 3 atoms per

cell at compositions of 1/3 and 2/3, respectively. Similarly, the first two structures with 4 atoms per primitive cell are $L1_2$ cP4 (Cu_3Au) at compositions of 1/4 and 3/4, which are the 10^{th} and 11^{th} structures.

The "smallest-first" algorithm [65] can be used for enumerating structures on any fixed lattice. Although consideration of only a limited set of the smallest structures bears the risk of missing long-range interactions, as we shall show, such interactions are not important in the phase-segregating systems considered in Chapter 4.

3.3.2 DFT Calculations

Electronic energies of various alloy structures are calculated via the Vienna Ab-initio Simulation Package (VASP) [34] — a pseudopotential code using projector augmented-wave (PAW) basis sets [67, 68] and the generalized-gradient approximation [43] (GGA). We used a plane-wave energy cutoff of 400 to 425 eV for all alloy structures, and converged Brillouin zone integration meshes [69, 70] with 8^3 to 16^3 k-points/cell, depending on the cell size. All the structures were relaxed using the conjugate-gradient algorithm within VASP so that residual pressures for most structures are below 1 kB and atomic forces did not exceed 0.03 eV/Å.

3.3.3 Cluster Expansion on Fixed Lattice

Given that we are interested in configurations on a fixed lattice, it is desirable to classify clusters using the underlying lattice symmetry, because clusters with the same symmetry have the same ECI. On a fixed lattice having N sites, any binary alloy configuration σ can be represented by a set of occupational variables $\{\xi\}$ (introduced in Section 1.2), with ξ_p being 1 (0) if site p is (not) occupied by solute. We assume that all sites are occupied. An average over site occupation gives the solute concentration for configuration σ, i.e.

$$\langle \xi \rangle_\sigma = \frac{1}{N} \sum_p^N \xi_p(\sigma) = c(\sigma). \tag{3.1}$$

In the disordered phase $\langle \xi_p \rangle = c$ for each site p.

A cluster is a fixed set of lattice sites. All possible clusters of lattice sites $\{p\}_{nfd}$ can be enumerated. Here n is the number of sites within the cluster (e.g., $n = 2$ for pairs); f enumerates symmetry-distinctive shapes of the n-site clusters (e.g., $f = 1$ for nearest- and $f = 2$ for next-nearest neighbors); smaller clusters have smaller indices. Index d distinguishes symmetry-equivalent n-body clusters of shape f. Because ξ_p is either 0 or 1 for any given site p of a fixed configuration σ, a product $\prod_{p_i \subset \{p\}_{nfd}} \xi_{p_i}$ is also either 0 or 1 for a fixed set of sites $\{p\}_{nfd}$ including site p. The n-site correlation function

$$\begin{aligned} \bar{\Phi}_{nf}(\sigma) &= \langle \xi_{p_1} ... \xi_{p_n} \rangle_\sigma \\ &= \frac{1}{N D_{nf}} \sum_{p}^{N} \sum_{d}^{D_{nf}} \prod_{p_i \subset \{p\}_{nfd}}^{n} \xi_{p_i}(\sigma) \end{aligned} \tag{3.2}$$

is an ensemble average bounded by $0 \leq \bar{\Phi}_{nf} \leq 1$. The number of symmetry-equivalent clusters including one particular site p is called *degeneracy* D_{nf}; for example, for fcc lattice $D_{21} = 12$ accounts for the number of nearest-neighbor pairs. In the homogeneously disordered state with no short-range order $\langle \prod \xi_p \rangle = \prod \langle \xi_p \rangle$ and

$$\bar{\Phi}_{nf}(c) = c^n. \tag{3.3}$$

In the disordered phase the atomic pair correlations $\bar{\Phi}_{2f}(c)$ describe the atomic short-range order.

The general form of cluster expansion in (2.5) is then expressed as

$$H(\sigma) = \frac{1}{N} \sum_{p}^{N} \xi_p \sum_{n,f} \widetilde{V}_{nf} \frac{1}{n} \sum_{d}^{D_{nf}} \prod_{i=2}^{n} \xi_{p_i} \tag{3.4}$$

(where $p_i \subset \{p\}_{nfd}$ and $p_i \neq p$) can be written in terms of averaged correlations $\bar{\Phi}_{nf}(\sigma)$ defined by (3.2) and weighted effective cluster interactions $V_{nf} \equiv D_{nf} \widetilde{V}_{nf}/n$, namely,

$$H(\sigma) = \sum_{n,f} V_{nf} \bar{\Phi}_{nf}(\sigma). \tag{3.5}$$

The energy of the fully-disordered state is

$$H_d(c) = \sum_n c^n \sum_f V_{nf}. \tag{3.6}$$

Often it is convenient to approximate the formation enthalpy using the CE Hamiltonian by

$$\begin{aligned} \Delta H^F(\sigma) &= H(\sigma) - [(1-c)H(0) + cH(1)] \\ &= \sum_{n\geq 2}\sum_f [\bar{\Phi}_{nf}(\sigma) - c]V_{nf} \quad , \end{aligned} \tag{3.7}$$

where $H(c=0) \equiv H(0) = V_0$ and $H(1) = \sum_{nf} V_{nf}$.

We find V_{nf} by fitting a set of $\Delta H^F(\sigma)$ obtained from DFT. Using these interactions, we identify the ground states (here only fcc), calculate the enthalpy of the fully-disordered phase versus c, and perform thermodynamic calculations via Monte Carlo and/or mean-field theories.

3.3.4 Estimating Predictive Capability via Cross-Validation

If V_{nf} are known, energies of any atomic configuration σ with correlations $\bar{\Phi}_{nf}(\sigma)$ can be predicted with the CE (3.5). Errors associated with CE energies may be evaluated using a standard statistical measure of exclude-m cross-validation (CV) score [71–73]

$$\varepsilon_m^2 = \frac{1}{M}\sum_{i=1}^{M} \frac{1}{C_{m-1}^{M-1}} \sum_{j=1}^{C_{m-1}^{M-1}} (H_{DFT}^i - H_{CE(M-m_j)}^i)^2. \tag{3.8}$$

Here $H_{CE(M-m_j)}^i$ is *predicted* by a fit to $(M-m)$ DFT energies *excluding* a set m_j of m DFT energies, one of which is H_{DFT}^i. The number of possible sets m_j is given by $C_{m-1}^{M-1} = (M-1)!/[(m-1)!(M-m)!]$.

Thus, ε_0 yields a least-squares fit error, measuring how well the CE reproduces the known *fitted* DFT energies. Error in the predicted unknown values can be estimated by an exclude-m CV score ε_m, if m new values are predicted simultaneously. The exclude-one

CV score

$$\varepsilon_1 = \left[\frac{1}{M} \sum_{i=1}^{M} (H^i_{DFT} - H^i_{CE(M-1_i)})^2 \right]^{1/2} \tag{3.9}$$

estimates an uncertainty in predicting one excluded or unknown structural formation enthalpy ΔH^F. Both too few (underfitting) or too many (overfitting) parameters give poor prediction, so ε_1 has a minimum [6, 53]. Previously it was suggested to select the best CE by minimizing the predictive error estimated by ε_1 [6, 53, 74]. However, for correlated data ε_1 is not always a good estimate of the predictive error. In general, we can put an error bar on ε_m by $\varepsilon_{m-1} \leq \varepsilon_m \leq \varepsilon_{m+1}$. In particular, if ε_2 is infinite, ε_1 has an infinite upper error bar. Only if ε_2 is finite can we use ε_1 to estimate the CE predictive error for a well-defined compact cluster basis [6]. Total error in predicted thermodynamics arises from cumulative errors in the DFT, CE, and Monte Carlo statistics [7].

CHAPTER 4

PHASE TRANSITIONS OF PHASE-SEGREGATING FCC ALLOYS

Knowledge of the ground states and the temperature (T) versus composition (c) phase diagrams are of crucial importance in materials design. Unfortunately, low-temperature phase transitions are often difficult to observe experimentally due to slow kinetics. Yet, sometimes unexpected phase transitions are responsible for catastrophic failures of aging materials. Thus, multiscale theoretical and computational methods, including rapid estimates of phase stability, are important in materials design and for safety verification. Here we apply the cluster expansion methodology via the Thermodynamic ToolKit (TTK) software package, as discussed in Section 3.3, to several face-centered-cubic (fcc) based alloys, which phase-segregates at low T, focusing mainly on Ca-Sr (prediction) and Pd-Rh (validation). T_c obtained from Monte Carlo (MC), rapid mean-field estimates and experiments (if available) are compared. The discussions in this chapter are also available in [8].

4.1 Introduction

Pd-Rh has a well-known miscibility gap [25,75–77], previously studied theoretically [51,78–80], hence it is perfect for assessing simple methods for estimating transition temperature T_c. Being both from group 2A alkaline earth metals, the more chemically active radioactive Sr isotope has tendency to replace Ca in living organisms. The assessed Ca-Sr phase diagram [25,81] shows a solid-solid phase boundary between disordered high-T body-centered cubic and a low-T fcc solid-solution phases, but no known transitions inside the fcc phase. As each alloy is expected to have segregated and/or ordered states at low temperatures, there must be a T_c phase boundary.

We first obtain optimally truncated CEs for Ca-Sr and Pd-Rh, using the specific im-

plementation discussed in Section 3.3. The CE Hamiltonians are used to construct T_c versus c diagrams for Ca-Sr and Pd-Rh using two methods: a rapid estimate by an analytic mean-field solution of the Gibbs equation (Section 4.1.1), and Monte Carlo simulation. Using thermodynamic integration, we determine under what circumstances for the derived interactions in these alloys the mean-field solution is accurate. For Pd-Rh, we compare our results to experimental data and show that results from both methods are accurate. We use the methods on (Cu, Ag, Au)-Rh and Au-Pt for trends. We conclude by comparing results to other mean-field estimates and discuss how vibrations will affect our results, including a means to assess *a priori* when vibrational effects are important.

4.1.1 Rapid Estimate of T_c

Because change of Gibbs free energy $\Delta G(T) = \Delta H(T) - T\Delta S(T)$ is zero at a first-order transition at T_c, where ΔH and ΔS are changes in enthalpy and entropy between the two coexisting phases at T_c,

$$T_c(c) = \frac{\Delta H(T_c, c)}{\Delta S(T_c, c)}, \tag{4.1}$$

Equation (4.1) is exact; however, the ratio is difficult to find directly. For given interactions V_{nf}, estimates of T_c can be made quickly using mean-field approximation, or a relatively accurate value can be calculated by Monte Carlo methods.

Mean-field "T_0" Estimate:

T_c can be quickly estimated by assuming that $\Delta H(T_c)$ in (4.1) is proportional to the difference between T=∞ fully-disordered and T=0 fully-ordered states, i.e., $\Delta H_{d-o} = H(T = \infty) - H(T = 0)$, and similarly for the entropy. Then

$$T_c(c) \approx \frac{\Delta H_{d-o}(c)}{\Delta S_{d-o}(c)} \equiv T_c^{est}(c) \tag{4.2}$$

is a standard mean-field approximation, often called the "T_0" line [5, 79, 82]. Entropy of a single fully-ordered or phase-segregated state is zero, while that of the fully disordered

state is given by only the point entropy, i.e.,

$$S_d(c) = -k_B \left[c \ln c + (1-c) \ln(1-c) \right]. \tag{4.3}$$

The difference in enthalpy (4.2) can be calculated trivially within the cluster expansion using (3.5-3.6). For phase-segregation, as is the case for Ca-Sr and Pd-Rh,

$$\Delta H_{d-o}(c) = \Delta H_d^F(c) = \sum_{n \geq 2} (c^n - c) \sum_f V_{nf}. \tag{4.4}$$

Although $\Delta H(T_c)$ in (4.1) is typically orders of magnitude smaller than ΔH_{d-o} in (4.2), and the same is also true for ΔS, the mean-field estimate is accurate if and only if the ratio $\Delta H/\Delta S$ in (4.1) and (4.2) is approximately the same, which should be the case for a large class of systems identified by the underlying interactions.

We suggest that the approximation (4.2-4.4) is expected to be accurate for alloys with competing (pair and multibody) interactions, which lower the enthalpy and entropy differences due to atomic correlations (clustering here) such that the ratio in (4.1) remains approximately equal to that in (4.2), as we show in the results. The rapid estimate $\mathrm{T}_c^{est}(c)$ from (4.2) provides an accurate $\mathrm{T}_c(c)$ for Pd-Rh and Ca-Sr at all c except those near $c = 0$ and $c = 1$, where both ΔH and ΔS approach zero.

Mean-field "Bethe" Estimate

T_c can be also quickly estimated using another first-order, mean-field theory by Bethe for the zero-field Ising ferromagnet (equivalent to a clustering 50% binary) [83–85]. Bethe improved the Weiss molecular-field theory by including the short-range correlations in order to enforce agreement between the average magnetization on the central site and nearest neighbors. The well-known solution in terms of the nearest-neighbor pair $\widetilde{V}_{21}$ in (3.4) is

$$T_c^{Bethe} = \frac{\widetilde{V}_{21}}{2k_B} \left[ln \left(\frac{q}{q-2} \right) \right]^{-1} \tag{4.5}$$

where q is the coordination number of the Bravais lattice (e.g., 12 for fcc). In the limit where mean-field theory is exact (i.e., $q \to \infty$) the Weiss result of $q\widetilde{V}_{21}/4k_B$ is recovered, whereas the fcc nearest-neighbor-only T_c^{Bethe} result is lower by a factor of 1.0939. More notably, for the Ising ferromagnet, the Bethe approximation predicts the correct behavior of T_c in d dimensions; for example, in $2d$ with $q = 2$, T_c^{Bethe} is zero, the correct answer [85].

While Bethe derived the theory for a nearest-neighbor pair interaction, it is straightforward to extend his derivation (in the same approximations) to pair interactions of arbitrary range, which we write for an alloy using (3.7) as

$$T_c^{Bethe2} = \frac{2\Delta H_d^F(c)}{k_B}\left[\frac{q_{eff}}{2} ln\left(\frac{q_{eff}}{q_{eff}-2}\right)\right]^{-1}, \tag{4.6}$$

where the effective coordination number is

$$q_{eff} = \sum_{f=1}^{N} \frac{\widetilde{V}_{2f}}{\widetilde{V}_{21}} D_{2f}. \tag{4.7}$$

For interactions $\widetilde{V}_{2f}$ held constant to $\widetilde{V}_{21}$, independent of range, for all shells of neighbors, the Weiss result of $q\widetilde{V}_{21}/4k_B$ is recovered. Note that for a phase-segregating alloy, T_c is estimated as $2\Delta H_{d-o}(c)/k_B$ for long-range, clustering-only pair interactions.

Extending the Bethe approximation to ordering (antiferromagnetic) interactions (and its longer-range, competing interaction, variant) is tenuous because it is sensitive to the lattice topology, even for the ferromagnetic case [86,87]. The same is true for the extension to the general multibody interaction case. The Bethe approximation is exact, however, in the limit that $\widetilde{V}_{2f}$ are only clustering and long ranged. More importantly, for clustering-only $\widetilde{V}_{2f}$ (independent of range), T_c^{Bethe2} is independent of entropy change, in contrast to $\mathrm{T}_c^{est}(c)$. Hence, alloys cannot be described, generally, by Bethe or Weiss type theories if they have competing clustering- and ordering-type interactions. Therefore, only at the end will we contrast the results of $\mathrm{T}_c^{Bethe2}(c)$ with $\mathrm{T}_c^{est}(c)$ and $\mathrm{T}_c^{MC}(c)$.

4.1.2 Monte Carlo Determination of T_c

We also find an accurate T_c by locating maxima in specific heat, using $\widetilde{V}_{nf}$ within the lattice Monte Carlo program with Metropolis algorithm [50] as implemented within TTK [88]. We used from 16^3 (or 4096) to 24^3 (or 13824) atoms within the periodic simulation box. We performed grand-canonical simulations with either fixed chemical potential or fixed temperature, as well as canonical (fixed-composition) simulations with 200–800 equilibration steps and 4000–16000 sampling steps. To perform any noted finite-size scaling, we included up to 32^3 simulation box (32768 atoms).

4.1.3 Thermodynamic Integration

In Section 4.2.4 we will investigate the difference in enthalpies and entropies between the two phases versus T and c. To do this we find the enthalpies $\langle H \rangle$ and specific heats $C_v \sim \langle H \rangle^2 - \langle H^2 \rangle$ using thermodynamic averages within canonical Monte Carlo. Entropies $S(T, c)$ are then found by thermodynamic integration, i.e.,

$$\begin{aligned} S(T_+ > T_c) &= S_d - \int_{T_+}^{\infty} dT \frac{C_v(T)}{T} \\ S(T_- < T_c) &= S_o + \int_0^{T_-} dT \frac{C_v(T)}{T}, \end{aligned} \tag{4.8}$$

where $S_o = 0$ and S_d in (4.3) are known. Near T_c we use a temperature step of approximately $0.01\,T_c$, while at higher temperatures a significantly coarser temperature integration step can be used.

4.2 Results

4.2.1 Structural Formation Enthalpies

First-principles calculated formation enthalpies ΔH^F of various fcc Ca-Sr and Pd-Rh structures are given in Fig. 4.1, where all ΔH^F are positive. Hence we expect both alloys to segregate at low enough temperatures [order of magnitude is roughly $k_B T_c(c) \sim \Delta H_d^F(c)$]. The internal atomic relaxations in all these structures are relatively small compared to in-

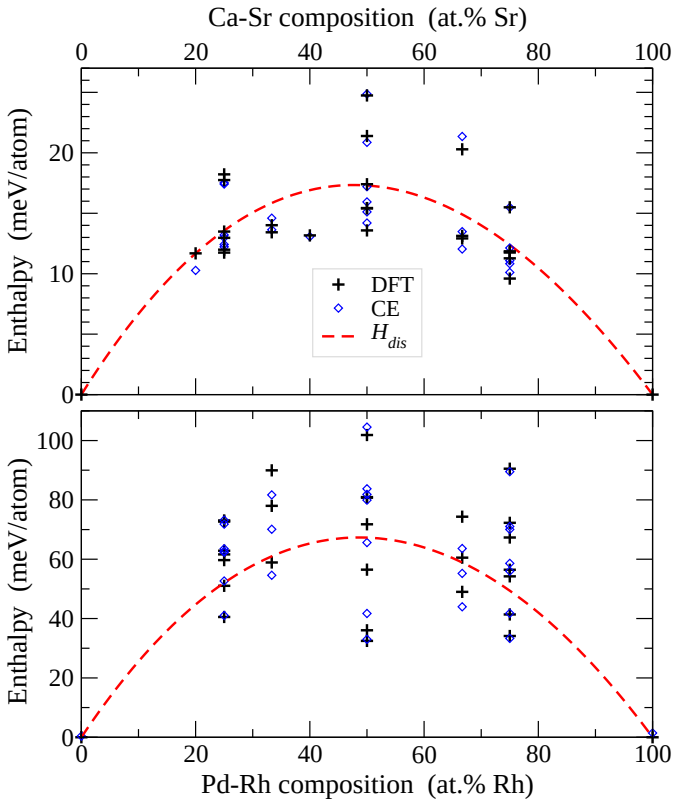

Figure 4.1: (color online) Formation enthalpies of the fcc Ca-Sr (upper) and Pd-Rh (lower) structures from DFT (crosses) and CE (diamonds), with enthalpy of the fully-disordered phase, Eq. (3.6), included (dashed lines).

teratomic distances, so an effective lattice for both Ca-Sr and Pd-Rh at low temperatures is fcc only (in contrast, for example, to Ca-Ag or Al-Ag) [16,17]. Next, there is a small asymmetry of structural enthalpies versus composition; namely, formation enthalpies of similar binary structures (e.g., $L1_2$ or DO_{22} at 25% and 75%) are not the same at c and $(1-c)$, indicating presence of multibody interactions beyond pairs.

Many alloy phase diagrams are known from a combination of experimental data and thermodynamic modeling; hence, the boundaries are estimates, as in the case of Au-Pt, which exhibits an asymmetric miscibility gap with a maximum at 61% Pt [25]. We will focus primarily on Pd-Rh (known) and Ca-Sr (new prediction). However, as shown in Figure 4.5, Au-Pt exhibits a highly asymmetric formation enthalpies of similar structures, indicating important multibody interactions, and yielding a $\Delta H_d^F(c)$ with a maximum roughly at 62 %Pt, in agreement with asymmetry in experiment. Interestingly, in highly cold-work Au-

Table 4.1: Interactions V_{nf} (3.5) and $\widetilde{V}_{nf}$ (3.4) in meV with their degeneracies D_{nf} for four alloys, see Sec. 4.2.2.

		Ca-Sr		Pd-Rh		Cu-Rh		Au-Pt	
f	D_{2f}	V_{2f}	$\widetilde{V}_{2f}$	V_{2f}	$\widetilde{V}_{2f}$	V_{2f}	$\widetilde{V}_{2f}$	V_{2f}	$\widetilde{V}_{2f}$
1	12	-14.3	-2.39	-330.8	-55.13	229.2	38.19	160.6	26.77
2	6	-21.0	-7.00	-3.8	-1.27	54.5	18.18	55.3	18.42
3	24	-28.4	-2.37	-9.3	-0.77	140.6	11.72	97.6	8.13
4	12	9.1	1.52	5.3	0.88	-29.5	-4.91	9.4	1.56
5	24	-24.7	-2.06			-26.6	-2.21	-24.1	-2.00
6	8	-7.3	-1.83			44.7	11.18	9.5	2.39
7	48	6.4	0.27			-82.7	-3.45	-26.0	-1.08
8	6	-5.2	-1.72					-12.0	-4.00
f	D_{3f}	V_{3f}	$\widetilde{V}_{3f}$	V_{3f}	$\widetilde{V}_{3f}$	V_{3f}	$\widetilde{V}_{3f}$	V_{3f}	$\widetilde{V}_{3f}$
1	24	-9.3	-1.16	20.6	2.57	-311.7	-38.96	-424.9	-53.11
2	36	5.3	0.44	5.6	0.47	-67.4	-5.62	-33.2	-2.77
3	72	15.3	0.64	-40.3	-1.68	-493.1	-20.55	-169.4	-7.06
4	18			85.8	14.31	158.5	26.42	-72.7	-12.12
5	72			85.8	14.31	158.5	26.42	-41.9	-1.75
f	D_{4f}	V_{4f}	$\widetilde{V}_{4f}$	V_{4f}	$\widetilde{V}_{4f}$	V_{4f}	$\widetilde{V}_{4f}$	V_{4f}	$\widetilde{V}_{4f}$
1	8			-21.8	-10.9	83.4	41.69	10.1	5.07
2	48					4.3	0.36	455.2	37.94
3	48					212.9	17.74	253.0	21.08
f	D_{5f}	V_{5f}	$\widetilde{V}_{5f}$	V_{5f}	$\widetilde{V}_{5f}$	V_{5f}	$\widetilde{V}_{5f}$	V_{5f}	$\widetilde{V}_{5f}$
1	30							-186.5	-31.09
2	120							-133.2	-5.55

Pt, metastable Au_3Pt has been found, which corresponds to low-energy structures we find at 25% and 33% Pt, see the Sec. 4.3.5 for more discussion. We also show similar results for Rh-(Cu,Ag,Au) alloys in the Sec. 4.3.5 (see Fig. 4.5) to provide a trend in segregation going down a column in the periodic table. However, the stability of the liquid phase is critical for the Rh-(Ag,Au) systems, and its thermodynamic influence is also very important for the concentrated Rh-Cu and Pt-Au, where $T_c \sim T_{melt}$, as discussed in Sec. 4.3.2.

4.2.2 Interatomic Interactions

We used DFT structural enthalpies to find cluster interactions (Table 4.1) within the CE basis [6]. We found several sets of cluster interactions with low fit and predictive errors, all approximately equal; using those equally good sets in Monte Carlo lead to similar results.

Table 4.2: DFT and CE enthalpies (meV/atom) and their difference for the fcc Ca-Sr and Pd-Rh structures with concentration c relative to the elements. CV errors for Ca-Sr are $\varepsilon_0 = 0.57$, $\varepsilon_1 = 1.33$ and $\varepsilon_2 = 1.42\,m$eV/atom. CV errors for Pd-Rh are $\varepsilon_0 = 4.3$, $\varepsilon_1 = 7.5$, and $\varepsilon_2 = 7.7$ meV/atom.

		Ca-Sr			Pd-Rh		
Structure	c	H_{DFT}	H_{CE}	error	H_{DFT}	H_{CE}	error
Ca	0	0.0	0.7	0.74			
Sr	1	0.0	-0.1	-0.07			
Pd	0				0.0	0.4	0.38
Rh	1				0.0	1.4	1.42
2 $L1_0$	1/2	15.4	15.9	0.50	101.9	104.5	2.68
3	1/2	24.7	24.9	0.12	80.7	81.8	1.10
4	1/3	13.4	13.6	0.21	74.3	63.6	-10.74
5	2/3	13.1	13.5	0.35	89.9	81.7	-8.28
6	1/3	14.0	14.6	0.58	60.5	55.2	-5.29
7	2/3	12.9	12.0	-0.88	78.0	70.1	-7.89
8	2/3				49.0	44.0	-5.01
9	2/3	20.3	21.4	1.06	58.9	54.6	-4.33
10 $L1_2$	1/4	13.0	13.0	0.02	90.5	89.5	-0.99
11 $L1_2$	3/4	11.3	11.1	-0.19	73.1	73.2	0.10
12 DO_{22}	1/4	13.5	13.2	-0.29	67.3	70.0	2.73
13	1/2	17.4	17.2	-0.21	80.9	83.7	2.79
14 DO_{22}	3/4	11.9	12.1	0.28	72.7	71.8	-0.85
15	3/4				56.5	58.6	2.14
16	1/2				71.8	79.9	8.14
17	1/4				61.6	62.7	1.06
18	1/4	18.2	17.5	-0.70	72.3	71.0	-1.24
19	3/4	15.5	15.5	0.00	62.9	63.5	0.66
20	1/4	11.7	12.4	0.68	54.2	56.0	1.77
21	1/2	15.4	15.1	-0.30	56.5	65.6	9.12
22	3/4	11.8	10.8	-0.92	59.7	62.3	2.63
23	1/4	12.0	12.2	0.24	41.4	41.8	0.37
24	1/2	13.6	14.2	0.62	36.1	41.7	5.67
25	3/4	9.6	10.1	0.51	51.0	52.7	1.62
26	1/4	17.7	17.4	-0.33	34.1	33.3	-0.78
27	1/2	21.4	20.9	-0.52	32.5	33.0	0.52
28	1/4				40.5	41.0	0.50
45	1/5	11.7	10.3	-1.41			
46	2/5	13.2	13.1	-0.10			

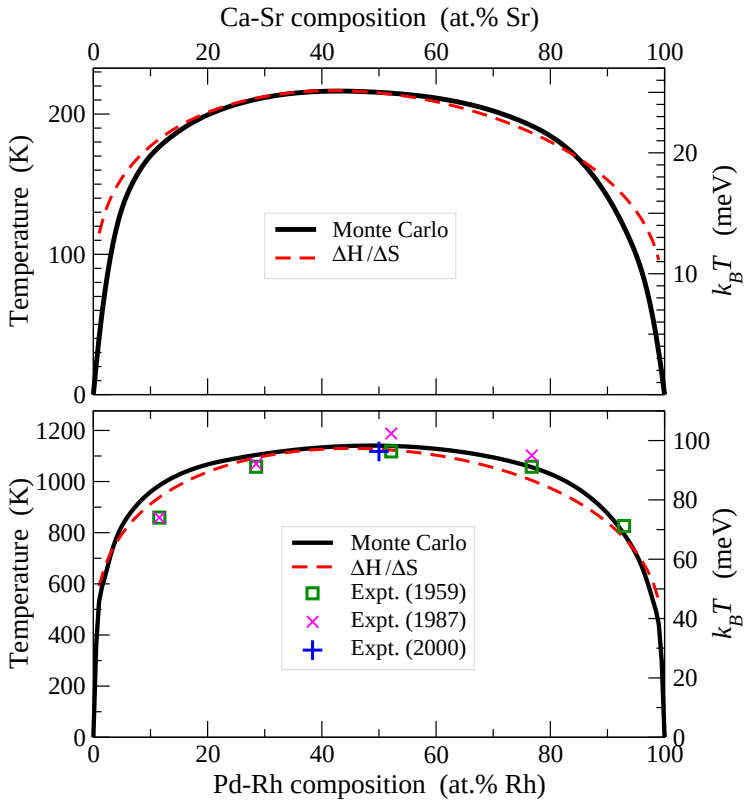

Figure 4.2: (color online) Ca-Sr and Pd-Rh T–c phase diagrams. Miscibility gap from Monte Carlo (solid line) and estimate (dashed line) from (4.2), compared to experimental data found from [25, 76, 77].

For Ca-Sr, the set including eight pair and three triplet interactions reproduces the DFT enthalpies well (see Table 4.2), with the exclude-0 (i.e., least-squares fit error), exclude-1 and exclude-2 cross-validation scores ε_0, ε_1 and ε_2 of 0.57, 1.3 and 1.4 meV/atom, respectively. Similarly, we list the Pd-Rh interactions in Tables 4.1 and enthalpies in Table 4.2), where the cross-validation errors ε_0, ε_1, and ε_2 are 4.3, 7.5, and 7.7 meV/atom, respectively. While the absolute values of the errors ε_m are several times larger for Pd-Rh, so too are T_c (see Fig. 4.2), hence, relative CE errors are similar for these two systems. In Table 4.1 we see that both systems have pair interactions that drive local clustering (negative sign) competing with triplet interactions that drive local ordering.

4.2.3 Phase Diagrams

The calculated fcc phase diagrams are shown in Fig. 4.2. The Ca-Sr alloy segregates at low temperatures into Ca and Sr, whereas the Pd-Rh alloy has nearly five times larger formation enthalpy (see Fig. 4.1) and segregates at about five times higher temperature (Fig. 4.2) due to the stronger 2-body interactions, see Table 4.1. Due to 3-body interactions, the phase boundary is slightly asymmetric versus c for both Ca-Sr and Pd-Rh, as expected from the small asymmetry of formation enthalpies.

Figure 4.2 shows phase boundaries $\mathrm{T}_c(c)$ calculated by the Monte Carlo and the rapid estimate (4.2-4.4). One can see that approximation (4.2) provides an accurate estimate for Monte Carlo T_c for Pd-Rh and Ca-Sr at all c except those near $c = 0$ and $c = 1$ where both ΔH and ΔS approach zero. For Pd-Rh both the $\mathrm{T}_c(c)$ from Monte Carlo and (4.2) agree very well with experiment [25, 76, 77].

The total error in calculated transition temperatures includes DFT, predictive, and statistical errors, with the predictive one being the largest [7]. Each error can be estimated. As explained in section 3.3.4, the predictive error in CE structural enthalpies can be estimated by the cross-validation score ε_1, but only if ε_2 is finite. We estimate an error bar on T_c (ε_1 plus 1 meV DFT and statistical errors) to be 30 K (2.5 meV) for Ca-Sr and 100 K (8.5 meV) for Pd-Rh. In Fig. 4.2 one can see that both the rapid estimate and Monte Carlo results for Pd-Rh agree with experiment [77] within the ε_1 error bar.

4.2.4 Enthalpy and Entropy Changes Versus T and c

As noted earlier, the exact T_c can be found from (4.1) via the ratio of $\Delta H(T_c)$ and $\Delta S(T_c)$, which are the enthalpy and entropy differences, respectively, between two phases coexisting at T_c. With $0 < \kappa < 1$, we define

$$\Delta H(\kappa) \equiv H(T_c/\kappa) - H(\kappa T_c), \tag{4.9}$$

and similarly for the entropy. The limits of (4.9) are

$$\lim_{\substack{\kappa\to 0\\ \kappa\to 1}} \Delta H(\kappa) = \begin{cases} H_d(\infty) - H_o(0) \equiv \Delta H_{d-o} \\ H(T_c^+) - H(T_c^-) = \Delta H(T_c) \end{cases} \tag{4.10}$$

where the $\kappa \to 0$ limit is analytically obtained from the CE and $\kappa \to 1$ limit is from careful Monte Carlo calculations. The calculated $\Delta H(\kappa)$, $\Delta S(\kappa)$, and their ratio for $Pd_{75}Rh_{25}$ are shown in Fig. 4.3. Clearly, the ratio $\Delta H(\kappa)/\Delta S(\kappa)$ does not strongly depend on κ. Thus,

$$T_c = \frac{\Delta H(\kappa = 1)}{\Delta S(\kappa = 1)} \approx \frac{\Delta H(\kappa = 0)}{\Delta S(\kappa = 0)} \equiv \frac{\Delta H_{d-o}}{\Delta S_{d-o}}. \tag{4.11}$$

However, T_c^{est} from (4.2) is invalid near $c = 0$ and 1 due to $\Delta H(T)$ and $\Delta S(T)$ approaching zero with different asymptotics. In Figs. 4.3 and 4.4 $\langle H \rangle$ and C_v were calculated as given in Sec. 4.1.3. Figure 4.4 shows the calculated ratio $\Delta H(\kappa, c)/\Delta S(\kappa, c)$ at fixed κ of 0.93 versus c. One can see that the relative differences $\Delta H(\kappa)/H_{d-o}$ and $\Delta S(\kappa)/S_{d-o}$ at most compositions are the same. Thus the ratio of $[\Delta H(\kappa)/\Delta S(\kappa)]$ to $[H_{d-o}/S_{d-o}]$ is roughly 1, except near $c = 0$ and 1 for reasons stated above.

Together the results from Figs. 4.2–4.4 show that (4.2) provides reliable estimates for the segregating alloys, if, in addition, the difference in electronegativity of the constituting elements is small (which implies vibrations are not important, as discussed below). Segregation can be ascertained in a cluster expansion from disordered enthalpy before any Monte Carlo simulations are performed.

In summary, in alloys where vibrational effects are unimportant we have shown that an analytic, mean-field estimate from the cluster expansion given by T_c^{est} in (4.2) is accurate and involves no simulation — useful for rapid design estimates. Via Monte Carlo based thermodynamic integration, we illustrated the validity of this estimate versus composition and temperature scale. Below, we contrast this with the Bethe (pair-only) mean-field theory that becomes exact for infinite-ranged pair interactions, and show that without competing interactions the T_c^{est} is inaccurate. We then discuss the effects of vibration on the prediction of T_c.

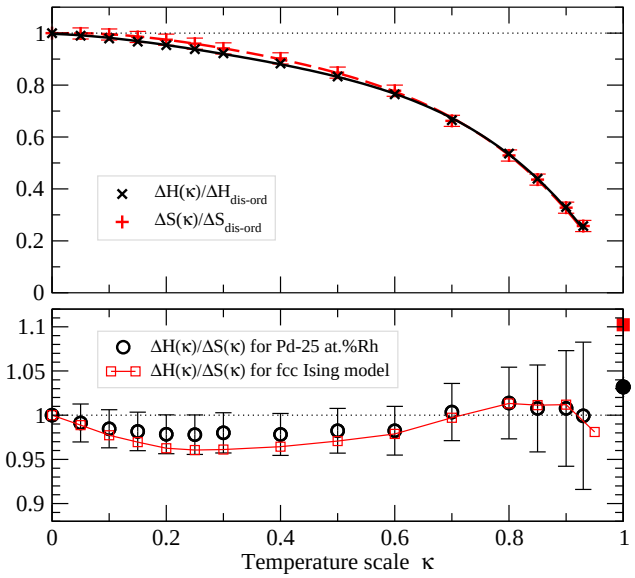

Figure 4.3: (color online) For $Pd_{75}Rh_{25}$ using (4.9), enthalpy $\Delta H(\kappa)/\Delta H_{d-o}$, entropy $\Delta S(\kappa)/\Delta S_{d-o}$, and their ratio (circles), along with same results for the fcc nearest-neighbor pair Ising model (squares). Filled symbols at $\kappa = 1$ are Monte Carlo T_c relative to $(\Delta H_{d-o}/\Delta S_{d-o})$. Results are obtained using a fixed 24^3-atom periodic box. Error bars are given and lines are a guide to eye.

4.3 Discussion

4.3.1 Comparison to Previous Results

Unlike fcc Ca-Sr, Pd-Rh was previously studied both experimentally [75–77] and theoretically [78–80]. Disordered fcc Pd-Rh has been studied via first-principles multiple-scattering theory combined with the coherent-potential approximation (KKR-CPA) for direct calculation of formation enthalpies of the homogeneously disordered state [79]. Even though obtained within the atomic-sphere approximation to the potentials, the previous KKR-CPA enthalpies [79] agree well with our present full-potential results. Also, the KKR-CPA enthalpies were used to find the phase boundary via approximation (4.2), also in reasonable agreement with experiment [79].

Pd-Rh was also studied by a CE with interactions fitted to the tight-binding linear muffin-tin orbital results [80]. The difference between the present structural formation enthalpies and the former [80] ones are presumably due to a more approximate electronic-structure method used. The previous phase diagram [80] calculated by combining the CE

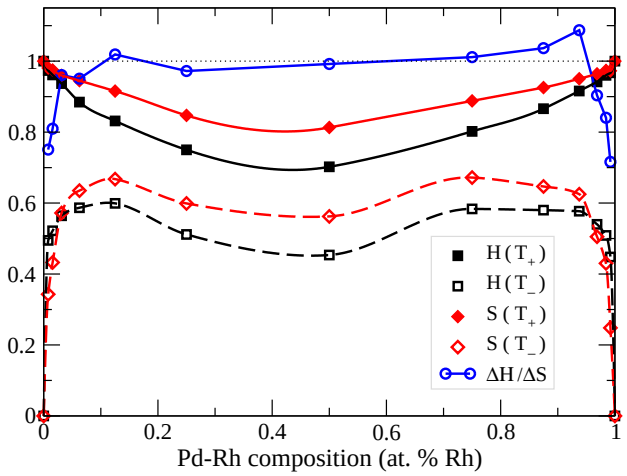

Figure 4.4: (color online) Composition dependence of $H(T_c^+, c) = H(T_c/\kappa, c)$ and $H(T_c^-, c) = H(\kappa T_c, c)$ relative to ΔH_{d-o}, $S(T_c^+, c)$ and $S(T_c^-, c)$ relative to ΔS_{d-o}, and the ratio $\Delta H(\kappa, c)/\Delta S(\kappa, c)$ relative to $\Delta H_{d-o}(c)/\Delta S_{d-o}(c)$ for $\kappa = 0.93$. Lines are a guide to the eye.

with the cluster variation method using the tetrahedron-octahedron approximation found fair agreement with experiment; larger deviation from experiment are presumably due to the use of less accurate enthalpies.

Au-Rh was studied experimentally [89–92] and theoretically [93], where it was noted that Au-Rh has no stable compounds, but no phase diagram was calculated. The calculated formation enthalpy [93] of the lowest-energy $AuRh_3$ is 91 meV/atom, which compares well to our 88 meV/atom for the same structure (same as structure 23 noted in Section 3.3.1). Au-Pt was studied in [92, 94–97], and Ag-Rh was addressed in [98–101]. The previously calculated lowest formation enthalpies [93] of Au_2Pt (9 meV/atom) and $AgRh_3$ (116 meV/atom) agree with our results of 16 and 114 meV/atom, respectively, if it is noted that we used higher plane-wave energy cutoff and four times denser k-point mesh (k-point convergence is not monotonic). In general, CE can be used to search for new ground states in ordering alloys, and to confirm their absence in phase-segregating systems.

4.3.2 Influence of Other Phases

As noted earlier, liquid phase is important in the (Cu,Ag,Au)-Rh and Au-Pt systems, hence, without addressing at least the density (i.e., volume) changes of the liquid phase and its

reduction in segregation energetics, we can not make a direct comparison to experiment. In general, all possible phases, structures, and states s contribute to the statistical sum $\sum_s \exp(-E_s/k_BT)$, but contributions of higher-energy structures are exponentially suppressed. If all low-energy structures belong to one and the same lattice, and contributions from all other high-energy phases are negligibly small, then the fixed-lattice cluster expansion works well and provides high-accuracy predictions, as is the case for Ca-Sr and Pd-Rh. However, this is not always the case. For example, when a (predicted) solid-solid transition temperature is comparable to (or exceeds) a melting temperature, influence of a liquid phase is significant. The CE takes into account only one crystalline phase, and can provide inaccurate predictions if contributions from other phases (such as the liquid phase) are also important.

To illustrate this, we consider Rh-(Cu,Ag,Au) and Au-Pt alloys, see Fig. 4.5 and Table 4.5. In Cu-Rh and Au-Pt, T_c^{expt} and T_{melt}^{expt} are very close (within 20%), while in Ag-Rh and Au-Rh the predicted T_c exceeds T_{melt}^{expt}. Note, that if only two phases (such as solid-solution and liquid) contribute significantly, and only one of them is taken into account by a CE (i.e., the fcc-based solid solution here), then the prediction is usually roughly within a factor of 2 from the correct result. Although in such systems the CE-based quick estimates and Monte Carlo results are still in some agreement with each other, the CE itself here does not account properly for the liquid thermodynamic contributions. In Ca-Sr and Pd-Rh only one fcc crystalline phase is important at relevant temperatures, hence $T_c \ll T_{melt}$, the CE works, $T_c^{est} \approx T_c^{MC}$, and for Pd-Rh both agree with experiment. In Cu-rich Cu-Rh, $T_c \ll T_{melt}$ and the CE should be correct, if vibrational contributions are also included, see below.

4.3.3 Comparison to the Bethe Theory

Having shown that the rapid estimate in (4.2) works well for the Ca-Sr and Pd-Rh systems, the Bethe (pair-only) approximation could also be used to estimate T_c quickly, but not reliably. Also, generally, due to topological frustration, the Bethe approximation does very poorly on fcc-based alloys with antiferromagnetic (ordering) interactions [86,102]. Table 4.3

Table 4.3: Ratios of T_c to T_c^{Bethe} from (4.6) and T_c^{est} from (4.2) for different ranges of interactions for 50% composition. We used $\widetilde{V}_{2f}$s from Pd-Rh in Table 4.1.

No. of V_{2f}	T_c/T_c^{Bethe}	T_c/T_c^{est}
1	0.886	1.12
4	0.889	1.13
∞	1.00	1.39

compares estimate T_c^{est} from (4.2) and T_c^{Bethe2} from (4.6). The ratios of T_c (obtained from Monte Carlo with careful finite-sized scaling analysis) to each of the estimates is calculated for three different sets of pair interactions. For the first two sets we used $\widetilde{V}_{2f}$ with the number of neighbor shells N taken as 1 and 4, respectively, from Pd-Rh in Table 4.1 and q_{eff} is calculated from (4.7). The third case takes the first nearest-neighbor value for Pd-Rh in Table 4.1 for all $\widetilde{V}_{2f}$, i.e., -55.13 meV (constant) and negative (clustering), with $N \to \infty$, which is calculated analytically.

Table 4.3 shows that the Bethe approximation improves marginally when a few pairs beyond the nearest-neighbor are added. However, in the third case, as N becomes infinite with V_{2f} being constant and negative, where mean-field theory is exact [31], T_c/T_c^{Bethe} is indeed 1. Hence, the Bethe approximation improves as more pair-interactions favoring phase segregation are added.

In contrast T_c^{est} becomes increasingly worse compared to T_c as more pairs are added. For the third case, where the Bethe approximation is exact, T_c^{est} has a significant error of 39%. In addition, we note that T_c^{est} produces an error of 11% when multibody interactions are just ignored in the CE of Pd-Rh given in Table 4.1. Also, we note that a similar proportional change of the entropy and enthalpy versus temperature is found for a pair-only model (we focus on the Ising model), see Fig. 4.3. However, as is clear in Fig. 4.3, the Monte Carlo T_c is 11% larger than the T_c^{est}, in contrast to a multibody case. Taking into account of finite-size scaling, the original CE in Table 4.1 gives T_c/T_c^{est} of 1.06 (1.03 for a fixed-size 24^3-atom box, see Fig. 4.3), suggesting that the presence of the competing multibody interactions is needed for estimate (4.2) to be reliable. Lastly, we find that T_c^{est} works well for certain classes of ordering systems too. However, this is beyond the scope of this thesis.

4.3.4 Effects of Vibrational Entropy Changes on T_c

Up to this point our results have focused on how well T_c^{est} reproduced the time-consuming Monte Carlo results for virtually no cost, as it is obtained directly from the cluster expansion analytically, for the cases where no vibrational effects are included. Vibrational effects add a higher level of complexity and difficulty, as they are as time-consuming computationally as a cluster expansion. It can be shown (e.g., see [54] or [12]) that T_c is altered by changes in harmonic vibrational entropy $\Delta S_{vibr}^{\alpha\to\beta}$ from the $\alpha-\beta$ phase transition from solely configurational contributions $T_{c,conf}^{\alpha\to\beta}$ in (4.1), and can be accounted for in the analysis of T_c^{est} in (4.2), as

$$T_c^{\alpha\to\beta} \approx T_{c,conf}^{\alpha\to\beta}\left(1+\frac{\Delta S_{vibr}^{\alpha\to\beta}}{\Delta S_{conf}^{\alpha\to\beta}}\right)^{-1}. \tag{4.12}$$

For phase-segregating systems studied here $\Delta S_{conf}^{\alpha\to\beta}$ is ΔS_{d-o} from (4.3). The more correct and computationally expensive quasiharmonic corrections to vibrational entropy, i.e. $\Delta_{QH} = (\Delta S_{QHvibr} - \Delta S_{vibr})/2$, account for the effects of thermal expansion, which typically increase the lattice constant as temperature increases and, thus, decreases the phonon modes contributing to (4.12), and lead to $\sim 50\%$ decrease in the harmonic contributions [103].

From (4.3), the configurational entropy per atom ΔS_{conf}^{max} for a binary is bounded because

$$0 \le \Delta S_{conf}^{max} \le -k_B \sum_{n=1}^{2} c_n ln c_n \le k_B ln 2, \tag{4.13}$$

This expression is generalized easily to multicomponent cases, just like for T_c^{est}. Equations (4.12) and (4.13) provide an absolute scale to judge the importance of the vibrational effects on T_c. Equally important, $\Delta S_{vibr}^{\alpha\to\beta}$ can, in principle, be larger in magnitude than $\Delta S_{conf}^{\alpha\to\beta}$, and, moreover, it can be both positive (reducing T_c) or negative (increasing T_c), as evidenced by numerous examples (e.g., see [12] and references therein).

Here are a few examples for $\Delta S_{vibr}^{\alpha\to\beta}$ (in k_B units): From experiment, Delaire, Swan-Wood and Fultz [104] found negative values for V-6.25%Ni, Pd, Pt alloys, from -0.082, -0.185, and -0.272 (all ± 0.005), respectively, while for concentrated alloys [105], Cu_3Au is 0.12 ± 0.03, Fe_3Pt is 0.55 ± 0.03 and $CeSn_3$ is -0.54 ± 0.09. From theory, for example, Cu_3Au

is ~ 0.06 [103]. In addition, there are many approximations that have been attempted to reduce the needed phonon calculation [12], most notably a simple Grüneisen theory [106]. However, these have met with limited success for alloys. For example, some alloys are described by a near-neighbor bond-stretching and bond-bending model [12], whereas in dilute $Al_{26}Sc$ the vibrational entropy is $+0.50$ and arise due to longer-ranged neighbors [18, 107]. Note also that for Al-Sc the vibrational entropy is larger than that possible from configurational effects alone. For a more complete picture see the review by van de Walle and Ceder [12].

Importantly here, however, are recent experimental findings of Delaire and Fultz [108]. For vanadium-based alloys with 6.83%X, where X is taken from 3, 4 and 5d transitional metals, they found that *the change in vibrational entropy due to alloying showed a linear correlation with the difference in electronegativity of the constituent elements* ($\Delta\chi = \chi_{solute} - \chi_{host}$), rather than mass difference, or other possible factors. Essentially, the difference in electronegativity reflects the potential change in local bonding, and, hence, change in bond stiffnesses. The least-squares, linear relation they found was

$$\Delta S^{\chi}_{vibr} = -0.34\Delta\chi \ (\pm 0.06\Delta\chi). \tag{4.14}$$

In addition, reanalysis of their previous results on $L1_2$ metals [109, 110] shows that the ΔS^{χ}_{vibr} correlation works [108], but seems less correct for f electron systems, where even the cluster expansion appears to be more problematic.

Table 4.4 lists the elemental electronegativities χ, and other basic properties, to determine for which systems vibrations might be important. For example, bulk modulus reflects the charge density (hence bonding) at the Wigner-Seitz radius [112]. Let us compare ΔS^{χ}_{vibr} to those already mentioned. For V-Ni and V-Pd, for example, with $\Delta\chi$ of 0.28 and 0.57, ΔS^{χ}_{vibr} is -0.10 ± 0.017 and -0.19 ± 0.034, respectively, in good agreement with experimental values. For Cu_3Au, $\Delta\chi$ is -0.5, so ΔS^{χ}_{vibr} is 0.17 ± 0.03, compared to 0.12 ± 0.03 from above.

Clearly, there is much to be understood in regards to this simple correlation and how it can be used for concentrated alloys, especially its variation with composition and type

Table 4.4: Elemental configurations of valence electrons, atomic numbers Z, electronegativities χ, fcc lattice constants a (Å), and bulk moduli B (MPa) for the relevant alloys [111].

electrons	Z		χ	a	B
$5s^2$	38	Sr	0.95	6.08	0.118
$4s^2$	20	Ca	1.00	5.58	0.115
$3d^3 4s^2$	23	V	1.63	3.03	1.65
$3d^{10} 4s^1$	29	Cu	1.90	3.62	1.335
$3d^8 4s^2$	28	Ni	1.91	3.53	1.90
$4d^{10} 5s^1$	47	Ag	1.93	4.09	0.981
$4d^{10} 5s^0$	46	Pd	2.20	3.89	1.844
$5d^{10} 6s^0$	78	Pt	2.20	3.92	2.838
$4d^8 5s^1$	45	Rh	2.28	3.80	2.758
$5d^{10} 6s^1$	79	Au	2.40	4.08	1.766

of order. However, the relevant point is that this approximate correlation permits a quick assessment of when vibrational contributions to T_c can be expected to be important. A synopsis of the transition temperatures for the five alloy systems studied are given in Table 4.5, along with ΔH_{d-o} and $\Delta\chi$.

Clearly, from Table 4.5, based upon the correlation with $\Delta\chi$, Ca-Sr and Pd-Rh should have little effect from changes in vibrational modes. Indeed, for Pd-Rh our Monte Carlo and rapid estimate results considering only configurational effects are in good agreement with experiment, as already described. Configurational effects consider only solid-on-solid transformation, which is solid-solution versus segregated state in the present cases. As noted earlier, the stability of the liquid phase is important in the (Ag,Au)-Rh systems, where the predicted T_c exceeds Ag or Au melting temperature T_{melt}.

Importantly, for Cu-rich $Cu_{75}Rh_{25}$ where Rh is solute, ΔS^{χ}_{vibr} is found to be $-0.129\,k_B$ (using data from Table 4.5), yielding a 30% increase in the configuration-only T_c^{MC} value from (4.12) at 25% Rh, i.e., from 882 K to 1145 K, which is now close to the experimental value of 1103 K, see Table 4.5. Again, how this simple correlation may be used as concentration progresses from 0 to 1, where the "solute" and "host" should change identity, is unclear. Nonetheless the correlation appears to work well, at least within the error in DFT and its vibrational-entropy estimates.

Table 4.5: ΔH_{d-o} (in meV), T_c (in K) from from (4.2), Monte Carlo, and experiment, and percent difference δ (in %) between estimate and Monte Carlo values, for Ca-Sr, Pd-Rh, (Cu,Ag,Au)-Rh, and Au-Pt. $\Delta\chi$ is the difference in the electronegativity of the elements, see text.

	ΔH_{d-o}	T_c^{est}	T_c^{MC}	T_c^{expt}	T_{melt}^{expt}	$\delta\%$	$\Delta\chi$
Ca-Sr							0.05
$Ca_{0.75}Sr_{0.25}$	13.6	280	279		1043	0.4	
$Ca_{0.50}Sr_{0.50}$	17.3	290	290		1011	-0.2	
$Ca_{0.25}Sr_{0.75}$	12.4	256	261		1023	-2.1	
Pd-Rh							0.08
$Pd_{0.75}Rh_{0.25}$	52.0	1074	1091	1033	1913	-1.5	
$Pd_{0.50}Rh_{0.50}$	67.3	1126	1137	1118	2013	-0.9	
$Pd_{0.25}Rh_{0.75}$	49.4	1019	1068	1073	2113	-4.5	
Au-Rh							0.12
$Au_{0.75}Rh_{0.25}$	107.3	2214	2657		1339	-16.7	
$Au_{0.50}Rh_{0.50}$	158.6	2655	2924		1339	-9.2	
$Au_{0.25}Rh_{0.75}$	121.5	2507	2785		1339	-10.0	
Au-Pt							0.20
$Au_{0.75}Pt_{0.25}$	26.1	539	615	1103	1493	-12.4	
$Au_{0.50}Pt_{0.50}$	46.3	776	1021	1513	1573	-24.1	
$Au_{0.4}Pt_{0.6}$	49.2	853	1073	1533	1593	-20.5	
$Au_{0.25}Pt_{0.75}$	45.3	935	1114	1473	1613	-16.1	
Ag-Rh							0.35
$Ag_{0.75}Rh_{0.25}$	148.8	3070	3412		1235	-10.0	
$Ag_{0.50}Rh_{0.50}$	213.2	3570	3586		1235	-0.4	
$Ag_{0.25}Rh_{0.75}$	171.1	3531	3597		1235	-1.9	
Cu-Rh							0.38
$Cu_{0.75}Rh_{0.25}$	31.4	647	882	1103	1533	-26.6	
$Cu_{0.50}Rh_{0.50}$	53.5	896	998	1413	1593	-10.2	
$Cu_{0.4}Rh_{0.6}$	53.4	920	1039	1423	1613	-11.4	
$Cu_{0.25}Rh_{0.75}$	41.9	865	1068	1363	1753	-19.0	

4.3.5 ΔH^F of Rh-(Cu,Ag,Au) and Au-Pt

For completeness, we provide the formation enthalpy results in Fig. 4.5 for various structures at a few concentrations for Au-Pt and Rh-(Cu,Ag,Au) alloys. The similarity to the Ca-Sr and Pd-Rh as far as formation enthalpies are concerned is clear. The numerical results for stoichiometric compositions appear in Table 4.5.

In brief, Au-Pt and Cu-Ru show clear asymmetry in the formation enthalpies, see Fig. 4.5. For Au- and Ag-Rh systems the formation enthalpies, such as for ΔH_{dis}, are very symmetric. Table 4.1 shows the interactions of Au-Pt and Cu-Ru compared to Ca-Sr and Pd-Rh. As expected, due to the asymmetry in the formation enthalpies, there are more significant contributions from multibody interactions. However, more interestingly, the Au-Pt or Cu-Ru pair interactions are of ordering-type, rather than clustering as in Ca-Sr and Pd-Rh. It is the multibodies that are responsible for global clustering, as determined by the sign of the interactions – negative (positive) is clustering (ordering). Ordering or phase-segregation are driven by electronic effects [113,114], especially size-effect due to electronic hybridization. Note that the DFT and CE agree very well in Au-Pt system, better than any of the other Rh-(Cu,Ag,Au) systems, showing that the multibodies are critical to reproduce the DFT values. And, as noted in the main text, metastable Au_3Pt has been observed in highly cold-worked Au-rich Au-Pt, and indeed we find that the [100]-layered A-A-A-B structure (23 in Sec. 3.3.1) has the lowest formation enthalpy (see Fig. 4.5), in contrast to metastable Au_2Pt structure 9 in [93].

The simple estimate T_c^{est} can have larger error, see Table 4.5, when the systems exhibit positive curvature in ΔH_{dis}, as happens in both Cu-rich Cu-Rh and Au-rich Au-Pt, which may explain the larger discrepancy between T_c^{est} and T_c^{MC}, as we are investigating. This change in curvature arises from important multibody interactions at dilute concentrations.

4.4 Summary

Using first-principles density-functional theory, we calculated the enthalpies of a set of fcc-based phase-segregating alloy systems, found interatomic interactions via the cluster

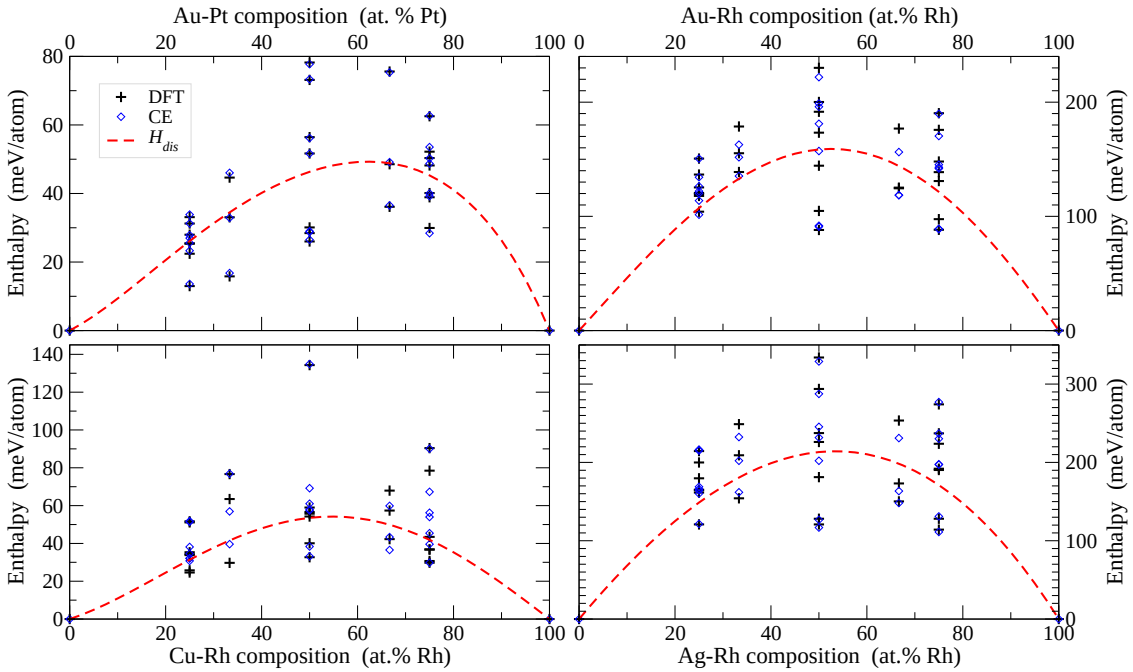

Figure 4.5: (color online) ΔH^F (in meV/atom) versus c for the fcc Au-Pt and Rh-(Au,Ag,Cu) alloys, with symbols as in Fig. 4.1. Ag-Rh and Au-Rh have 3–4 times larger H_d than Au-Pt or Cu-Rh. Cu-Rh and Au-Pt have similar asymmetry, with the predicted maximum of $H_d(c)$ as observed in T_c vs c, see text. Important influence of liquid phase is discussed in Sec. 4.3.2.

expansion method, and determined the transition temperatures (T_c vs. c) from Monte Carlo and a rapid mean-field estimate. We predicted that Ca-Sr should segregate at low temperatures, yet to be observed. As validation of our predictions and rapid estimate, we found that Pd-Rh segregates, as is well known, and our T_c results are in excellent agreement with experiment. In addition, we showed that a rapid mean-field estimate of T_c from the ratio of enthalpy and entropy differences between the fully-disordered and fully-ordered states (obtained analytically within the cluster expansion) agrees well with the Monte Carlo results, permitting rapid design estimates *without* time-consuming Monte Carlo simulations. Using thermodynamic integration, we explained why and when the rapid estimate is accurate and reliable. Finally, we discussed how the difference in constituent electronegativites can be used to assess when vibrational entropy should be considered when predicting solid-solid transformations, such as the phase-segregation studied here. For Ca-

Sr and Pd-Rh, the configuration-only T_c were shown to be quite good, whereas in Cu-rich Cu-Rh, vibrations were estimated to result in a 30% increase in the configuration-only T_c, which then agreed with experiment. How these simple and rapid design-estimate results extend to ordering systems is a part of our ongoing research.

CHAPTER 5

ORDERING AND PHASE STABILITY IN FRUSTRATED FCC ALLOYS: CASE STUDY OF Ag-Au

Frustrated systems are not only intriguing mathematical models, they can describe interesting physical phenomena (such as chemical or magnetic ordering) in many important materials, including alloys, magnetic systems, and superconductors [115–130]. On the other hand, (re)discovery of the chains of long-period superstructures (LPS) on the groundstate hulls in the formation energy versus concentration has attracted significant interest [3, 4, 131–139]. These LPS are linear combinations of the bounding, most stable stoichiometric groundstates, and arise due to short-range chemical interactions that do not distinguish between such structures and lead to zero-energy planar (antiphase boundary – APB) defects. In this chapter we investigate systems with internal frustration, and show that existence of the low-energy [zero-energy] APB results in similar-energy [degenerate] structures, some of which are the groundstates, while others look like superposition of the ground states, forming chains of LPS on the ground-state hull. The discussions in this chapter is also available in [56].

5.1 Introduction

An example of a frustrated system is a nearest-neighbor (NN) pair Ising model with ordering (antiferromagnetic) interactions on a close-packed triangular or face centered cubic (fcc) lattice, where the binary alloy exhibits so-called "superdegeneracy" [140–146] due to the above effects – with a narrowed $L1_2 + L1_0$ coexistence region compared to a typical fcc alloy phase diagram. Because the NN pair is the dominant (strongest) interaction in most alloys and many metals have a close-packed lattices, understanding frustration in a "simple" fcc Ising model is crucial for understanding similar phenomena in real alloys, especially ones

that have small, but non-negligible, multibody or longer-ranged pair interactions that alter the phase diagram topology significantly.

As a prototype of a close-packed alloy with dominant NN pair interaction, we consider fcc Ag-Au. Using density-functional theory (DFT), we calculate pair and multibody interactions in Ag-Au directly using large supercells, and show how they originate from the electronic density.

Here we compare the interactions obtained from the CE, whose implementation via TTK is detailed in Section 3.3, and those found directly from DFT calculations involving supercells. This allows us to visualize the electronic density related to the effective interactions obtained from CE, demonstrating that CE interactions give physical insight, provided that a complete and compact basis [6] is retained, as opposed to a CE with "holes" in the basis set [59]. We calculate the energetics of millions of structures to predict groundstates and study phase stability, including how small breaking of the degeneracies (as in Ag-Au alloys) affect the phase diagrams. We use the interactions within a lattice Monte Carlo (MC) program to study thermodynamics and to construct phase diagrams. We emphasize that frustrated systems with degenerate LPS can have phase coexistence instead of phase segregation in clustering systems, which is narrower in nearest-neighbor pair dominated CE. The direct extraction of chemical interactions via large DFT supercell calculations is discussed next

5.2 Cluster Expansion Method: Additional Details

Because Ag-Au has stable ordered structures, in addition to the structures generated by 'smallest-first' algorithm discussed in Section 3.3.1, an iterative procedure is used to search for other possible ground states or low-energy structures. In the first iteration, we use the DFT energies of the first 29 structures from 'smallest-first' algorithm to construct the initial CE. A ground state search over millions of possible structural configurations (with up to 20 atoms per unit cell) is conducted using the CE enthalpies. Energies of any new CE-predicted ground states are then confirmed by DFT. The latter are added to the pool of DFT enthalpies to construct a new CE for the ground state search in the subsequent iteration.

The above iterative process stops when the final CE does not predict any new ground states and finally we have a total of 55 Ag-Au structural energies from DFT calculations.

The optimal truncated CE selected from the 55 Ag-Au structural energies via the procedure in Section 3.3.4. For comparison, we also fit the same set of DFT enthalpies to other (not optimal) selected cluster sets, including NN pair only (Ising model), and compact NN clusters (pair, triplet, and quadruplet) used in the tetrahedron approximation [147–149] within the cluster variation method (CVM) [45, 47], which can then be compared to the interactions determined directly.

Lattice MC simulations, as implemented within TTK, are performed in periodic boxes with 16^3 (4096) to 32^3 (32768) atoms, with 4000-25000 sampling steps and 1000-16000 equilibriation steps (largest values are for lowest temperatures). Phase transitions are determined from either fixed composition (variable temperature) or fixed temperature (variable chemical potential) MC runs (see section 2.3.1), using heat capacity versus temperature or chemical potential versus composition.

5.2.1 Extracting Interactions from Supercells

To calculate directly the n-body NN interactions of Au solutes in fcc Ag, we carried out DFT calculations with NN Au dimer, trimer and tetramer on an fcc Ag lattice. A cubic cell of 32 atoms (i.e., 2×2×2 fcc 4-atom cells) with 8.30 Å in each dimension was used to exclude the interactions of Au atoms or clusters with their periodic images. All convergence criterion were the same as for the concentrated alloys, using an 8×8×8 k-point mesh.

In this way we can calculate the DFT energies of fcc Ag $E_{(0)}$ as well as the Au monomer $E_{(1)}$, dimer $E_{(2)}$, trimer $E_{(3)}$ and tetramer $E_{(4)}$ embedded in fcc Ag. These energies can be

expressed in terms of the NN ($f = 1$) $n-$body interactions $\tilde{V}_{n1}$ as follows:

$$\begin{aligned} E_{(0)} &= \tilde{V}_{01} \\ E_{(1)} &= \tilde{V}_{01} + \tilde{V}_{11} \\ E_{(2)} &= \tilde{V}_{01} + 2\tilde{V}_{11} + \tilde{V}_{21} \\ E_{(3)} &= \tilde{V}_{01} + 3\tilde{V}_{11} + 3\tilde{V}_{21} + \tilde{V}_{31} \\ E_{(4)} &= \tilde{V}_{01} + 4\tilde{V}_{11} + 6\tilde{V}_{21} + 4\tilde{V}_{31} + \tilde{V}_{41} \end{aligned} \tag{5.1}$$

Conversely, the NN interactions are linear combinations of the above energies:

$$\begin{aligned} \tilde{V}_{01} &= E_{(0)} \\ \tilde{V}_{11} &= -E_{(0)} + E_{(1)} \\ \tilde{V}_{21} &= E_{(0)} - 2E_{(1)} + E_{(2)} \\ \tilde{V}_{31} &= -E_{(0)} + 3E_{(1)} - 3E_{(2)} + E_{(3)} \\ \tilde{V}_{41} &= E_{(0)} - 4E_{(1)} + 6E_{(2)} - 4E_{(3)} + E_{(4)} \end{aligned} \tag{5.2}$$

These values represent cluster interactions at dilute concentrations of Au determined directly and can be put into Eq. (3.4) to predict the enthalpy of a given structure. The root-mean-squared (rms) error between this prediction and DFT is shown in Table 5.1.

5.3 Results and Discussion

5.3.1 Ground States and Effective Interactions

Using the iterative procedure described in section 5.2, we find an optimal CE that accurately represents the DFT results, as shown in Fig. 5.1, where the CV1 score (a measure of predictive error) is 0.47 meV, and CV0 (least-squares error) is 0.28 meV. From the CE we also predict the homogeneously (fully) disordered phase and the lowest-energy structures, see Fig. 5.1. The latter are connected to form the groundstate "hull" of the formation enthalpy vs. composition plot (so named because it resembles the hull of a ship). The difference

between groundstates and fully-disordered enthalpies at fixed composition determines the temperature scale of the order-disorder transition [8]. In addition, the CE permits direct prediction of millions higher-energy structures, discussed below, and shown in Fig. 5.2. In what follows, we use the "smallest-first" algorithm [8,65,66] for structure enumeration, see section 2A in [8].

As is evident in Fig. 5.2(b), CE predicts that chains of structures occur on the Ag-Au groundstate hull, some of which are verified by DFT in Fig. 5.1. Well-distinguished groundstates at $c = 1/4$ (Ag_3Au), 1/2 (AgAu), and 3/4 ($AgAu_3$) are $L1_2$, $L1_0$, and $L1_2$ structures, respectively. The chains of superlattice structures (previously referred to as "adaptive" structures [4]) along the hull are created by linear combinations of smaller stoichiometric groundstate structures with low-energy APB. This results in a large number of degenerate "superstructures" at fixed composition. In addition, when the APB costs exactly zero energy, an infinite number of degenerate states occur, called superdegeneracy in the Ising model [140–142, 145, 146].

We find that there is a very small (below 1 meV/atom) energy difference between structure #2 ($L1_0$-AgAu) and structures #434, 1643, 1644, 8135, and 8375 at $c = 1/2$; between #10 ($L1_2$-Ag_3Au) and LPS #12 (DO_{22}), 425, 8074, 8321 at $c = 1/4$; and between #11 ($L1_2$-$AgAu_3$), 437 and 8388 at $c = 3/4$. Such small energy differences between the groundstates and competing structures are due to the low APB energies and allow formation of the chains of LPS on or near the groundstate hull, see Fig. 5.2.

Being a feature of the frustrated fcc (zero-energy APB) Ising model [143,144], such LPS chains on the groundstate hull are also expected to form in any fcc alloys with dominant NN interactions; Ag-Au is only one example of such alloys [51, 55, 150–152]. In particular, hP6 structure (space group P6/mmm, no. 191) at $c = 1/6$ can be viewed as a linear combination of $L1_2$ at $c = 1/4$ and $A1$ at $c = 0$; hence, it is located on the line connecting those groundstates. A non-zero APB energy from longer-range interactions introduces a curvature to this line of LPS, either removing them from the groundstate hull or forming chains of new ground states with a positive curvature. For example, Ag-Au does not have ground states at $3/4 < c < 1$ in Fig. 5.1, but has many structures close to the groundstate

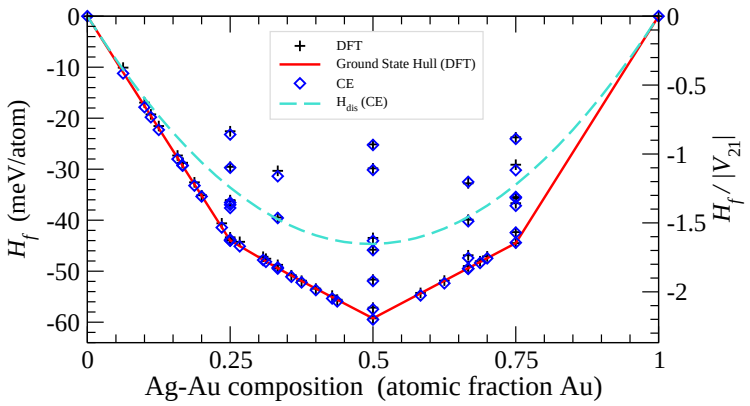

Figure 5.1: (color online) Formation enthalpies of 55 fcc Ag-Au structures from DFT (crosses) and optimal CE (diamonds), with interactions in Table 5.1. Enthalpies for ground-states [solid (red) line] and fully-disordered states [dashed line] are shown.

hull at compositions $0 \leq c \leq 3/4$. Similar "adaptive" structures are also predicted for the fcc Cu-Au and Ni-Pt alloys [4]. We emphasize that the NN-pair interaction is dominant in many alloys, and many metallic alloys have close-packed fcc or hcp lattices; hence, there are many alloys exhibiting chains of structures on their ground-state hulls. Our results are quite general and applicable to any fcc system, which can be described as a frustrated Ising model with added longer-range perturbations. Note, however, that multibody interactions actually can screen the larger, short-ranged pair interactions, sometimes dramatically, see, e.g., [153].

Ag-Au interactions $\tilde{V}_{nf}$ are displayed in Table 5.1. For completeness, the values of $\tilde{V}_{01}$ (constant) and $\tilde{V}_{11}$ (point cluster) are reported, although they do not affect the ordering temperatures nor the topology of the phase diagrams. The NN pair interaction $\tilde{V}_{21}$ is clearly dominant. The longer-range pair and multibody interactions in Ag-Au are small, but they are numerous and their aggregated effect is not negligible. For example, a restricted CE using only NN tetrahedron (and its subclusters) has a 4-body interaction that is opposite in sign to the optimal CE; this sign change depresses the transition temperature compared to the optimal CE, see Table 5.2, and changes topology of the phase diagram. Longer-range interactions introduce non-zero energy APBs, reducing or removing degeneracy. For Ag-Au, those APB energies are small due to small interactions. Due to the compositional effect, there is clearly still a large degeneracy in the Ag-rich side while the degeneracy is lost

Table 5.1: $\tilde{V}_{nf}$ (in meV) and their degeneracies D_{nf} for fits to Ag-Au using the cluster expansion with optimal (CE), compact NN-tetrahedron only (CE-T), NN-pair only (CE-P), and NN pair and triplet restricted to structures with $0 \leq c \leq 1/4$ (CE-R). Interactions from DFT supercell calculations (direct) are provided also. CV1 and CV0 scores for each CE fit are given to assess errors, along with rms error between the enthalpy predictions from the direct and DFT for 55 (in parentheses, 19 of 55 for $0 \leq c \leq 1/4$) structures.

			$\tilde{V}_{nf}$ (meV)				
n	f	D_{nf}	CE	CE-T	CE-P	direct	CE-R
0	1	1	0.64	0.18	0	-87238.23	0.4
1	1	1	-178.48	-176.58	-175.46	-659.08	-175.88
2	1	12	27.02	29.38	29.10	28.15	28.17
	2	6	0.2				
	3	24	0.3				
	4	12	0.47				
	5	24	0.34				
	6	8	-0.64				
	7	48	-0.11				
	8	6	0.36				
3	1	24	-0.48	0.04		-0.24	-0.31
	2	36	0.32				
	3	72	0.99				
4	1	8	3.45	-0.73		-1.87	
	2	48	-0.96				
	3	48	-0.86				
CV1 score			0.47	1.05	0.99		–
CV0 score			0.28	0.92	0.93		0.28
rms error						3.90 (2.08)	

completely on the Au-rich side, see Fig. 5.1. With larger longer-ranged pairs and multibody interactions the dominance of the NN pair is rapidly lost. Thus, the loss of degeneracy is important when comparing NN-only and dominant NN cases, as it changes the topology and coexistence regions of the phase diagrams.

5.3.2 The FCC Ising Model Revisited

The fcc Ising model with a clustering (ferromagnetic) NN pair interaction results in phase segregation, with the miscibility gap having a maximum at $c = 0.5$ at $k_B T_c/|\tilde{V}_{21}| = 2.42$. Multibody interactions in phase-segregating alloys make this miscibility gap asymmetric versus composition; a rapid estimate of their transition temperatures was discussed in [8].

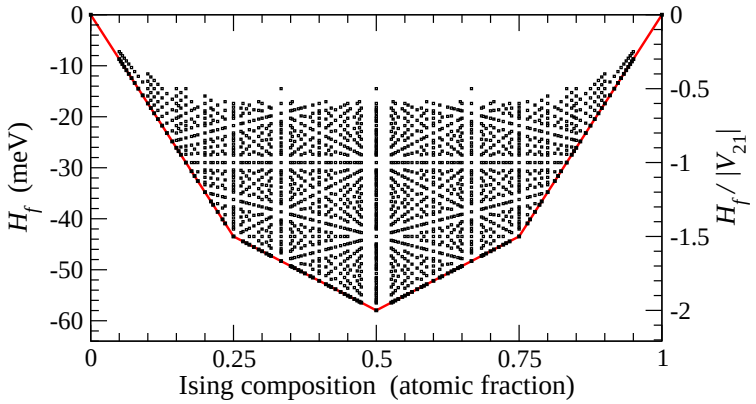

(a)

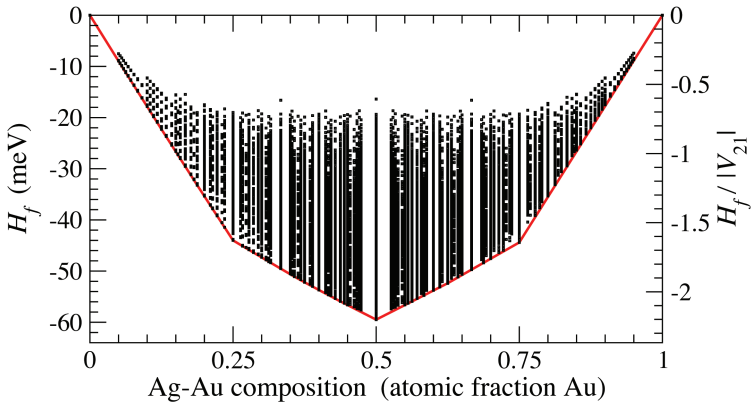

(b)

Figure 5.2: (color online) Structural formation enthalpies for cells up to 20 atoms: (a) fcc Ising model and (b) Ag-Au alloy from an optimal CE. Lines (red) are the groundstate hull, see text for number of degenerate structures on the hull.

Here we discuss the more interesting fcc ordering (antiferromagnetic) case [46,143–145,148, 154–156].

Structural formation enthalpies and groundstates of an Ising (NN-pair only) model for ordering on fcc lattice are shown in Fig. 5.2(a), and its phase diagram is shown in Fig. 5.3(a). Although frustration and degeneracy of the fcc Ising model is well-known [140–142,146,157–162], it is worth noting that, for example, $L1_2$, DO_{22}, DO_{23} structures at $c = 1/4$ or $3/4$ have degenerate energies with NN-only Ising interactions since their NN environment is the same. DO_{22} or DO_{23} can sometimes (but not always [6]) be viewed as $L1_2$ with APB(001), which have zero energy within the NN interaction range. This is

also true for $L1_0$ structure at $c = 1/2$, which is made up of layers of (001) planes with antiferromagnetic ordering, where the antiferromagnetic layers in $L1_2$ and $L1_0$ structures can be shuffled with respect to one another without incurring any energy cost. This allows us to estimate quickly the degeneracy in a $4L^3$-atom cell, where L^3 is the number of 4-atom fcc unit cell. Accounting for cubic symmetry, the degeneracies are 2^L and 2^{2L} for $c = 1/4$ (or 3/4) and $c = 1/2$, respectively [141, 146].

As noted above, combining the neighboring groundstates (e.g., $L1_0$ and $L1_2$, or $L1_2$ and pure elements) into larger structures with zero-energy APB yields chains of structures on the groundstate hull, see Fig. 5.2(a). Again, due to the numerous possible superlattice ("adaptive") structures that can be constructed from zero-energy APB configurations, there is a larger number of degenerate structures (or superdegeneracy [140–142, 145, 146]) as a result of a limited interaction range. Even small longer-range interactions are sufficient to remove degeneracies, giving an obvious difference between highly-degenerate Ising model and Ag-Au, see Fig. 5.2.

Depending on the range of interactions considered, it is possible to obtain 3,039,674 configurations with up to 20-atom unit cell [4]. In particular, for our optimal CE for the real Ag-Au involving 8 pairs, 3 triplets, and 3 quadruplets (Table 5.1), there are 1,927,602 structures that are distinguishable – with 6627 of them on the hull. In contrast, in Fig. 5.2(a) only 1843 structures with different energies and compositions are distinguished by the NN-pair Ising model – with 127 on the groundstate hull. Using $L = (20/4)^{1/3}$ one can estimate the degeneracies at $c = 1/4$ (3/4) and 1/2 to be 3 and 11, respectively, comparing well with our actual numbers of 5 and 11. This degeneracy is much smaller than that arising from superdegeneracy, which accounts for the other 6604 degenerate structures on the groundstate hull (with 2 elemental state removed). Longer-range interactions in alloys lead to non-zero APB energies and (eventually) remove this degeneracy, see, e.g., Fig. 5.2(b) for Ag-Au with widening of two-phase coexistence regions in the Au-rich end.

5.3.3 Phase Diagrams

Each distinguishable groundstate at $c = 1/4$, $1/2$, and $3/4$ in Fig. 5.2 corresponds to an ordered phase in the phase diagram in Fig. 5.3. At dilute concentrations a short-ranged repulsion between the solute atoms prevents them from being nearest neighbors; however, in the fcc Ising model all atomic arrangements (ordered or disordered) without NN interactions are equally energetically favored. Hence, it is not surprising that there are no finite-T phase boundaries near $c = 0$ or 1.

Typically, in phase diagrams with similar topologies, the low-T region at $1/4 < c < 1/2$ should be a phase-coexistence region. For the fcc Ising model this region is that of $L1_2$ + $L1_0$ coexistence, see Fig. 5.3, and is much narrower (due to superdegeneracy) than would be found for the case of less dominant NN pair interaction. Existence of zero- or low-energy APB leads to a large statistical ensemble that makes determining ordered phase boundaries at very low T difficult. Indeed, this had led to controversies in previous works on fcc Ising model, such as existence of the L' phase in CVM calculations [163] and the location of triple points in MC calculations. [141, 142, 145]

To identify phase transitions within MC simulations, c_V vs. T and μ vs. c are examined at fixed c and fixed T, respectively. At low-T, $\mu(T)$ vs. c plot are used in conjunction with c_V vs. T to determine coexistence regions. For the Ising model, our values of $k_B T_c/|\tilde{V}_{21}|$ at $c = 0.25$ (or 0.75) and 0.5 are 0.45 and 0.43, respectively, in good agreement with reported values [141, 142, 145] of 0.46 and 0.43. (Note that the critical temperature for ordering is a factor of 5 times smaller than segregation. And, just as with ours, published Ising phase diagrams typically do not report temperatures below $k_B T/|\tilde{V}_{21}| < 0.1$ due to slow equilibration. Due to slow kinetics, experiments do not access these temperature anyway.) In addition, we find a triple point at $k_B T/|\tilde{V}_{21}|$=0.23 at c=0.39 (or 0.61), see Fig. 5.3, in agreement with MC simulation using grand canonical [142] (c=0.39, $k_B T/|\tilde{V}_{21}|$=0.25) or careful large-cells [146] (c=0.39, $k_B T/|\tilde{V}_{21}|$=0.245). Importantly, only the states occurring at the vertices of the groundstate hull ($c = 1/4, 1/2, 3/4$) have corresponding high-T phases, i.e., no LPS (or adaptive structures) that are linear combinations of those groundstates.

Along with the calculated high-T boundaries (solid lines and symbols in Fig. 5.3), we find

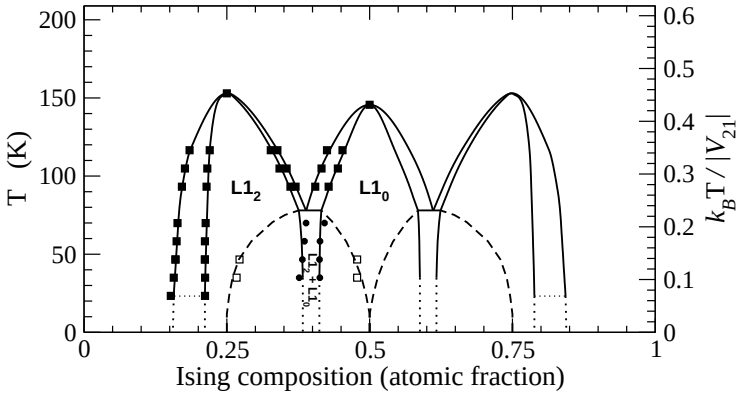

(a)

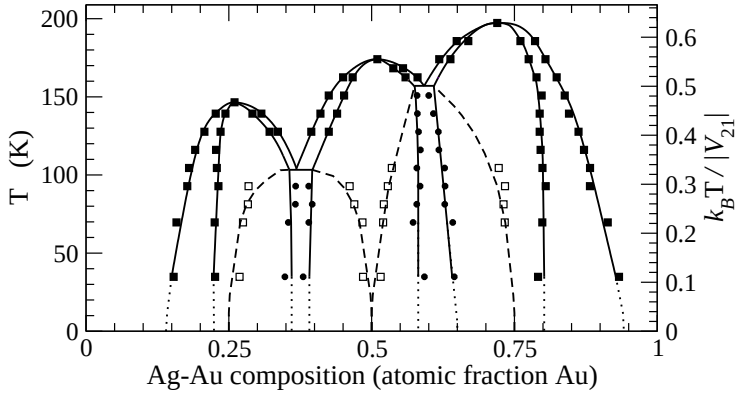

(b)

Figure 5.3: T vs. c diagram of fcc (a) Ising model and (b) Ag-Au from the optimal CE. Solid squares are determined from sharp peaks in heat capacity, with solid lines denoting boundaries. Narrow $L1_2$ + $L1_0$ coexistence regions are below tricritical points. Other heat capacity maxima give boundaries (open squares and dashed lines) that are the stable coexistence boundaries when superdegeneracy is lifted amongst the LPS. Dotted lines are extensions of boundaries to 0 K.

Table 5.2: Order-disorder temperatures at stoichiometric compositions for different sets of interactions fitted to Ag-Au.

	T_c (K)		
c	CE	CE-T	Ising
0.25	144	155	152
0.50	173	149	145
0.75	193	148	152

a narrowing of the $L1_2$ + $L1_0$ coexistence due to superdegeneracy (just below the triple points), as identified earlier [140–146]. For cases where the transitions are weak and/or temperatures are low, features could not always be clearly identified from heat capacity alone; hence, we examined $\mu(T)$ vs. c plots for discontinuities in the gradient. In addition, we find other maxima in the heat capacity (identified by the open squares and dashed lines) that become the stable coexistence boundaries when superdegeneracy is lifted amongst the LPS arising from stronger, longer-ranged pairs and/or larger multibody interactions.

For NN-pairs only, the phase diagram is symmetric versus composition. The multibody interactions in Ag-Au result in asymmetry in the topology of the phase diagram, see Fig. 5.3, and the corresponding transition temperatures, see Table 5.2. Besides this asymmetry, phase diagrams of fcc alloys with dominant NN interactions have similar topology to that of an Ising model, as is evident in Fig. 5.3. The removal of degeneracy leads to new states and raises the transition temperatures from 0 K to a low, but finite value. At low temperatures ($k_BT/|\tilde{V}_{21}| < 0.1$), transition boundaries are difficult to determine among degenerate (or nearly degenerate) LPS so they are sometimes reported as boundaries that resemble "elephant's feet" [31]. Due to vanishing kinetics at such low temperatures we do not expect those phase transitions to be observed experimentally. Importantly, low-energy structures competing with the ground states influence ordering and atomic structure of materials, affecting their properties. As the multibodies become more significant relative to the NN pair, the degeneracies are lost and the diagram no longer has the narrow $L1_2$ + $L1_0$ coexistence region, which actually resembles the dashed lines shown in Fig. 5.3. Indeed, multibodies can screen pair interactions, decreasing them by over 70% [153].

For completeness, we note that, in general, the vibrational entropy contributions to an

order-disorder temperatures can be significant. Vibrational effects add a higher level of complexity and computational difficulty, more than the CE. It can be shown (e.g., see [12] or [54]) that T_c is altered by changes in harmonic vibrational entropy $\Delta S_{vibr}^{\alpha\to\beta}$ from the $\alpha-\beta$ transition from solely configurational contributions $T_{c,conf}^{\alpha\to\beta}$ as

$$T_c^{\alpha\to\beta} \approx T_{c,conf}^{\alpha\to\beta}\left(1+\frac{\Delta S_{vibr}^{\alpha\to\beta}}{\Delta S_{conf}^{\alpha\to\beta}}\right)^{-1}. \tag{5.3}$$

As discussed in section 4.3.4, the importance of $\Delta S_{vibr}^{\alpha\to\beta}$ can be accurately estimated from only differences in electronegativities of solute and host. For Pd-Rh, for example, the electronegativity difference ($|0.08|$) is very small and vibrations can be ignored in determining the miscibility gap, whereas, for other systems, this estimate brings the CE T_c in agreement with experiment [8]. For Ag-Au, the electronegativies are 1.93 for Ag and 2.4 for Au, hence, not negligible. We estimate a 13% decrease (18% increase) in T_c (Table 5.2) at Ag_3Au (at $AgAu_3$), which increase slightly the phase diagram asymmetry. The effect of vibrations should be considered for each case, but does not affect our findings generally.

5.3.4 Electronic Origins of Interactions

And now to the most significant point of the chapter. As described in section 5.2.1, using supercell techniques the local dominant NN multibody interactions can be extracted. (In principle, a transferable set of interactions, applicable to any structural configuration, can be calculated this way [153], but the cost of computation increases exponentially with the size of the multibody cluster.) We calculated the DFT energies of pure fcc Ag $E_{(0)}$ and Au monomer $E_{(1)}$, dimer $E_{(2)}$, trimer $E_{(3)}$ and tetramer $E_{(4)}$ embedded in Ag. With these energies the NN n-body interactions $\tilde{V}_{n1}$ from Eq. (5.2) can be ascertained directly for the dilute-Au case (i.e., $1-4$ Au sites out of 32). The results of the direct calculations of interactions are listed in Table 5.1. They are in reasonable agreement with the data from an optimal CE. However, as expected, they are in even better agreement (see Table 5.1) with a CE restricted to the NN tetrahedron (CE-T) with all its subclusters. Both the direct and CE-T, Table 5.1 shows that the dominant interaction is the NN pair, and that NN

four-body is larger than NN three-body interaction.

We should expect a difference between interactions found from the CE using data from concentrated alloys and those found directly from the supercell with dilute concentrations of Au in Ag. In particular, the 4-body tetrahedron could be less significant in the concentrated alloys as it favors segregation. So, we performed a CE fit (CE-R in Table 5.1) using the restriction to NN pair and triplet interactions in the range of $0 \leq c \leq 1/4$; these CE-R interactions are in excellent agreement with those determined directly. (The CE requires that enough structures have been calculated using DFT that contain the relevant clusters, such as 3-body, in order to extract a value without infinite CV scores; hence the restriction to only NN pairs and triplets here.)

Finally, we used these direct interactions in Table 5.1 to predict the 55 structural enthalpies calculated within DFT; these and their *rms* error with the DFT enthalpies are given in Table 5.1, along with *rms* error for the 19 out of 55 in the range of $0 \leq c \leq 1/4$ (shown in parenthesis). Evidently, the direct interaction "predict" the structural enthalpies much better in the restricted range (rms of $\pm 2m$eV) where they were fit, as they much better reflect the physics in that range, than they do for all 55 structures (rms of $\pm 4m$eV – or about 46 K).

It is important to point out that "inverse" methods like the cluster expansion [2, 5, 9–11, 31, 164–166] and "direct" methods, like the supercells or coherent potential approximation based approaches like concentration functionals [167] or the generalized perturbation method, [31, 168–170] have been compared many times before (e.g., [171] or [172]). Direct methods are directly connected to the electronic effects and have direct physical interpretation (effective interactions are related to moments of the density of states or convolutions of the electronic structure), whereas inverse CE methods, while often argued as unique, can loose the physical correctness if the basis sets are not chosen correctly, [6] including having non-unique interactions sets and no direct physical interpretation [59].

From supercells the electronic density differences can be calculated similarly to the energy differences in Eq. 5.2, and the NN interactions can be visualized, see Fig. 5.4[1], with

[1]The author thank Dr. Lin-Lin Wang for the use of this diagram.

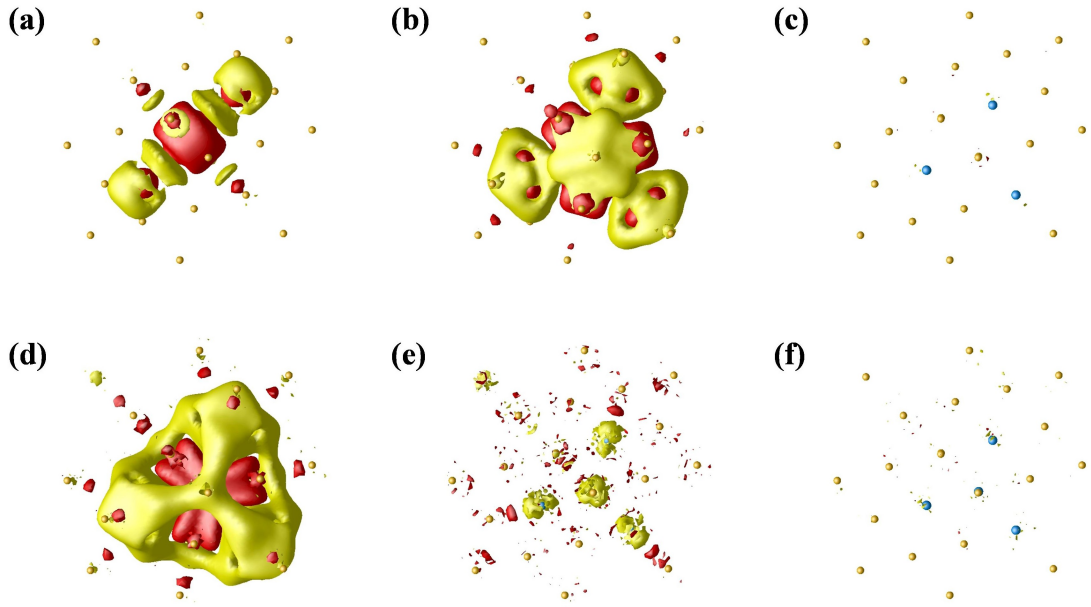

Figure 5.4: (color online) Electron density differences associated with the NN interactions for Au solutes (blue spheres) in fcc Ag (yellow spheres), viewed along [111]. Iso-surfaces are plotted at ± 0.0003 e/Å^3, with red (yellow) standing for density depletion (accumulation). The electron density differences in (a), (c) and (f) correspond to the NN interactions $\tilde{V}_{21}$, $\tilde{V}_{31}$, and $\tilde{V}_{41}$, repsectively, in Eq. 5.2. Differences (b), (d) and (e), defined in Eq. 5.4, show contributions of the subclusters [courtesy of Dr. Lin-Lin Wang].

panels (a), (c) and (f) corresponding to interaction $\tilde{V}_{21}$, $\tilde{V}_{31}$ and $\tilde{V}_{41}$, respectively. We also visualize electronic density differences corresponding to

$$\begin{aligned} \Delta E_3^{(1)} &= \tilde{V}_{31} + 3\tilde{V}_{21} = E_{(3)} - 3E_{(1)} + 2E_{(0)} \\ \Delta E_4^{(1)} &= \tilde{V}_{41} + 4\tilde{V}_{31} + 6\tilde{V}_{21} = E_{(4)} - 4E_{(1)} + 3E_{(0)} \\ \Delta E_4^{(2)} &= \tilde{V}_{41} + 4\tilde{V}_{31} = E_{(4)} - 6E_{(2)} + 8E_{(1)} - 3E_{(0)} \quad . \end{aligned} \tag{5.4}$$

As shown in Fig. 5.4, for a NN Au dimer, the bonding is achieved by accumulating electron density around Au atoms and at the same time depleting it in the middle (compared to those originally associated with a monomer, i.e. a single Au impurity embedded in Ag). The same feature is evident in (b) and (d), by only subtracting contributions of Au monomers for Au trimer and tetramer, respectively. By subtracting contributions of both Au monomers and dimers from Au trimer, we get the electron redistribution associated with

the direct 3-body NN interaction, which is very small as shown in (c); it is even smaller than the direct 4-body NN interaction shown in (f). In (e), for Au tetramer, the electron density difference corresponding to the multibody interactions beyond NN pair has the pattern of accumulating density on each Au atom and also in the interstitial tetrahedral site. Isosurfaces taken at ± 0.0001 e/$\mathring{A}^{\,3}$ (not shown) have been checked to identify that this pattern is indeed mostly due to the 3-body interaction, in accord with Eq. 5.4. The electron density redistribution is a direct way to illustrate the relative strength of multibody NN interactions and give the same trends observed in the data listed in Table 5.1 by both CE and direct calculations. This visualization highlights the physical origin of the cluster interactions within alloys, which are described accurately by a CE with complete and compact basis [6].

5.4 Summary

We considered enthalpic (structural formation enthalpy versus composition c) and thermodynamic properties (T_c vs c phase diagrams) of the fcc Ising model and close-packed alloys with dominant nearest-neighbor (NN) pair interactions, exemplified by fcc Ag-Au, although this is but one example of such alloys [51,55,150–152]. We discussed degeneracy, showcased how frustration and limited interaction range introduce zero-energy antiphase boundaries (APB), and explained that low-energy APB lead to formation of the chains of long-period superstructures (LPS) on the groundstate hull and the elimination of degeneracies in a composition-dependent manner. We described how longer-ranged pairs or larger multibodies interactions change the phase diagram and the phase-coexistence regions, widening as the dominance of the NN pair interactions is lost. Low-energy APB and LPS chains are expected to be a generic feature of the close-packed fcc alloys with dominant NN interactions. Finally, we found the interactions directly by a supercell method, confirming the dominance of the NN pair in Ag-Au, as predicted by a CE with a complete and compact basis, and showed when and how well the direct and CE interactions agree. We then visualized the electronic origins of direct chemical interactions in Ag-Au, highlighting the physical origin of the effective chemical interactions derived from direct and cluster expansion methods.

CHAPTER 6

UNIQUE CLUSTER EXPANSION VIA THE SUBSPACE PROJECTION METHOD

As pointed out in Chapter 3, although the cluster expansion (CE) is an exact basis set expansion [2] in terms of cluster correlation functions, whose coefficients (*a priori* unknown) are effective cluster interactions (ECI), it is impossible to determine all P^N ECI for a P-component alloy on a N-site lattice (where N is large). Using the DFT energies of a subset of M structures, which forms a subspace of the full P^N-dimensional configurational space, one then constructs a truncated CE set via structural inversion (SI) (see Section 2.2.1), evaluating at most M ECI. Current techniques often use some measure of predictive capability (e.g., cross-validation (CV) error, see Section 3.3.4) to select an optimally truncated CE set, resulting in a huge search space, thus leading to several non-unique sets with similar predictive capability (see Section 3.1).

6.1 Introduction

The goal is thus to have a reliable method to construct a truncated set, whose ECI approach that of the unique non-truncated CE, which is achieved only if all significant ECI are included. To obtain a uniquely truncated CE, we first show, using concepts from fractional factorial design [61, 62, 173, 174], how the judicious choice of M structural energies (for SI) allows the linear dependencies between cluster functions to be clearly identified. Because the ECI of two linearly dependent cluster functions are not individually determinable, one is kept in the truncated CE set while the other one is assumed to be zero. However, if this is not true, i.e., the neglected ECI is actually significant, the evaluated ECI will be biased, thus severely impacting the reliability of the truncated CE set. We will show that it is advantageous to consider a large supercell as our 'complete' Hilbert space, from which,

configuration subspaces and their associated linear dependencies (between ECI) can be clearly identified. Based on a cluster hierarchy [6], any critical dependency associated with a particular subspace of known energies can be removed by systematically adding structural energies from the 'complete' space. When the known subspace is large enough, the ECI of the truncated CE set (evaluated via SI) are no longer biased and approach the ECI of the unique untruncated CE. This method of subspace projection also results in a minimal set of known energies used for constructing the truncated CE.

In this chapter, we first set up the CE formalism focusing on the binary alloy system, and show its relation to other areas of studies, such as fractional factorial design, where the issues faced are similar to those of CE and the resolutions are transferable. These concepts are then illustrated using a simple example and via application to a real alloy system, FCC Ag-Au.

6.2 Cluster Expansion using Spin Variables

The cluster expansion (CE) is a basis expansion of alloy properties in terms of cluster entities, giving a formal and exact representation [2] when all clusters are included, and in its most general form (see (2.5)) is applicable to any multi-component alloy on a given lattice. This paper focuses on the binary alloy and uses orthogonal cluster functions constructed from spin variables (see Section 2.2). It is emphasized that the concepts are straightforwardly extendable to multi-component alloys.

Labeling the sites on an N-site lattice with integers $\{1, 2, ..., \mathrm{N}\}$, the vector $\vec{\sigma} = \{\sigma_1, \sigma_2, ..., \sigma_\mathrm{N}\}$ is used to describe a given structure (or configuration), where in an A-B alloy, $\sigma_i = 1(-1)$ if site i is occupied by atom of type A(B). The energy of an alloy structure expanded in terms of clusters is expressed as

$$\mathrm{E}(\vec{\sigma}) = \sum_{\eta} J_\eta \Phi_\eta(\vec{\sigma}) \quad , \tag{6.1}$$

where $\eta = \{i_1, i_2, ..., i_n\}$, a set of integers that denotes the sites selected to form an n-site cluster, with $i_k \in \{1, 2, ..., \mathrm{N}\}$ and $n \leq \mathrm{N}$. The summation is over all 2^N clusters possible

within the N-site lattice, including $\eta_0 = \{\emptyset\}$, which gives a constant term, J_0, independent of $\vec{\sigma}$. The J_η are the coefficients of the CE and are called the effective cluster interactions (ECI). The cluster functions, Φ, constructed from Chebyshev polynomials [2], are defined as

$$\Phi_\eta(\vec{\sigma}) \equiv \sigma_{i_1}\sigma_{i_2}...\sigma_{i_n}, \quad \forall i_k \in \eta \tag{6.2}$$

with $\Phi_0 = 1$, forming an orthogonal basis set which spans the 2^N configuration space. For example, $\Phi_{\{i\}}(\vec{\sigma}) \equiv \sigma_i$ is the single-site cluster at site i and $\Phi_{\{i,j\}}(\vec{\sigma}) \equiv \sigma_i\sigma_j$ is the pair cluster constructed using sites i and j, for a given configuration $\vec{\sigma}$. Note that, except for Φ_0, $\Phi_\eta(\vec{\sigma})$=1 or -1. The orthogonality condition is given by

$$\frac{1}{2^N}\vec{\Phi}_\eta \cdot \vec{\Phi}_{\eta'} \equiv \frac{1}{2^N}\mathrm{Tr}^{(N)}\Phi_\eta(\vec{\sigma})\Phi_{\eta'}(\vec{\sigma}) = \delta_{\eta\eta'} \quad , \tag{6.3}$$

where the trace is over all 2^N configurations, i.e., $\mathrm{Tr}^{(N)} \equiv \sum_{\sigma_1} ... \sum_{\sigma_N}$ and the correlation function is written as a 2^N-component vector, $\vec{\Phi}_\eta$, whose rows are indexed by $\vec{\sigma}$. The set of $\{\vec{\Phi}_\eta\}$ thus forms an orthogonal array and Eq. 6.1 can be expressed as

$$\vec{E} = \left[\vec{\Phi}_1, \vec{\Phi}_2, ..., \vec{\Phi}_{2^N}\right] \vec{J} \equiv \mathbf{\Phi}\vec{J} \quad , \tag{6.4}$$

where each cluster set η is simply labelled by integers 1 to 2^N.

As discussed in Chapter 3, $E(\vec{\sigma})$ of various structures in Eq. (6.1) are obtained via density function theory (DFT) calculations (or by any other first-principles method). When all 2^N $E^{DFT}(\vec{\sigma})$ are evaluated, the ECI are simply obtained from Eq. (6.4) via a matrix inversion

$$\vec{J} = \mathbf{\Phi}^{-1}\vec{E} \quad . \tag{6.5}$$

However, first-principle calculations are generally computationally expensive. It is impossible to evaluate all $E^{DFT}(\vec{\sigma})$ for even a modest value of N (N=32 gives $\sim$ 4 billion configurations), and in practice only a small fraction (typically between 30 to 100) are evaluated and

used to construct a CE for a given alloy system, and through structural inversion (SI), only a subset of ECI is determinable. Thus two important choices has to be made; which subset of $\mathrm{E}^{\mathrm{DFT}}$ to use for structural inversion (SI) and which subset of ECI are to be determined.

6.2.1 Error Analysis of Structural Inversion

As done in (2.7), it is pertinent to divide $\vec{J}$ into two subvectors $\vec{J}_1$ and $\vec{J}_2$ of length M and 2^{N}-M respectively, with $\vec{J}_1$ being the *chosen* set of ECI to be determined via structural inversion (SI) while leaving $\vec{J}_2$ undetermined. From Eq. (6.4),

$$\left[\begin{array}{c} \vec{\mathrm{E}}_1 \\ \hline \vec{\mathrm{E}}_2 \end{array}\right] = \left[\begin{array}{c|c} \boldsymbol{\phi}_{11} & \boldsymbol{\phi}_{12} \\ \hline \boldsymbol{\phi}_{21} & \boldsymbol{\phi}_{22} \end{array}\right] \left[\begin{array}{c} \vec{J}_1 \\ \hline \vec{J}_2 \end{array}\right] \quad , \tag{6.6}$$

where $\boldsymbol{\phi}_{11}$ is a L-by-M matrix with $2^{\mathrm{N}} \geq L \geq M$ and $\vec{\mathrm{E}}_1$ provides us with L DFT structure energies to solve for $\vec{J}_1$. We assume in our anlaysis that the DFT energies are very well converged with negligible errors. Structural inversion is applied using the general least squares method,

$$\hat{\vec{J}}_1 = \left(\boldsymbol{\phi}_{11}^{\mathrm{T}} \boldsymbol{\phi}_{11}\right)^{-1} \boldsymbol{\phi}_{11}^{\mathrm{T}} \vec{\mathrm{E}}_1 \quad , \tag{6.7}$$

provided that $\boldsymbol{\phi}_{11}^{\mathrm{T}} \boldsymbol{\phi}_{11}$ is invertible and $\hat{\vec{J}}_1$ is an estimator of $\vec{J}_1$. The choice of $\vec{\mathrm{E}}_1$ already precludes certain combinations of $\vec{J}_1$, which would result in a singular $\boldsymbol{\phi}_{11}^{\mathrm{T}} \boldsymbol{\phi}_{11}$ whose columns are linearly dependent. We further note that under the least square method, the estimator for $\vec{J}_2$ is always zero,

$$\hat{\vec{J}}_2 = \vec{0} \quad . \tag{6.8}$$

Unless $\vec{J}_2$ is truly zero, in general, $\hat{\vec{J}}_1$ is a biased estimator,

$$\begin{aligned} \hat{\vec{J}}_1 &= \vec{J}_1 + \left(\boldsymbol{\phi}_{11}^{\mathrm{T}} \boldsymbol{\phi}_{11}\right)^{-1} \left(\boldsymbol{\phi}_{11}^{\mathrm{T}} \boldsymbol{\phi}_{12}\right) \vec{J}_2 \\ &= \vec{J}_1 + \delta \vec{J}_1 \quad , \end{aligned} \tag{6.9}$$

which is derived by substituting the relation, $\vec{\mathrm{E}}_1 = \boldsymbol{\phi}_{11}\vec{J}_1 + \boldsymbol{\phi}_{12}\vec{J}_2$ from (6.6), into (6.7). The estimator of the known structural energies, $\vec{\mathrm{E}}_1$, is then given as,

$$\begin{aligned}
\hat{\vec{\mathrm{E}}}_1 &= \boldsymbol{\phi}_{11}\hat{\vec{J}}_1 \\
&= \vec{\mathrm{E}}_1 + \left[\boldsymbol{\phi}_{11}\left(\boldsymbol{\phi}_{11}^{\mathrm{T}}\boldsymbol{\phi}_{11}\right)^{-1}\left(\boldsymbol{\phi}_{11}^{\mathrm{T}}\boldsymbol{\phi}_{12}\right) - \boldsymbol{\phi}_{12}\right]\vec{J}_2 \\
&= \vec{\mathrm{E}}_1 + \delta\vec{\mathrm{E}}_1 \quad , \qquad (6.10)
\end{aligned}$$

where $|\delta\vec{\mathrm{E}}_1|^2/\mathrm{L}$ is commonly known as the least square error. Likewise, we have for the structural energies not used in the SI,

$$\begin{aligned}
\hat{\vec{\mathrm{E}}}_2 &= \boldsymbol{\phi}_{21}\hat{\vec{J}}_1 \\
&= \vec{\mathrm{E}}_2 + \left[\boldsymbol{\phi}_{21}\left(\boldsymbol{\phi}_{11}^{\mathrm{T}}\boldsymbol{\phi}_{11}\right)^{-1}\left(\boldsymbol{\phi}_{11}^{\mathrm{T}}\boldsymbol{\phi}_{12}\right) - \boldsymbol{\phi}_{22}\right]\vec{J}_2 \\
&= \vec{\mathrm{E}}_2 + \delta\vec{\mathrm{E}}_2 \quad , \qquad (6.11)
\end{aligned}$$

where $\delta\vec{\mathrm{E}}_2$ is called the validation or predictive error, because the structural energies in $\vec{\mathrm{E}}_2$ can be calculated via DFT a posteriori to validate $\hat{\vec{J}}_1$. Now, in least square fitting, $\vec{J}_1$ is chosen to minimize $|\delta\vec{\mathrm{E}}_1|^2/\mathrm{L}$, which is zero when $\boldsymbol{\phi}_{11}$ has a full rank of L. Errors in $\vec{\mathrm{E}}_2$ however remains,

$$\delta\vec{\mathrm{E}}_2 = \left[\boldsymbol{\phi}_{21}\boldsymbol{\phi}_{11}^{-1}\boldsymbol{\phi}_{12} - \boldsymbol{\phi}_{22}\right]\vec{J}_2 \quad , \qquad (6.12)$$

unless $\vec{J}_2$ is negligible. Overfitting occurs when $\delta\vec{\mathrm{E}}_1 = 0$ but $\delta\vec{\mathrm{E}}_2$ remains large, due to significant elements in $\vec{J}_2$. To balance $\delta\vec{\mathrm{E}}_1$ and $\delta\vec{\mathrm{E}}_2$, current methods are focused on choosing truncated CE sets that give a minimal value for selected elements (structures) in $\delta\vec{\mathrm{E}}_2$, e.g., in the leave-one-out cross-validation (CV_1) method (see Section 3.3.4). However, as mentioned earlier, without a physical hierarchy enforced upon the clusters, the search space is large, and often results in non-unique truncated CE sets.

In this chapter, we instead investigate linear dependencies between cluster functions, which directly dictates the error in the estimator, $\delta\vec{J}_1$, in Eq. (6.9). We elucidate a particular choice of structural energy subsets, which leads to $\boldsymbol{\phi}_{11}$ being a Hadamard matrix,

simplifying the error analysis in Eqs. (6.9), (6.10) and (6.11). Hadamard matrices are used in the area of fractional factorial design of experiments [61, 62, 173, 174], where effects with discrete levels used to describe experiment data set are obtained via knowing only a fraction of the all possible experimental data, and the various assumptions and problem resolutions are directly applicable to the selection of a unique truncated CE.

6.3 Relation to Hadamard Matrices

When $\{\vec{\Phi}_\eta\}$ in Eq. (6.4) are arranged in a *certain* lexicographical order, $\mathbf{\Phi}$ becomes the Hadamard matrix, commonplace in factorial design [61] of experiments and signal processing [175]. Several classes of Hadamard matrices exist, of which the Sylvester-type [62] of size 2^{N}-by-2^{N} are of direct relevance to CE. Starting from a single lattice site labelled as 1,

$$\mathcal{H}_{\{1\}} = \begin{bmatrix} 1 & 1 \\ 1 & -1 \end{bmatrix} = \left[\vec{\Phi}_0, \vec{\Phi}_{\{1\}}\right] \quad , \tag{6.13}$$

with the 2-configuation space fully spanned by the 2-component vectors $\vec{\Phi}_0$ and $\vec{\Phi}_{\{1\}}$. When a second site (labelled 2) is added,

$$\begin{aligned} \mathcal{H}_{\{1,2\}} = \mathcal{H}_{\{1\}} \otimes \mathcal{H}_{\{2\}} &\equiv \begin{bmatrix} \mathcal{H}_{\{2\}} & \mathcal{H}_{\{2\}} \\ \mathcal{H}_{\{2\}} & -\mathcal{H}_{\{2\}} \end{bmatrix} \\ &= \begin{bmatrix} 1 & 1 & 1 & 1 \\ 1 & -1 & 1 & -1 \\ 1 & 1 & -1 & -1 \\ 1 & -1 & -1 & 1 \end{bmatrix} \\ &= \left[\vec{\Phi}_0, \vec{\Phi}_{\{1\}}, \vec{\Phi}_{\{2\}}, \vec{\Phi}_{\{1,2\}}\right] \quad , \end{aligned} \tag{6.14}$$

where all four configurations are enumerated by $[\vec{\Phi}_{\{1\}}, \vec{\Phi}_{\{2\}}]$, e.g., the second row corresponds to a structure with sites 1 and 2 occupied by atoms of type -1 and 1 respectively.

For a general N-site lattice the Hadamard matrix is then

$$\mathcal{H}_{\{1,...,\mathrm{N}\}} = \mathcal{H}_{\{1\}} \otimes \mathcal{H}_{\{2\}} \otimes ... \otimes \mathcal{H}_{\{\mathrm{N}\}} \quad , \tag{6.15}$$

which satisfies the property,

$$\mathcal{H}^{\mathrm{T}}_{\{1,...,\mathrm{N}\}} \mathcal{H}_{\{1,...,\mathrm{N}\}} = 2^{\mathrm{N}} \mathrm{I}_{2^{\mathrm{N}}} \quad , \tag{6.16}$$

where $\mathrm{I}_{2^{\mathrm{N}}}$ is the 2^{N}-by-2^{N} identity matrix. In addition, the columns and rows are the Walsh functions, commonly used in spectral analysis of rectangular waveforms [175], thus when $\mathbf{\Phi} = \mathcal{H}_{\{1,...,\mathrm{N}\}}$, Eq. (6.4) and (6.5) are the Hadamard-Walsh transformation and its inverse, with the ECI being Walsh coefficients.

6.4 Fractional Factorial Design

In the language of factorial design, $\vec{\mathrm{E}}$ (see Eq. (6.4) and (6.5)) is the full experimental *data set* to be explained by N 2-level *factors* (represented by the N single-site clusters) with each factor having 2 possible values, 1 or -1. Because factors corresponds to spin variables, multiplications of factors results in *interactions*, which corresponds to the pair and multibody cluster functions defined in (6.2). Each experimental data is described by a *combination* of *levels*, corresponding to $\vec{\sigma}$ being used to notate the atomic occupation in a given configuration. The full factorial design space is then spanned by the columns of the Hadamard matrix $\mathcal{H}_{\{1,...,\mathrm{N}\}}$. Using N=2 case for illustration, from Eq. (6.14), the full factorial design is given by

$$[E_{11}, E_{\bar{1}1}, E_{1\bar{1}}, E_{\bar{1}\bar{1}}]^{\mathrm{T}} = \mathcal{H}_{\{1,2\}} \, [J_0, J_1, J_2, J_{1,2}]^{\mathrm{T}} \quad , \tag{6.17}$$

where the subscripts of $\vec{\mathrm{E}}$ denote the combination of $\vec{\sigma}$ as given by $[\vec{\Phi}_{\{1\}}, \vec{\Phi}_{\{2\}}]$ (see Eq. (6.14)) while those of $\vec{J}$ are labels of the cluster sites. The coefficients $\vec{J}$, called *effects*, obtained via inversion of $\mathcal{H}_{\{1,2\}}$, have specific physical meanings. For example, the *effect* $J_1 = (1/4)(E_{11} - E_{\bar{1}1} + E_{1\bar{1}} - E_{\bar{1}\bar{1}})$ gives the *contrast* of factor 1 (or site 1) averaged over

all possible levels of factor 2, because $E_{11} - E_{\bar{1}1}$ and $E_{1\bar{1}} - E_{\bar{1}\bar{1}}$ measure the effect of the changing the levels in factor 1, with factor 2 fixed at levels 1 and -1 respectively.

As pointed out in Section 6.2, only a fraction of 2^{N} possible experiments are done in practice, either because the experiments are costly or the total number required is prohibitively large. In fractional factor design, the *sparsity of effects* principle [173, 176] (or Pareto's principle) is often assumed, i.e., all experiment data can be explained by small or manageable number of effects. In 2-level fractional factorial design, it is common to select in fractions of $1/2^k$, so that the reduced design matrix $\boldsymbol{\phi}_{11}$ (see Eq. (6.6)) remains a Hadamard matrix, an approach that is useful for determining how the *effects* in $\vec{J}$ are *confounded*; i.e., how the interactions in $\vec{J}$ are correlated with one another. Two effects are confounded if it is impossible to evaluate them simultaneously from the known data set. The confounding relations are succinctly expressed in terms of k *generators*. Using N=2 as our example, suppose only the first two experiments, E_{11} and $E_{\bar{1}1}$, are evaluated (half of the four possible experiments), this set forms a combinatoric subspace where all possibilities of factor 1 are included with factor 2 held fixed (at a value of 1). We have the following scenario,

$$[E_{11}, E_{\bar{1}1}]^{\mathrm{T}} = \begin{bmatrix} 1 & 1 & 1 & 1 \\ 1 & -1 & 1 & -1 \end{bmatrix} [J_0, J_1, J_2, J_{1,2}]^{\mathrm{T}} \quad , \tag{6.18}$$

which is an under-determined set of linear equations, hence it is impossible to solve for all effects; at best only 2 of the 4 can be determined. Because columns 1 and 3 are identical, J_0 and J_2 are confounded, likewise for J_1 and $J_{1,2}$. We now choose two effects to be determined and include them in $\vec{J}_1$ (see Eq. (6.6)). Because of the confounding relations, we avoid pairing J_0 and J_2 or J_1 and $J_{1,2}$, which would render $\boldsymbol{\phi}_{11}$ singular.

Now, suppose we choose to evaluate J_0 and J_1, comparing (6.6) with (6.17), we have,

$$\vec{\mathrm{E}}_1 = [E_{11}, E_{\bar{1}1}]^{\mathrm{T}} \quad ; \quad \vec{\mathrm{E}}_2 = [E_{1\bar{1}}, E_{\bar{1}\bar{1}}]^{\mathrm{T}} \quad , \tag{6.19}$$

$$\vec{J}_1 = [J_0, J_1]^{\mathrm{T}} \quad ; \quad \vec{J}_2 = [J_2, J_{1,2}]^{\mathrm{T}} \quad , \tag{6.20}$$

$$\boldsymbol{\phi}_{11} = \boldsymbol{\phi}_{12} = \boldsymbol{\phi}_{21} = -\boldsymbol{\phi}_{22} = \mathcal{H}_{\{1\}} \quad , \tag{6.21}$$

where the last relation is a result of the Hadamard matrix structure (see (6.14)). Using the property of Hadamard matrices in (6.16), the error analysis in Eqs. (6.9), (6.10) and (6.11) are respectively simplified to:

$$\hat{\vec{J}}_1 = \vec{J}_1 + \vec{J}_2 \quad , \tag{6.22}$$

$$\delta\vec{\mathrm{E}}_1 = 0 \quad , \tag{6.23}$$

$$\delta\vec{\mathrm{E}}_2 = 2\mathcal{H}_{\{1\}}\vec{J}_2 \quad . \tag{6.24}$$

From (6.22), the elements in the estimator, $\hat{\vec{J}}_1$, are $J_0 + J_2$ and $J_1 + J_{1,2}$, and this is clearly a bias estimate of $\vec{J}_1$. Unless one knows apriori that $J_0 = J_{1,2} = 0$, we incur some errors in the estimation of $\vec{\mathrm{E}}_2$, even though $\vec{\mathrm{E}}_1$ is reproduced exactly, which shouldn't be surprising, because the values of $\vec{\mathrm{E}}_1$ are known *a priori* and we can make as good an effort as can be to reproduce them.

The crux of the issue is, thus, one effect from each of the two groups, $J_0 + J_2$ and $J_1 + J_{1,2}$, has to be assumed negligible or zero, as a result of only knowing a fraction of the data in $\vec{\mathrm{E}}$. In fractional factorial design, this choice is in general made using the *hierarchical ordering* principle [173, 177], i.e., higher-order effects are smaller in magnitude and hence less important than lower-order ones. Accordingly, one would chose J_0 over J_2 and J_1 over $J_{1,2}$, because we have a good chance that $|J_0| > |J_2|$ and $|J_1| > |J_{1,2}|$. For completion, we state the last principle, *effect heredity* [173, 178] principle, which states that if a higher-order effect is important, then at least one of its parent effect is important. Thus, if we had evaluated J_0 and $J_{1,2}$ instead (thus neglecting J_1 and J_2 which are parent effects of $J_{1,2}$), the heredity principle is violated.

The issues faced in fractional factorial design are applicable to CE. As pointed out in Section 6.2.1, one only evaluates the DFT energies of a fraction of all 2^{N} configurations, hence the ECI are confounded. To minimize the risk of evaluating the less significant ECI, which are associated with clusters of higher order and larger spatial extent, at the expense of more significant ones, a physical hierarchy is used to rank the clusters [6], and the truncated CE basis is enforced to be compact and locally complete (analogous to effect

heredity principle). Given a group of confounding ECI, the one at the top of the hierarchy should always be evaluated. For an infinite lattice, i.e., $\mathrm{N} \to \infty$, the confounding is complex and may not be apparent. We shall address this in the next section.

6.5 Structures with Periodically Repeated Boundaries

For the CE to simulate correctly thermodynamics of bulk alloy systems, the CE has to be based on structures (or configurations) on an infinitely repeating lattice ($\mathrm{N} \to \infty$). Hence, structural energies are calculated using periodic boundary. Typically in CE, the clusters and configurations are classified according to the underlying symmetry of the lattice. The number of symmetry unique structures and that for clusters are equal. For structures, only the symmetry unique ones require evaluation via DFT, where methods exist for distinguishing the symmetry unique ones [8, 179]. When the clusters are classified according to symmetry, the CE in Eq. (6.1) can be re-expressed as

$$\frac{\mathrm{E}(\vec{\sigma})}{\mathrm{N}} = \sum_{n,f} D_{nf} J_{nf} \left\langle \Phi_{nf} \right\rangle_{\vec{\sigma}} \quad , \tag{6.25}$$

where symmetry unique clusters are classified under the labels n and f. Here n is the number of sites making up the cluster (e.g., n=2 for pairs) and f enumerates symmetry distinct clusters with the same n, according to a range-dependent hierarchy [6] (e.g., for pairs, f=1 for nearest neighbor and f=2 for next nearest neighbor in an FCC lattice) and there are D_{nf} degenerate clusters for each group (e.g., D_{21}=12 for nearest neighbor pairs in an FCC lattice). Clusters with the same label have the same ECI and the cluster function is averaged over all lattice sites,

$$\left\langle \Phi_{nf} \right\rangle_{\vec{\sigma}} = \frac{1}{\mathrm{N}} \sum_{i_1}^{\mathrm{N}} \frac{1}{n D_{nf}} \sum_{d}^{D_{nf}} \Phi_{\eta_{nfd}}(\vec{\sigma}) \quad , \tag{6.26}$$

where η_{nfd} is the set of lattice sites, $\{i_1, ..., i_n\}$, making up a degenerate n-site cluster grouped under n, f. For a periodic structure, the site averaging is done within the finite-size unit cell.

To illustrate how the ECI are confounded for a limited set of structures, we look at a 2-site supercell in the FCC lattice, defined by the translation vectors $[1\ 1\ 0], [1\ -1\ 0], [0\ 0\ 2]$ (see Fig. 6.1). The single-site cluster function, $\Phi_{\{i\}} \equiv \sigma_i$, at sublattice $i \in \{1, 2\}$ is 1 (-1) if occupied by B (A). The 2-site supercell forms a 'closed' configuration subspace, consisting of 2^2 configurations, of which, three have unique energy values (i.e., AA, AB and BB). Hence at best, one can solve for three symmetry unique ECI via SI.

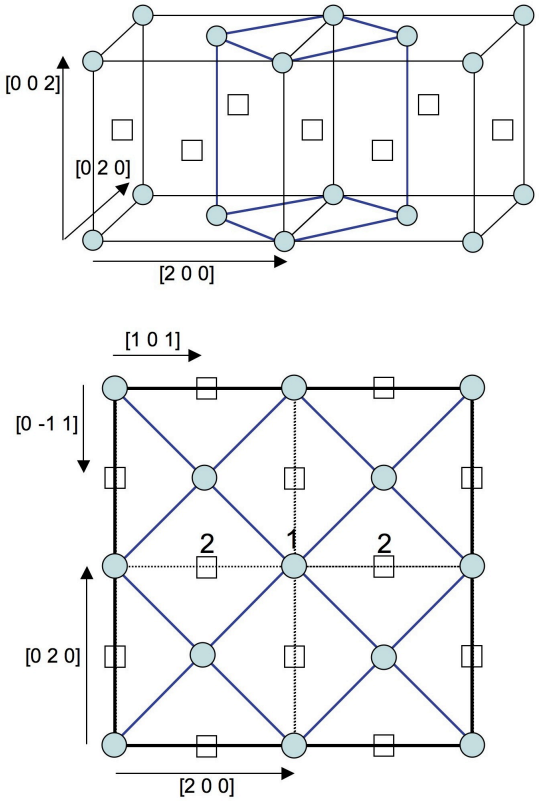

Figure 6.1: FCC lattice viewed in 3-D (top) and along the [0 0 1] direction (bottom), with corner (circle) and face-centered (square) sites marked out. The 2-site supercell given by the translation vectors, $[1\ 1\ 0], [1\ -1\ 0]$ and $[0\ 0\ 2]$, is periodically repeated, with circles denoting sublattice 1 and squares sublattice 2, and is shown relative to the 4-site cubic cell.

Confounding relations: Using only the three aforementioned structures to obtain $\hat{\vec{J}}_1$ via (6.7), we show how it is a bias estimator of $\vec{J}_1$, by listing the confounding relations between the symmetry unique ECI in $\vec{J}_1$ (see Table 6.1). Each symmetry unique class of ECI is subdivided into sublattice-dependent groups defined by $\{s_1, ..., s_n\}$, where each element, s_i, denotes the sublattice type (either 1 or 2) at site i of the n-site cluster (see Fig. 6.1)

associated with the ECI. Because the configuration subspace is 'closed', the confounding relations are conveniently found by noting that $\sigma_i\sigma_j = 1$, if $s_i = s_j$. Using 'C' as the (spin independent) constant term, which serves as the identity, we develop the following mathematical shorthand,

$$\begin{aligned} \sigma_i\sigma_j &\Leftrightarrow s_i s_j \quad , \\ s_i \mathrm{C} &\rightarrow s_i \quad , \\ s_i s_j &\rightarrow \mathrm{C}, \text{ if } s_i = s_j \quad . \end{aligned} \tag{6.27}$$

For example, $11 \rightarrow$ C and $112 \rightarrow 2$. From Table 6.1, we have 3 separate confounding relations,

1. Constant, group C: $\{J_0, J_{21}, J_{22}, J_{23}, ..., J_{41}, ...\}$.
2. 1-site, group 1 or 2: $\{J_{11}, J_{31}, ...\}$.
3. 2-site NN, group 12: $\{J_{21}, J_{23}, ...\}$.

Note that we have listed the ECI according to hierarchy [6], as such the three ECI to be determined via SI (Eq. (6.7)) are J_0, J_1 and J_{21}, which constitute $\vec{J}_1$, with the rest assumed negligible, otherwise a bias occurs as given in (6.9). Note that, although some degenerate ECI from the J_{21} class falls into the constant group, they are unconfounded because the value of J_{21} is determined; all columns in $\boldsymbol{\phi}_{11}$ associated with J_{21} class are averaged over, according to Eq. (6.26). The importance of hierarchical arrangement becomes clear, without which, one would equally likely choose J_{22}, J_{31} and J_{23} to be evaluated and still get a solution (because these interactions are not confounded) but at the expense of neglecting the physically more important ones.

The configuration subspace generated by the 2-atom cell is insufficient to unconfound all physically important ECI for a general alloy. The relevant question is thus whether a configuration subspace allows all significant ECI to be predicted via (6.9), which would lead to a $\hat{\vec{J}}_1$ that has negligible bias because $\vec{J}_2$ is small. In this case, the ECI of the truncated CE set approaches that of the unique non-truncated CE. To this end we offer the following

Table 6.1: Indices (n, f) of an exemplar list of symmetry distinct clusters with degeneracies D_{nf}. Each symmetry distinct class is subdivided into sublattice-dependent groups, with $\{s_i\}$ denoting the sublattice types (according to Fig. 6.1) of the cluster sites, and its number of instances is given by $D_{\{s_i\}}$. The notation is reduced according to the shorthand developed in (6.27) (listed under 'Red.' column), which is used to group confounded ECI (under Group). The last column lists the coordinates of sites constituting an exemplar cluster from each group (see Fig. 6.1).

n	f	D_{nf}	$\{s_i\}$	Red.	Group	$D_{\{s_i\}}$	E.g.
0	1	1	C	C	constant	1	—
1	1	1	1	1	1-site	1	[0 0 0]
2	1	12	11	C	constant	4	[0 0 0], [1 1 0]
			12	12	2-site NN	8	[0 0 0], [1 0 1]
2	2	6	11	C	constant	6	[0 0 0], [2 0 0]
2	3	24	11	C	constant	16	[0 0 0], [2 1 1]
			12	12	2-site NN	8	[0 0 0], [1 1 2]
3	1	24	112	2	1-site	16	[0 0 0], [1 1 0], [1 0 1]
			122	1	1-site	8	[0 0 0], [1 0 1], [0 1 1]
4	1	8	1122	C	constant	8	[0 0 0], [1 1 0], [1 0 1], [0 1 1]

step-by-step resolution:

1. We first define a large supercell and all its associated configurations as our 'complete' Hilbert space.

2. A reasonable size supercell within the Hilbert space is selected as the initial subspace, with confounded ECI identified. Using first-principles energies from structures in this subspace as $\vec{E}_1$, we evaluate $\hat{\vec{J}}_1$, which can be used as an initial screen for significant and/or insignificant ECI.

3. Based on a physical hierarchy for clusters, the confounding relations and the values of $\hat{\vec{J}}_1$, we identify important ECI that are confounded.

4. We unconfound each targeted ECI by including a structure systematically from the Hilbert space (but not in the initial subspace) to $\vec{E}_1$.

The unique ECI of the alloy is approached when the subspace created by structures in $\vec{E}_1$ is large enough to unconfound all important ECI. We will show in a later section (using Ag-Au alloy as case study) that the truncated ECI, resulting from the above systematic

increment of the configuration subspace, has comparable predictive capability as the one selected using cross-validation method, but using only one-third the number of structural energies for SI. Before this, we shall illustrate the ideas using a fictitious model Hamiltonian.

6.5.1 An Illustrative Example on Subspace Projection

A fictitious (binary alloy) model is created on an FCC lattice, such that all structural energies are defined by interactions within the NN range, i.e., only $J_0, J_{11}, J_{21}, J_{31}, J_{41} \neq 0$, with values shown in Table 6.2. In this example, we do not *a priori* know the values of these interactions, but assume that the NN clusters span the complete space we will be working with. We then start by using the configurations generated by the 2-sublattice cell (AA, AB and BB) in Fig. 6.1 to calculate the estimator (chosen by a physical hierarchy), $\hat{\vec{J}}_1 = [\hat{J}_0, \hat{J}_{11}, \hat{J}_{21}]^{\mathrm{T}}$, via (6.7). Because we did not span the complete space, $\hat{\vec{J}}_1$ is biased, as seen in Table 6.2, and the values obtained are explained by the confounding relations in the previous subsection, e.g., $\hat{J}_0 = J_0 + (D_{41}/4)J_{41}$. We then seek to add symmetry unique structures beyond the initial subspace to unconfound J_{31} and J_{41}. By including additional structures generated by the 4-site cubic cell (A_3B and AB_3), the complete space is spanned and $\hat{\vec{J}}_1$ is an unbiased estimate of $\vec{J}_1$, as shown in Table 6.2.

Hence, if we were lucky enough to choose a subspace of lattice configurations that is spanned by all non-zero, significant J_{nf} of the real-world alloy Hamiltonian, we would recover an accurate CE. However, we can never know this *a priori*. Therefore, a physical hierarchy of interactions due to the moment theorem [180–182] is required, i.e., $J_{2f} > J_{3f} > J_{4f} > ...$, to ensure that all subclusters are included. By increasing the configuration subspace systematically, we can progressively build up knowledge of significant J_{nf} within a local subspace. In addition, lower order ECI, in particular J_{2f}, are of longer range. The original local subspace can be expanded by including selected configurations from an augmented space to unconfound long-range but significant J_{2f}, keeping the number of required structures (for SI) to a minimum. Indeed, we now showcase these properties with Ag-Au.

Table 6.2: J_{nf} and their degeneracies D_{nf} for a model Hamiltonian on FCC lattice. The estimate, $\hat{J}_{nf}$, via structural inversion is shown for structures belonging to the subspace of a 2-site cell and the complete space given by the 4-site cubic cell.

			J_{nf}	$\hat{J}_{nf}$	
n	f	D_{nf}	Model	2-site cell	4-site cell
0	1	1	1	0.8	1
1	1	1	-1	-0.2	-1
2	1	12	1	1	1
3	1	24	0.1	0	0.1
4	1	8	-0.1	0	-0.1

6.6 Subspace Projection Methodology

We next apply the discussed concepts to the FCC Ag-Au system. A large cubic 32-atom cell is defined as our parent space (32-Cubic) from which smaller subspaces (8-atom cell of different shapes) are utilized. The hierarchy, based on the compact and locally complete basis rule [6], is as follows:

1. Lower order clusters with smaller index n are more important. Specifically, if an n-body cluster is included for evaluation, its subclusters of lower order should be included too.

2. For fixed n, clusters of smaller spatial extent are more important.

The first rule is analogous to the heredity principle in fractional factorial design and it also implies that lower order clusters remains important up to a larger spatial extent (or longer range). For Ag-Au, the CE set using subspace projection, shows that important multibody clusters ($n > 2$) are indeed shorter range than important pairs. Thus important multibody ECI are unconfounded by just utilizing a fraction of the structures belonging to the 8-atom subspaces, i.e., 8-Rh and 8-DO_{22} (see Table 6.3). Pairs being longer range, require structures from an augmented space to be unconfounded, because the 32-Cubic space only unconfounds up to the 5th NN pair. This allows greater flexibility than the original fractional factorial design methodology as it unconfounds pairs (which are longer range than multibodies in general) by adding only a few selected structures from the augmented space, keeping the list of structures required for structural inversion (SI) small. For clarity,

when we say a higher order ECI is unconfounded, it implies that the ECI is unconfounded from lower order (smaller n) and shorter range (possibly having the same n) ECI.

6.6.1 Subspaces

Two 8-atom subspaces of the 32-Cubic 'full' space are considered in this study; the 8-Rh and the 8-DO_{22} subspaces, which consist of structures generated by a symmetric rhombohedral cell and a (less symmetric) rectangular cell respectively. The translation vectors of these cells are given in Table 6.3 and illustrated in Fig. 6.2. The complete space of each 8-atom subspace consists of 2^8 configurations. However due to the underlying lattice symmetry and the cell shape, there are only 16 and 27 unique structures for the 8-Rh and 8-DO_{22} respectively, with the same maximum number of symmetry distinct ECI admissible for SI. These 2 subspaces overlap, with structures forming the groundstate hull of Ag-Au, generated by the 4-Cubic space ($L1_0$, Au-rich $L1_2$, Ag-rich $L1_2$, pure Ag and Au) common in both. Low-energy configurations related to DO_{22} structure are only present in 8-DO_{22}.

From Fig. 6.2, the confounding relations for the subspaces could be worked out completely. Using pairs as example for the 8-Rh subspace, the NN and 2nd NN pairs are not confounded with more important clusters of lower order or shorter range. This is, however, not true for longer range pairs, e.g., the 4th NN (J_{24}) and the 3rd NN (J_{23}) pairs are confounded with J_0 and the NN pair (J_{21}) respectively. For 8-DO_{22}, pairs up to 3rd NN are not confounded. In this case, depending on the direction, J_{24} is confounded with either J_0 or J_{22}; e.g., from Fig. 6.2, [2 2 0] is confounded with [2 0 0] while [2 0 2] is confounded with itself for the 8-DO_{22} cell.

6.6.2 Applying Fractional Design Principles to Subspaces

When all structures in each of the 8-Rh and the 8-DO_{22} subspaces are utilized, the CE set contains many multibody interactions and for the Ag-Au system they are in general weaker than that of the pairs (see Table 6.4). When a fraction of the structures are utilized for SI, the higher order and weaker multibody interactions are confounded with the stronger lower order ones (e.g., pairs and triplets). As will be shown in the next section, the quality

Table 6.3: Translation vectors of FCC supercells representing the various spaces (see Fig. 6.2), with lattice constant $a = 2$. The number of sites and symmetry unique structures for each cell (subspace) are listed under N_s and N_c respectively, with some exemplar structures shown in the last column. The 4-Cubic space is a subspace of 8-Rh and 8-DO_{22}, which in turn form (overlapping) subspaces within the 32-Cubic space. N_c was not evaluated exactly for the 32-Cubic, which covers a space of 2^{32} non-unique configurations.

Sub-spaces	N_s	Translation vectors	N_c	E.g.
4-Cubic	4	[2 0 0], [0 2 0], [0 0 2]	5	Ag, Au, $L1_0$, $L1_2$
8-Rh	8	[2 2 0], [2 -2 0], [0 2 2]	16	4-Cubic, ...
8-DO_{22}	8	[2 0 0], [0 4 0], [0 0 2]	27	4-Cubic, DO_{22}, ...
32-Cubic	32	[4 0 0], [0 4 0], [0 0 4]	—	All above, ...

of the CE is not affected, because the neglected multibody interactions are small.

6.6.3 Combining Structures from Different Subspaces

As mentioned, pairs beyond 3rd NN are confounded with clusters of lower order and shorter range in 8-DO_{22} subspace. To unconfound the 4th NN, it suffices to combine 8-DO_{22} with non-overlapping configurations from 8-Rh. To unconfound J_{25}, a structure from an augmented space within the 32-Cube space (but $\perp$ to 8-Rh and 8-DO_{22}) was added. To unconfound J_{26} and longer ranged pairs, structures from an augmented space $\perp$ to 32-Cubic are needed, which, for Ag-Au, just 3 were required to produce a good quality CE.

6.6.4 Practical Considerations and Implementation

For an arbitrary given set of structures there is always a unique set of confounding relations between the ECI. However, there is no guarantee that important interactions are not confounded with each other. We will show that, when structures are judiciously selected from the various subspaces (8-Rh, 8-DO_{22} and augmented), the following implementation ensures that smaller order and shorter range clusters, which are physically more important [6], are unconfounded first:

1. Lower order interactions (smaller n) are considered first (i.e., J_0, J_1, J_{2f}, J_{3f}, ...).

2. For a given n, shorter range interactions are considered first (e.g., J_{21}, J_{22}, J_{23}, ...).

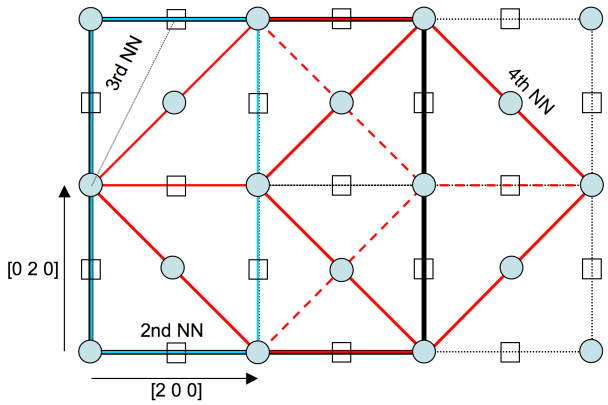

Figure 6.2: (color online) Top view of the FCC lattice along the [0 0 1] direction, with corner (circle) and face-centered (square) sites marked out. The 8-site supercells forming the 8-Rh (red) and 8-DO_{22} (blue) subspaces, are superposed on the 32-Cubic (bold black) cell (see Table 6.3 for translation vectors). For convenience, the lattice constant (corresponding to 2nd NN) is given 2 units. The translation vectors forming the 8-Rh cell have 4th NN distance, resulting in the confounding of the 4th NN pair interaction and constant term J_0. For the 8-DO_{22} subspace, the 4th NN pair is confounded either with J_0 or the NN pair.

3. If it is not confounded with the list of ECI with lower order and shorter range, an interaction is added to the list. Confounding is detected when the SI matrix, $\boldsymbol{\phi}_{11}^{\mathrm{T}}\boldsymbol{\phi}_{11}$, is singular.

4. The process is stopped once the matrix, $\boldsymbol{\phi}_{11}$, is full ranked, i.e., the number of symmetry distinct structures used equals number of symmetry distinct clusters, and a final SI is performed to obtain the unconfounded ECI.

This implementation can also serve to identify unsatisfactory sets of structures, in which physically less significant ECI are unconfounded before the more important ones, such as in the complete structural set generated by the (less symmetrical) 8-DO_{22} cell.

6.7 Results and Discussion

For Ag-Au alloy, we use a database of 95 DFT formation energies (both from smallest first algorithm [56] and the 8-atom subspaces), $\mathrm{E}_f^{\mathrm{DFT}}$, for construction and verification of various

sets of CE. The formation energy is defined as

$$\mathrm{E}_f(\vec{\sigma}) = \mathrm{E}(\vec{\sigma}) - c(\vec{\sigma})\mathrm{E}(\mathrm{Au}) - (1 - c(\vec{\sigma}))\mathrm{E}(\mathrm{Ag}) \quad , \tag{6.28}$$

with $c(\vec{\sigma})$ being the concentration of Au in the given structure defined by σ. The $\mathrm{E}_f^{\mathrm{DFT}}$ are estimated to be convergent within the range of 0.1 meV to $\sim$1 meV. The subspace projection method in Section 6.6 is explored by using a fraction of structures from 8-Rh, 8-DO_{22} and augmented subspaces. To distinguish different sets of CE from subspace projection, we classify the structures used in each CE set by the tuple {a, b, c}; "a" is the number of structures from 8-Rh, which includes all structures generated by 4-Cubic space (see table 6.3), "b" gives the number of additional structures from 8-DO_{22} not found in 8-Rh, and "c" is the number of additional structures from the augmented space $\perp$ to both 8-Rh and 8-DO_{22}. The total number of structures used is thus a+b+c.

The quality of each CE set is evaluated by the root-mean-square (rms) deviation of $\mathrm{E}_f^{\mathrm{CE}}$ with respect to $\mathrm{E}_f^{\mathrm{DFT}}$ for all 95 Ag-Au structures, i.e.,

$$\varepsilon_{\mathrm{rms}} = \left[\frac{1}{95}\sum_{i=1}^{95}\left(\mathrm{E}_{f(i)}^{\mathrm{DFT}} - \mathrm{E}_{f(i)}^{\mathrm{CE}}\right)^2\right]^{1/2} \tag{6.29}$$

We show that the judicious choice of (just) $\sim$ 16 structures, via consideration of various subspaces, results in a unique set of CE interactions that reproduces well the 95 $\mathrm{E}_f^{\mathrm{DFT}}$, within the accuracy of the DFT calculated $\mathrm{E}_f^{\mathrm{DFT}}$, as compared to 55 structures used for previous study [56].

6.7.1 CE Sets from Subspace Projection

The ECI and E_f versus composition diagrams for various CE sets from subspace projection are shown in Table 6.4 and Fig. 6.3, respectively. Starting with the CE set {5, 0, 0}, where the full 4-Cubic subspace is used, there are 5 symmetry unique structures, which incidentally are groundstate structures in Ag-Au, allowing only 5 ECI (up to the NN range) to be unconfounded. Under subspace projection, the interactions are obtained from SI of a full rank $\boldsymbol{\phi}_{11}$, hence the $\mathrm{E}_f^{\mathrm{DFT}}$ of the 5 structures are reproduced exactly by CE. Although $\mathrm{E}_f^{\mathrm{DFT}}$

of structures (fig. 6.3(a)) at the groundstate hull are reproduced well, some structures are not distinguishable due to the small set of ECI used. Among ECI responsible for ordering (n$\geq$ 2) and order-disorder phase transitions, the NN pair (J_{21}) dominates, as proven in previous study [56] via direct first-principles calculations.

Set {16, 0, 0} (fig. 6.3(b)), where all structures from the 8-Rh subspace (which encompasses the 4-Cubic subspace) are utilized, unconfounds more multibody interactions, of which those with $n \geq 5$ are negligible (<0.005meV), because they are smaller than the convergent error of E_f^{DFT} data. The ε_{rms} for E_f is similar to the {4, 0, 0} set. The use of only a fraction of the structures, {8, 0, 0}, results in only a slight increase in ε_{rms} (see Fig. 6.3(c)) and a minimal change in values of ECI. Hence, confounding the small ECI (with $n \geq 5$) do not change the quality of the CE. In particular, none of the CE sets discussed thus far distinguishes the E_f of $L1_2$ and DO_{22} structures at 0.75 Au.

In line with the physical insight that lower order interactions (i.e., pairs) are longer range, we seek to include longer range pairs. Four DO_{22} related structures from 8-DO_{22} subspace are added and the resulting {8, 4, 0} set unconfounds the 3rd NN and 4th NN pairs and reduces ε_{rms}. The E_f^{CE} of $L1_2$ and DO_{22} are now distinguishable and exactly reproduces E_f^{DFT} (see fig. 6.3(d)).

Because combining 8-Rh and 8-DO_{22} at best unconfounds the 4th NN ECI, structures from an augmented space (see table 6.5) are required to unconfound longer range pairs. Two structures at 0.5 Au are added in turn to give sets {8, 4, 1} and {8, 4, 2} (Figs. 6.3(e) and 6.3(f)); unconfounding J_{25} and J_{26} leads to significant improvement in ε_{rms}, which are now within the convergent errors of most of our E_f^{DFT} data. It is noted that the unconfounding of J_{25} and J_{26} did not lead to any change in the multibody ECI, because they were originally only confounded with lower order terms and shorter range pairs. Unconfounding J_{27} and J_{34} with set {8, 4, 4} further reduces ε_{rms} to 0.42 meV. We thus obtained a good quality CE set for Ag-Au using only 16 structures.

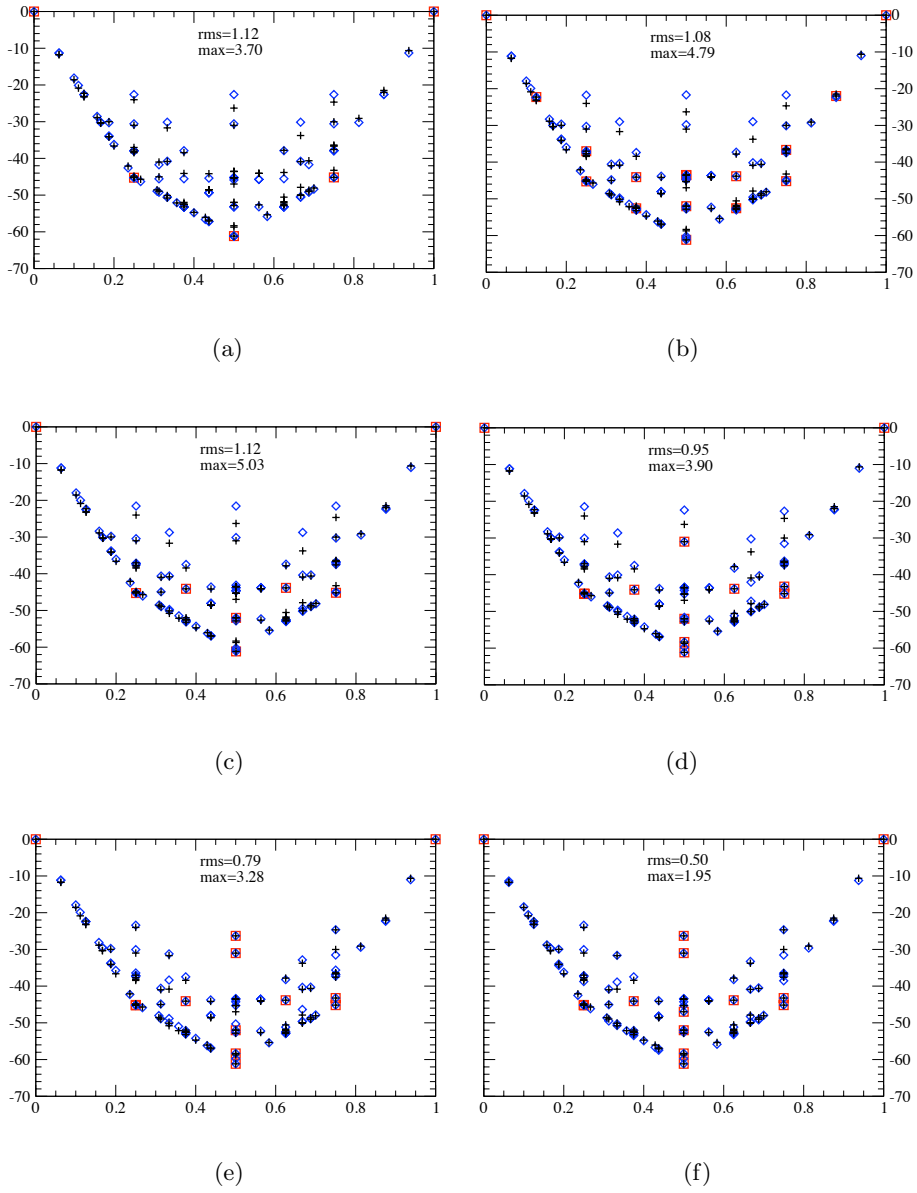

Figure 6.3: (color online) E_f^{CE} (meV) (diamonds) from CE sets using subspace projection, (a) {5, 0, 0}, (b) {16, 0, 0}, (c) {8, 0, 0}, (d) {8, 4, 0}, (e) {8, 4, 1} and (f) {8, 4, 2} vis-a-vis E_f^{DFT} ('+') for each of the 95 Ag-Au structures, plotted against atomic fraction of Au. Structures used for structural inversion (SI) are marked out by (red) squares. The rms (ε_{rms}) and maximum (ε_{max}) deviation of E_f^{CE} from E_f^{DFT} are given for each CE set. Only structures (including $L1_0$ and $L1_2$) from the 8-Rh subspace are included in (a) to (c), which unconfounds up to 2nd NN pair at most, and they have similar ε_{rms}. Adding 4 structures from 8-DO_{22} cell (see (d)) unconfounds the 4th NN apir, with significant improvement in ε_{rms}. However high-energy structures are not reproduced well, which can only be improved by unconfounding the 5th and 6th NN pair, (e) and (f) respectively, with (up to) 2 additional structures from the augmented space.

Table 6.4: J_{nf} (in meV) and their degeneracies D_{nf} for Ag-Au for different sets of CE. For the subspace projection method, the tuplet {a, b, c} gives the number of symmetry distinct structures (see text) from 8-Rh, 8-DO_{22} and augmented spaces respectively. Left blank are ECI of clusters not used during SI while those with magnitude smaller than 0.005 meV are listed as 0.00 (or -0.00). {16, 0, 0} set contains 5 other ECI (with $5 \leq n \leq 8$) that are not listed as their magnitudes are smaller than 0.005 meV. For comparison, we show results from cluster selection via CV_1 score [56] with ECI obtained via L.S, using 55 structures as the learning set. The rms ($\varepsilon_{\rm rms}$) and maximum ($\varepsilon_{\rm max}$) deviation of $E_f^{\rm CE}$ with respect to $E_f^{\rm DFT}$ are shown with references to the figures of E_f v.s Au composition.

			J_{nf} (meV)									
n	f	D_{nf}	{5, 0, 0}	{16, 0, 0}	{8, 0, 0}	{8, 4 ,0}	{8, 4, 1}	{8, 4, 2}	{8, 4, 4}	{8, 4, 6}	CV_1	
0	1	1	-3010.31	-3009.22	-3009.26	-3008.98	-3008.98	-3010.21	-3010.21	-3010.52	-3010.48	
1	1	1	-238.13	-237.90	-237.89	-237.89	-237.89	-237.89	-237.35	-237.25	-237.23	
2	1	12	7.65	7.61	7.58	7.24	6.59	6.79	6.79	6.90	6.88	
	2	6		-0.33	-0.35	-0.35	-0.35	0.06	0.06	0.06	0.10	
	3	24				0.17	0.17	0.17	0.36	0.28	0.28	
	4	12				-0.05	-0.05	0.16	0.16	0.16	0.15	
	5	24					0.33	0.22	0.22	0.17	0.15	
	6	8						-0.31	-0.31	-0.31	-0.25	
	7	48							-0.09	-0.05	-0.05	
	8	6								0.10	0.12	
3	1	24	-0.00	0.00	-0.00	-0.31	-0.31	-0.31	-0.18	-0.18	-0.18	
	2	36		-0.02	-0.02	-0.02	-0.02	-0.02	-0.02	-0.00	-0.06	
	3	72				0.10	0.10	0.10	0.06	0.06	0.06	
	4	18							-0.09	-0.11	-0.05	
	5	72								-0.00		
4	1	8	-0.16	-0.07	-0.16	-0.07	-0.07	-0.07	-0.07	-0.07	-0.08	
	2	48		0.02	0.03	0.03	0.03	0.03	0.03	0.03		
	3	48		-0.02		-0.02	-0.02	-0.02	-0.02	-0.02		
	4	12		-0.03								
$\varepsilon_{\rm rms}$			1.12	1.08	1.12	0.95	0.79	0.5	0.42	0.42	0.33	
$\varepsilon_{\rm max}$			3.70	4.79	5.03	3.90	3.28	1.95	1.41	1.22	0.88	
Figure			6.3(a)	6.3(b)	6.3(c)	6.3(d)	6.3(e)	6.3(f)	6.4(b)	—	6.4(a)	

Table 6.5: Translation vectors of 16 FCC structures (prior to atomic relaxation) used in CE set {8, 4, 4} with their affiliated subspaces given. The denominator in column 'Fraction Au' gives the number of sites in each structure. Structures SM#21, 27, 06 and 07 are from the augmented space $\perp$ to both 8-Rh and 8-DO_{22} subspaces, and except for SM#21 are also $\perp$ to the 32-Cubic space.

Tag	Fraction Au	Affiliated spaces	Translation vectors
Ag	0	All	[0 1 1], [1 0 1], [1 1 0]
Au	1	All	[0 1 1], [1 0 1], [1 1 0]
$L1_0$	1/2	8-Rh, 8-DO_{22}	[1 1 0], [1 -1 0], [0 0 2]
$L1_2$	1/4	8-Rh, 8-DO_{22}	[2 0 0], [0 2 0], [0 0 2]
$L1_2$	3/4	8-Rh, 8-DO_{22}	[2 0 0], [0 2 0], [0 0 2]
8-Rh#3	3/8	8-Rh	[2 2 0], [2 -2 0], [0 2 2]
8-Rh#7	4/8	8-Rh	[2 2 0], [2 -2 0], [0 2 2]
8-Rh#9	5/8	8-Rh	[2 2 0], [2 -2 0], [0 2 2]
DO_{22}	1/4	8-DO_{22}	[2 0 0], [0 2 0], [1 1 2]
DO_{22}	3/4	8-DO_{22}	[2 0 0], [0 2 0], [1 1 2]
SM#13	2/4	8-DO_{22}	[2 0 0], [0 2 0], [1 1 2]
SM#24	2/4	8-DO_{22}	[4 0 0], [0 1 -1], [0 1 1]
SM#21	2/4	Aug., in 32-Cubic	[1 -1 0], [2 2 0], [0 0 2]
SM#27	2/4	Aug., $\perp$ 32-Cubic	[3 3 2], [0 1 -1], [-1 0 1]
SM#06	1/3	Aug., $\perp$ 32-Cubic	[1 1 0], [1 -1 0], [1 0 3]
SM#07	2/3	Aug., $\perp$ 32-Cubic	[1 1 0], [1 -1 0], [1 0 3]

6.7.2 Comparison with Optimal CE that Utilizes CV_1

To show the uniqueness of the CE ECI, set {8, 4, 4} from subspace projection was compared with that obtained via CV_1 selection using 55 structures from smallest first algorithm [56] as the learning set, as described in Section 5.2. We emphasize that our CV_1 selection procedure also follow the hierarchical ordering of cluster set forth [6], unlike others [59]. Although ε_{rms} from the optimal CV_1 set is lower by 0.1 meV (see Fig. 6.4), 3 times more structures had been used in the learning set. To facilitate comparison of the ECIs, we further unconfound J_{28} and J_{35} using set {8, 4, 6}, with insignificant improvement in ε_{rms} versus {8, 4, 4}. As observed in table 6.4, the ECI of {8, 4, 4} , {8, 4, 6} and 55-structure-fit are very close to one another, signifying a convergence in the ECI values (within the convergent errors of E_f^{DFT}). The ECI values are thus unique for a given alloy system with an attached physical meaning, and should not merely be treated as coefficients obtained from statistical fitting.

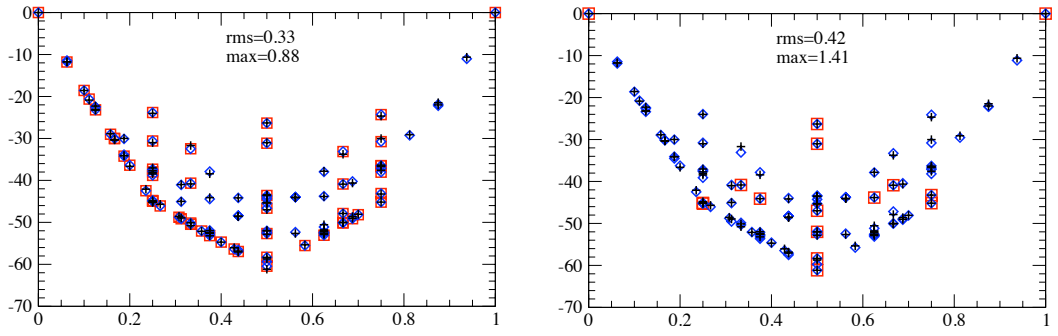

(a) (b)

Figure 6.4: (color online) E_f^{CE} (meV) versus fraction Au (diamonds) using (a) L.S fit to 55 structures with cluster set selected via CV_1 (marked by squares) and (b) CE from the {8, 4, 4} subspace, compared to E_f^{DFT} ('+').

6.8 Summary

In this chapter, we showcased a method for selecting important cluster interactions ($\vec{J}_1$), which are *a priori* unknown, to construct a reliable and unique truncated CE. Because only a subset of 2^N possible structural energies (from the configuration space of a binary alloy) is used to evaluate $\vec{J}_1$, the estimator, $\hat{\vec{J}}_1$, obtained via SI (Eq. 6.7) is biased; there are linear dependencies between the truncated cluster basis. Importantly, the complete correlation matrix, $\mathbf{\Phi}$, is a Hadamard matrix, and using fractional factorial design principles, we elucidate how the linear dependencies can be determined and quantify the errors incurred, when $\hat{\vec{J}}_1$ is used to evaluate the data set, $\vec{E}$. In fractional factorial design, the experimental observations can be explained by a set of factors and their interactions. Each factor takes discrete levels and each combination of factors denotes a possible experiment, analogous to spin variables used to describe a given configuration. We then show that these concepts are applicable to the selection of truncated CE basis and the method for determining cluster dependencies are carried over, even though periodic boundary conditions are applied to alloy configurations. Coupled with a physical hierarchy that ranks the relative importance of clusters (according to the number of sites and spatial extent), the dependency relation indicates whether two important ECI are confounded – a term used in fractional factorial

design to imply that interactions are correlated, and its impossible to separate their individual contributions. To remove the targeted confounding, new energies from structures of selected subspaces are added to the SI equation. Using Ag-Au alloy as a case study, we show the various subspaces generated by unit cells in the 32-cubic box. Because pairs remain important out to a longer range, we show how longer range pairs are unconfounded using structures from an augmented space. The resulting truncated CE is unique (when all important interactions are unconfounded) and shows good predictive capability, using only a minimal set of first-principles structural energies in the process. We used only one-third the structural energies used by current methods based on cross-validation measures.

CHAPTER 7

AN IMPROVED CLUSTER MEAN-FIELD THEORY FOR ISING HAMILTONIANS VIA SELF-CONSISTENT COARSE-GRAIN RELATIONS

Given a reliably constructed cluster expansion (CE) Hamiltonian for an alloy, thermodynamic quantities are calculable using the partition function as shown in (2.9). Direct evaluation of the partition function is often intractable for an infinite lattice. Even for the simple Ising model (pair interactions only), exact solution is known only for a few cases [183]. Hence, for thermodynamic calculations and phase diagram constructions, one often rely on stochastic techniques such as Monte Carlo (MC) to sample important configurations or mean-field theories (MFTs), which approximates the partition function by neglecting correlations beyond a finite cluster size. Reliable MC simulations are computaitonally expensive, often requiring a big simulation box of 10^4 to 10^6 lattice sites. On the other hand, the reliability of MFTs varies greatly with the complexity of the model; simple single-site MFT (such as the Weiss model) predicts the wrong phase diagram topology for frustrated systems, while the more accurate cluster variation method (CVM) [45–47] involves a highly complicated approximation of the cluster entropy. However, the above MFTs do not maintain thermodynamic consistency as the variables calculated from the finite cluster violates mathematical relations at the lattice level.

7.1 Introduction

As such, we derive a cluster mean-field theory (cMFT) that uses a cluster-lattice Fourier transform to relate the cluster to the coarse-grained (CG) lattice. The site magnetization (m_i) and pair correlations (G_{ij}) obtained from a cluster-approximated partition function ($\hat{\mathrm{Z}}$[A], with source fields A), are required to obey a set of relations derived from the entire lattice. We apply it to the study of the Ising Hamiltonian (a CE with pair-only interactions),

offering a much improved prediction of phase diagram topologies, even with just a single-site cluster.

A cMFT strategy is straightforward: A finite-size cluster containing N_c sites is treated (more) accurately while the remaining sites in the infinite lattice outside the cluster interact via static mean fields, which consist of averaged quantities (e.g., m_i and G_{ij}) derived from the cluster partition function. Calculated correlations are local within the cluster and, for $N_c = 1$, the correlations are neglected, resulting in poor predictions of transition temperatures (T_c), especially for frustrated systems.

For classical, static Hamiltonians, to improve on the prediction of cluster quantities, as well as phase boundary topology and T_c, we utilize the Dyson's equation that relate the pair correlations G of an N-site lattice and the Ising interactions J via the self-energy Σ. We then enforce the consistency, which is neglected in most MFTs, between the lattice G and the cluster $\hat{G}$ evaluated from the cluster partition function. (We denote cluster quantities with a "*hat*".) Although this consistency is straightforward to enforce in the $N_c = 1$ case, one has to consider the effect of boundary conditions on the consistency conditions for general sized clusters, which destroy the translational invariance of the original lattice. In this context, for the Ising Hamiltonian we adapt the self-consistency ideas used in quantum cluster methods, namely, cellular DMFT (cDMFT) [184] and DCA [185], commonly used in quantum Monte Carlo (MC) simulations of correlated-electron physics. Both cDMFT and DCA use a cluster-lattice Fourier transform that invoke specific and different boundary conditions. The DCA, for example, recovers the (static) coherent-potential approximation [186, 187] for $N_c = 1$, but it is a proper generalization for $N_c > 1$ that enforces the same correlation length in real ($\mathbf{r}$) space or Fourier ($\mathbf{k}$) space by coarse-grained (CG) $\mathbf{k}$-space integrals [188]. Besides dynamical cases, these same concepts can be applied to static, classical thermodynamics. For the correlated-electron case, T_c's are improved via scaling versus N_c [189].

Utilizing these concepts, the lattice can be CG into non-overlapping cells of size N_{cell} sites and clusters of size N_c, where $N_{cell} \geq N_c$. We approximate the self-energy Σ with entries within (between) the cells being non-zero (zero). When $N_{cell} = N_c$, as in the DCA,

the lattice G is coarse-grained within a cell, and then is required to be self-consistent with cluster $\hat{\mathrm{G}}$. For $\mathrm{N}_c = 1$, this reduces to an integral sum rule for the on-site G_{ii} (see Sect. 7.2), resulting in dramatic improvement of the phase diagram, see Fig. 7.1. More generally, we explore a spectrum of MFTs applicable to the Ising Hamiltonian where we require the self-consistency to be obeyed for $\mathrm{N}_{\mathrm{cell}} > \mathrm{N}_c$; in particular, we investigate the efficacy of a non-coarse-grained (NCG) version with $\mathrm{N}_{\mathrm{cell}} = \infty$, which recovers a previous MFT [190, 191].

The chapter is organized as follows. Section 7.2 provides background on MFT Ising thermodynamics. The correct phase boundary topology and more accurate order-disorder T_c for an antiferromagnet (AFM) on an FCC lattice is obtained already for $\mathrm{N_c} = 1$ by enforcing the conservation of on-site correlation. In Sec. 7.3 we discuss the generalization of the method to multisite clusters, utilizing CG techniques from cDMFT and DCA to achieve self-consistency between lattice and cluster correlations. We call these CG (or NCG) DCA for convenience. We obtain a variational cluster Grand Potential for $\mathrm{N}_{\mathrm{cell}} \geq \mathrm{N_c}$. In Sec. 7.4 we apply both DCA and NCG-DCA theories to determine T_c, phase boundary topologies, and scaling of T_c versus $\mathrm{N_c}$ via Betts' clusters [192], comparing results to exact Monte Carlo (MC). In particular, we investigate the NCG version at *small* $\mathrm{N_c}$ and its computational efficiency and accuracy. For the ferromagnetic (FM) case, we show that the NCG variant is computationally faster, more rapidly convergent versus cluster size, and accurate, which may be useful for quantum cluster and cluster expansion applications.

7.2 Background

To extend MFTs (e.g., Weiss [193,194], Onsager [195–197] and Brout [198,199]), to multisite clusters, we focus on the Ising Hamiltonian in a uniform field, h, i.e.,

$$\mathrm{H} = -\frac{1}{2}\sum_{i,j} \mathrm{J}_{ij}\sigma_i\sigma_j - h\sum_i \sigma_i \tag{7.1}$$

where $\sigma_i = \pm 1$ is the two-state spin variable on site i, with pairs of spins interacting via J_{ij}. We denote ensemble averages with $\langle ... \rangle$. Hence, the site magnetization is $m_i \equiv \langle \sigma_i \rangle$

and the pair (two-site) correlations are

$$G_{ij} = \beta^{-1}\chi_{ij} \equiv \langle \sigma_i \sigma_j \rangle - \langle \sigma_i \rangle \langle \sigma_j \rangle \qquad i \neq j \tag{7.2a}$$

$$\equiv \qquad 1 - m_i^2 \qquad i = j \tag{7.2b}$$

where $\beta^{-1} \equiv k_B \mathrm{T}$ (k_B is Boltzmann's constant), and χ is the susceptibility. G_{ii} and m_i obey the sum rule in (7.2b), i.e., scattering intensity is conserved, because σ_i^2 and $\langle \sigma_i^2 \rangle$ are 1. MFTs typically overly correlate, through self interactions, the spins on two (or more) sites, such that (7.2b) is violated. Notably, G and H are always related as shown by diagrammatic expansions [200]; that is, G satisfies a Dyson's equation relating the self-energy Σ, the irreducible part in the expansion, and the J's, i.e.,

$$\Sigma = G_0^{-1} - \mathrm{G}^{-1}, \tag{7.3}$$

where $G_0^{-1} = -\beta \mathrm{J}$, and all matrices are N×N for an N-site lattice (N is large). Given known J's, the self correlation G_{ii} from (7.3) satisfy (7.2b) only for the correct Σ.

The ensemble averaged energy $\mathrm{E}_{avg} = \langle \mathrm{H} \rangle$ from (7.1) is expressed as single-site energy E_1 and *correlation energy* E_2, approximated (or ignored) in MFTs, i.e.,

$$\mathrm{E}_{avg} \quad = \quad -\frac{1}{2}\sum_{i,j} \mathrm{J}_{ij} m_i m_j - h \sum_i m_i - \frac{1}{2}\sum_{i,j} \mathrm{J}_{ij} G_{ji} \quad . \tag{7.4}$$

From (7.3), E_2, the last term in (7.4), can be written in terms of G and Σ as

$$\mathrm{E}_2 = \frac{k_B \mathrm{T}}{2} \mathrm{Tr}(1 + G\Sigma) \quad . \tag{7.5}$$

In general, E_2 cannot be solved exactly but it can be estimated within a finite cluster of size $\mathrm{N_c}$ while enforcing proper self-consistency of $\hat{\mathrm{G}}$ and $\hat{\Sigma}$ in (7.3) via CG methods to approach the exact solution as $\mathrm{N_c} \to \infty$.

7.2.1 Sum-Rule Requirement for cMFTs

For a single sublattice, the lattice G in (7.3) is diagonal in **k**-space, giving $\mathrm{G}(\mathbf{k}) = [-\Sigma(\mathbf{k}) - \beta J(\mathbf{k})]^{-1}$. Denoting translation between two lattice sites by $\mathbf{r}_{ij}$, we have

$$G_{ij} \equiv \frac{1}{V_{\mathrm{BZ}}} \int d\mathbf{k}\ \mathrm{G}(\mathbf{k}) \exp(-i\mathbf{k}\cdot\mathbf{r_{ij}}) \quad , \tag{7.6}$$

with V_{BZ} the volume of the first Brillouin zone (BZ). In cluster methods, the lattice Σ is divided into identical non-overlapping cells with $\mathrm{N_{cell}}$ sites, with non-zero values for site indices belonging to the same cell and zero otherwise, while enforcing consistency between the *lattice* G and the *cluster* $\hat{\mathrm{G}}$. In the limit of $\mathrm{N_c}$=1, Σ contains only diagonal entries; thus, G_{ii} in (7.6) must maintain particle number (7.2b) and concomitantly satisfy the Dyson's relation (7.3), which (for identical sites) becomes

$$G_{ii} = \frac{1}{\Omega_{BZ}} \int \frac{d\mathbf{k}}{-\Sigma_{ii} - \beta J(\mathbf{k})} = 1 - m_i^2 \quad . \tag{7.7}$$

Hence, there is a constraint on Σ_{ii}, as first discussed by Onsager [195] and later Brout [198, 199], which also provides the best initial (diagonal) guess of $\hat{\Sigma}$. More generally, the constraint is on the cluster $\hat{\Sigma}_{ij}$, as initially approximated by Tokar [191]. In what follows we develop a CG-cMFT that appropriately reflects the translational periodicity of the infinite lattice and we invoke cluster self-consistency to improve dramatically the quantitative prediction and convergence with respect to $\mathrm{N_c}$.

7.2.2 Cluster Free Energy

In phase-diagram calculations, free energies must be compared between possible states and entropy S must be added to Eq. (7.4) giving $\mathrm{F} = \bar{\mathrm{E}} - \mathrm{TS}$. With the usual definition of (grand) partition function $\mathrm{Z[A]} = \mathrm{Tr}e^{-\beta \mathrm{H} + A\sigma}$, where A is a source field vector (A_i applied to spin σ_i at site i). For all 2^{N} possible configurations on an N-site lattice, the grand potential is

$$\Omega[\mathrm{A}] \equiv -k_B \mathrm{T} \ln \mathrm{Z[A]} \quad . \tag{7.8}$$

Setting $A = 0$ the free energy is $\mathrm{F} = \Omega[0]$. The one- and two-site state variables m_i and G_{ij} are

$$m_i = \frac{\partial \ln \mathrm{Z[A]}}{\partial A_i}\Big|_{A=0} \;\; ; \;\; G_{ij} = \frac{\partial^2 \ln \mathrm{Z[A]}}{\partial A_i \partial A_j}\Big|_{A=0} \;\; , \tag{7.9}$$

recovering both cases in (7.2). The second variation of $\Omega[A] + A \cdot m$, the variational grand potential, with respect to $\{m_i\}$ [201, 202] recovers (7.3).

Z[A] is exactly solvable for only a few cases. Direct evaluation of Z[A] is often intractable for large N. Thus, in MFTs the partition function of a small $\mathrm{N_c}$-site cluster embedded in the full lattice, $\hat{\mathrm{Z}}$[A], with $2^{\mathrm{N_c}}$ configurations, is evaluated instead. Therefore, only state variables, such as m_i and G_{ij}, whose site indices are in the cluster are configurationally averaged. When $\hat{\mathrm{Z}}$[A] further includes explicit dependence on self-energy (see Section 7.6), any cluster evaluated $\hat{\Sigma}$ or $\hat{\mathrm{G}}$ (from applying (7.9) to $\hat{\mathrm{Z}}$[A]) has to be related consistently with the lattice Σ or G in (7.3), where Σ is divided into periodically repeating cells in coarse-graining techniques. This consistency is key for lattice G to satisfy the sum rule in (7.2b), or the integral (or **k**-space) version in (7.6) or (7.7), all of which can be generalized to multisublattice versions.

7.2.3 Sum-Rule-Conserving Single-Site MFT

As a prelude to the self-consistency relations for general clusters, we summarize the simple improvement for $\mathrm{N_c}$=1 discussed in results. First, we have the cluster $\hat{G}_{ii}$ and $\hat{\Sigma}_{ii}$, obtained from an appropriate cluster partition function [191], $\hat{\mathrm{Z}}$[A] (see Section 7.6), and the lattice G_{ii} and Σ_{ii}. When Σ_{ii}=$\hat{\Sigma}_{ii}$, G($\hat{\Sigma}_{ii}$) from (7.3) is a functional of $\hat{\Sigma}_{ii}$ at fixed T and J. The value of $\hat{\Sigma}_{ii}$ is such that $G_{ii} = \hat{G}_{ii} = 1 - {m_i}^2$, satisfying (7.2b) and (7.7). The cluster free energy $\hat{\mathrm{F}}$ derived from $\hat{\mathrm{Z}}$[A] (see Sec. 7.3.4) is used to determine the AFM phase boundary. We shall call this sum-rule-conserving cMFT, which we show is recovered by general CG in the DCA at $\mathrm{N}_c = 1$. As shown in Fig. 7.1, compared to "exact" lattice Monte Carlo simulations, the sum-rule-conserving cMFT gives the correct topology and good estimates of T_c at consulate points.

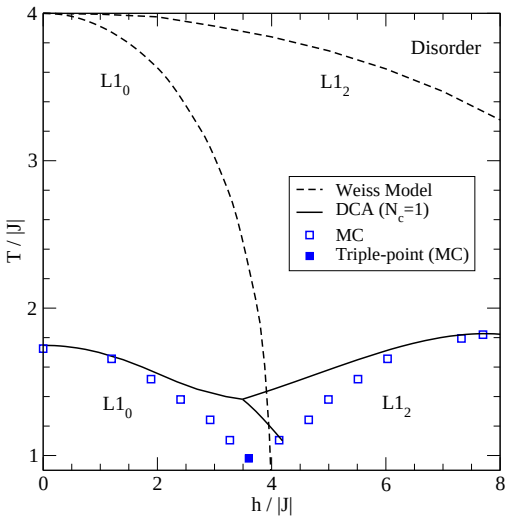

Figure 7.1: T-h boundaries for an FCC AFM. Diagriam is symmetric about h= 0, so only A1, $L1_0$, and $L1_2$ are shown. Results are shown for MC (squares), Weiss [194] (dashed line), and the single-site MFT (solid line) that obeys (7.2b), also recovered via CG-DCA at $N_c = 1$. Obeying (7.2b) improves T_c around stoichometry and gives the correct T-h topology.

7.3 Generalized CG Cluster MFT

For a multisite cluster approximation beyond single-site (N_c>1), the translational invariance of the original lattice is broken and care is needed to relate lattice variables G and Σ from (7.3) to their counterparts $\hat{G}$ and $\hat{\Sigma}$ from the cluster $\hat{Z}$[A]. To our best knowledge, translational invariance and requirements between lattice and cluster variables have not been resolved completely, even though good estimates for the ferromagnetic (FM) T_c had been demonstrated for the classical Ising model [191] for $2 \leq N_c \leq 4$. We use CG methods from DCA/cDMFT to account for cluster translational symmetry in the lattice and to obey (7.2) for $i, j \in$ cluster for G. We show that with a properly defined cluster $\hat{F}$ (see Sec. 7.3.4), reliable estimates for phase boundaries and T_c are obtained using finite clusters, yielding exact results via finite-size scaling as $N_c \to \infty$. Of course, the single-site case is recovered for N_c=1 and provides rapid estimation of phase diagrams, as already suggested by Fig. 7.1. We emphasize that we utilize the CG part from DCA/cDMFT and apply it to the proposed MFT for the Ising model to ensure self-consistency.

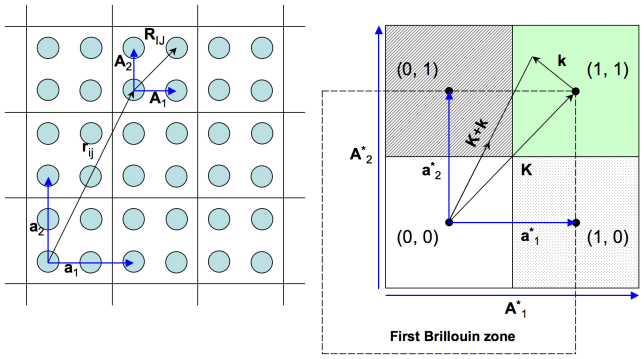

Figure 7.2: Coordinates describing the partition of the lattice into non-overlapping cells, illustrated for N_{cell}=4 on a 2-D square lattice. (left) Real-space translation vectors of the lattice sites and cells are $[\mathbf{A}_1, \mathbf{A}_2]$ and $[\mathbf{a}_1, \mathbf{a}_2]$, respectively, with $\mathbf{R}_{IJ}$ ($\mathbf{r}_{ij}$) the vector between two intra-cluster (inter-cell) sites. (right) Corresponding reciprocal-space translation vectors of the lattice (cells) are $[\mathbf{A}^*_1, \mathbf{A}^*_2]$ ($[\mathbf{a}^*_1, \mathbf{a}^*_2]$). As N_{cell}=4 and the cluster transform is done in a cell, there are 4 cluster momenta, $\mathbf{K}_n$, in the first BZ volume of V_{BZ}, and their positions are generated by $[\mathbf{a}^*_1, \mathbf{a}^*_2]$. The vector $\mathbf{k}$, from the Fourier transform of inter-cell coordinates, is quasi-continuous at large N and are assigned to CG (shaded) regions with volume $V_{\tilde{\Delta}}$=V_{BZ}/N_{cell}.

7.3.1 CG Methods from cDMFT and DCA

To distinguish between lattice and cluster variables, we refer to each partition of the lattice self-energy as 'cell' (instead of cluster). To begin, the lattice self-energy is partitioned into non-overlapping cells, $\tilde{\Sigma}$, containing N_{cell} lattice sites, where $N_{cell} \geq N_c$, where, again, N_c is the number of cluster sites considered in $\hat{Z}$[A]. Hence,

$$\Sigma_{(i,I)(j,J)} = \tilde{\Sigma}_{IJ}\delta_{ij} \quad , \tag{7.10}$$

where the double-index denotes a site (out of a total of N sites) in the lattice, with uppercase $I(J)$ denote sites within each cell $i(j)$.

Assuming identical cells, one can carry out an inter-cell Fourier transform on the lattice variables (see Fig. 7.2) using vectors $[\mathbf{a}_1, \mathbf{a}_2, \mathbf{a}_3]$, as opposed to translation vectors of the lattice $[\mathbf{A}_1, \mathbf{A}_2, \mathbf{A}_3]$. For a given lattice variable, X,

$$X_{IJ}(\mathbf{k}) = \frac{N_{cell}}{N} \sum_{i,j} X_{(i,I)(j,J)} e^{i\mathbf{k}\cdot\mathbf{r_{ij}}} \quad , \tag{7.11}$$

where $\mathrm{N}/\mathrm{N}_{\mathrm{cell}}$ is the total number of cells and the displacement between cell i and j is given by $\mathbf{r}_{ij}$, where $\mathbf{r}_{ij} = n_1\mathbf{a}_1 + n_2\mathbf{a}_2 + n_3\mathbf{a}_3$ with n_i being integers. Applying the inter-cell Fourier transform to (7.3),

$$G_{IJ}^{-1}(\mathbf{k}) = -\tilde{\Sigma}_{IJ} - \beta J_{IJ}(\mathbf{k}) \quad , \tag{7.12}$$

where the terms are entries to $\mathrm{N}_{\mathrm{cell}} \times \mathrm{N}_{\mathrm{cell}}$ symmetric matrices and $\tilde{\Sigma}_{IJ}$ is independent of $\mathbf{k}$. With no further assumptions (other than matrices are symmetric), $\tilde{\Sigma}$ will have $\mathrm{N}_{\mathrm{cell}}(\mathrm{N}_{\mathrm{cell}} - 1)/2$ independent entries and a violation of translational invariance within the cell is possible.

Translational invariance: If a given lattice variable is further required to be translational invariant within the cell, as in the DCA [185], X_{IJ} is diagonal in the $\mathbf{k}$-space of the cell. Via the cluster transform

$$X(\mathbf{K}_n) = \frac{1}{\mathrm{N}_{\mathrm{cell}}} \sum_{IJ}^{\mathrm{N}_{\mathrm{cell}}} X_{IJ} e^{i\mathbf{K}_n \cdot \mathbf{R}_{IJ}} \quad , \tag{7.13}$$

where $\mathbf{K}_n$ are the $\mathrm{N}_{\mathrm{cell}}$ cluster momenta in the BZ (illustrated in Fig. 7.2) and $\mathbf{R}_{IJ}$ is the displacement between sites I and J within the cell. The summation in (7.13) is restricted to sites within the cell. The $\mathbf{K}_n$ are points in $\mathbf{k}$-space produced by the reciprocal vectors of the cell $[\mathbf{a}_1^*, \mathbf{a}_2^*, \mathbf{a}_3^*]$, where $\mathbf{a}_i \cdot \mathbf{a}_j^* = 2\pi\delta_{ij}$ and there are $\mathrm{N}_{\mathrm{cell}}$ of them in the BZ [185,188,203]. The inverse cluster transform is

$$X_{IJ} = \frac{1}{\mathrm{N}_{\mathrm{cell}}} \sum_{\mathbf{K}_n \in \mathrm{BZ}}^{\mathrm{N}_{\mathrm{cell}}} X(\mathbf{K}_n) e^{-i\mathbf{K}_n \cdot \mathbf{R}_{IJ}} \quad . \tag{7.14}$$

X_{IJ} is translational invariance only if both (7.13) and (7.14) holds, implying that X_{IJ} is only dependent on the displacement between the cluster sites $\mathbf{R}_{IJ}$. Therefore one could do the cluster transform in (7.13) based on any site in the cluster (translational invariance), leading to $\mathrm{N}_{\mathrm{cell}}$ independent entries.

However, $J_{IJ}(\mathbf{k})$, known *a priori* from the H in (7.1), is not translational invariant for a general cluster. The inter-cell Fourier transform in (7.11) results in the dependence on 2

indices, I and J, or, equivalently, I and $I-J$, making it site-dependent. Considering NN interaction, a central site in a large (enough) cluster will not incur a phase factor (as all interactions are contained in the cluster) during the inter-cell Fourier transform, but a site at the perimeter of the cell has a phase factor via interaction with a site from an adjacent cell; hence, $J_{IJ}(\mathbf{k})$ is site-dependent. To ensure translational invariance in the solution of $G_{IJ}(\mathbf{k})$ and $\tilde{\Sigma}_{IJ}$, we multiply $J_{IJ}(\mathbf{k})$ by the phase $\exp(i\mathbf{k}\cdot\mathbf{R}_{IJ})$, as is done in the **r**-space version of DCA (see appendix A in [184]), resulting in the relation

$$G_{IJ}^{-1}(\mathbf{k}) = -\tilde{\Sigma}_{IJ} - \beta J_{IJ}(\mathbf{k}) e^{i\mathbf{k}\cdot\mathbf{R}_{IJ}} \quad . \tag{7.15}$$

r-space CG: From G_{IJ} a coarse-grained $\bar{G}_{IJ}$ is obtained via

$$\bar{G}_{IJ} = \frac{\mathrm{N_{cell}}}{\mathrm{N}} \sum_{\mathbf{k}\in \mathrm{BZ'}} G_{IJ}(\mathbf{k}) e^{-i\mathbf{k}\cdot\mathbf{r}_{ij}} \quad . \tag{7.16}$$

For $\mathbf{r}_{ij}$=0, when only sites from the same cell are of interest, the procedure is exactly analogous to that used in cDMFT or DCA, when (7.12) or (7.15) are coarse-grained, respectively; the cell Brillouin zone, BZ', is $1/\mathrm{N_{cell}}$ of the lattice BZ. The r-space formulation allows for the representation of any general ordered phases with multiple sublattices [184].

k-space CG: For cases with one sublattice, i.e., paramagnetic or ferromagnetic phases, the solution from DCA is diagonal in **k**-space. Applying the cluster transformation [185], shown in (7.13), to (7.15) yields

$$G(\mathbf{k}+\mathbf{K}_n) = \left[-\tilde{\Sigma}(\mathbf{K}_n) - \beta J(\mathbf{k}+\mathbf{K}_n)\right]^{-1} \quad , \tag{7.17}$$

where $J(\mathbf{k}+\mathbf{K}_n)$ is equivalent to the lattice Fourier transform of J. The result, $\mathrm{G}(\mathbf{k}+\mathbf{K}_n)$, is further coarse-grained about $\mathbf{K}_n$ as

$$\bar{G}(\mathbf{K}_n) = \frac{\mathrm{N_{cell}}}{\mathrm{N}} \sum_{\mathbf{k}\in\bar{\Delta}(\mathbf{K}_n)} G(\mathbf{k}+\mathbf{K}_n) \quad , \tag{7.18}$$

where the summation is over a zone, $\bar{\Delta}(\mathbf{K})$ (a parallelogram in 2-D, a parallelepiped in

3-D), centered at $\mathbf{K}_n$, whose volume is $V_{\bar{\Delta}} = V_{\rm BZ}/{\rm N}_{\rm cell}$, see Fig. 7.2. Equation (7.18) in integral form for an infinite lattice ($\mathrm{N} \to \infty$) is

$$\bar{G}(\mathbf{K}_n) = \frac{1}{V_{\bar{\Delta}}} \int_{\mathbf{K}_n - \frac{1}{2}\Delta}^{\mathbf{K}_n + \frac{1}{2}\Delta} d\mathbf{k}\; G(\mathbf{k} + \mathbf{K}_n) \quad , \tag{7.19}$$

where the integral is over the same zone centered at $\mathbf{K}_n$ and defined by $\mathbf{K}_n \pm \frac{1}{2}\Delta$ with volume $V_{\bar{\Delta}}$. For DCA, r-space CG $\bar{G}_{IJ}$ is related to $\bar{G}(\mathbf{K}_n)$ via a cluster transform,

$$\bar{G}_{IJ} = \frac{1}{{\rm N}_{\rm cell}} \sum_{\mathbf{K}_n \in {\rm BZ}}^{{\rm N}_{\rm cell}} \bar{G}(\mathbf{K}_n) e^{-i\mathbf{K}_n \cdot \mathbf{R}_{IJ}} \quad . \tag{7.20}$$

7.3.2 Self-Consistent Embedded Cluster Solver

A connection has to be made between the lattice variables (divided into cells) and the cluster variables evaluated via the cluster $\hat{\mathrm{Z}}[A]$, see (7.48) and (7.47),

$$\hat{G}_{ij} = \frac{{\rm Tr}_{\sigma \in c} \sigma_i \sigma_j e^{\hat{H}(\hat{\mathcal{G}}^{-1},\ \beta m J,\ \sigma)}}{{\rm Tr}_{\sigma \in c} e^{\hat{H}(\hat{\mathcal{G}}^{-1},\ \beta m J,\ \sigma)}} \quad , \tag{7.21}$$

where the trace is over sites within the cluster and $\hat{\mathrm{Z}}[A = 0]$ is the denominator. The cluster Hamiltonian, $\hat{H}$, consists of the "dressed" effective interactions between sites in the cluster,

$$\hat{\mathcal{G}}^{-1} = \hat{G}^{-1} + \hat{\Sigma} \quad , \tag{7.22}$$

and the mean-field, mJ, for coupling to sites exterior to the cluster. For comparison with DCA/cDMFT (see Fig. 6 in [185]), Fig. 7.3 shows a self-consistency loop for the general case when ${\rm N}_{\rm cell} \geq {\rm N}_c$. A chosen CG method (Eq. (7.16) for r-space or (7.18) for k-space) is used in conjunction with the cluster solver in (7.21).

1. Starting from an initial value for $\tilde{\Sigma}$, $\bar{G}$ is evaluated from the CG equation of choice.
2. $\bar{G}$ is projected to the space of the cluster via a N_c-by-$\mathrm{N}_{\rm cell}$ projection matrix P_c.
3. An effective interaction $\mathcal{G}^{-1}$ is calculated and used in the cluster solver.
4. $\hat{G}$, evaluated via the cluster solver is used to obtain a new $P_c \tilde{\Sigma} P_c'$.

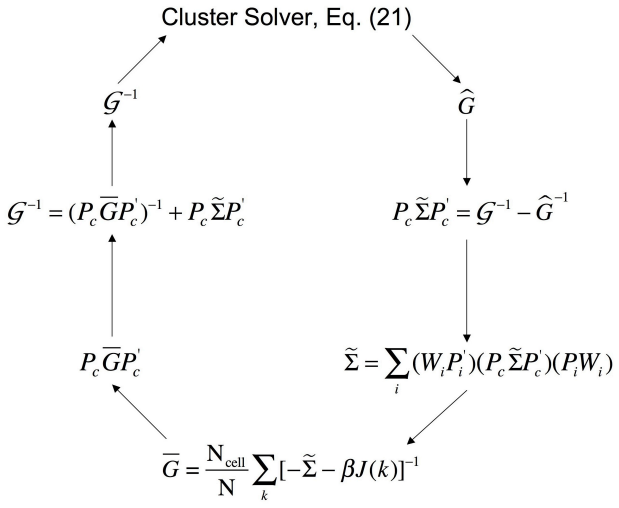

Figure 7.3: Sketch of a self-consistent algorithm for solving the cMFT problem, in the general case of $N_{\text{cell}} \geq N_c$, see Section 7.3.2 for description.

5. Lattice $\tilde{\Sigma}$ is obtained by appropriately 'tiling' an N_{cell}-by-N_{cell} matrix with $P_c \tilde{\Sigma} P_c'$. Mathematically, this is accomplished by a set of projection vectors P_i, which are weighed appropriately by a diagonal matrix, W_i, to prevent over-counting.

6. Steps 1 to 5 are repeated until $\tilde{\Sigma}$ converges to a solution.

We note that upon convergence,

$$\hat{\Sigma} = P_c \tilde{\Sigma} P_c' \quad , \tag{7.23}$$

$$\hat{G} = P_c \tilde{G} P_c' \quad . \tag{7.24}$$

Importantly, we note that for N_{cell}>N_c, only some of the components in $\bar{G}$ are used in the cluster solver. In addition, there may exist one-to-many relation going from $\hat{\Sigma}$ to $\tilde{\Sigma}$, depending on the relation

$$\tilde{\Sigma} = \sum_i (W_i P_i') \hat{\Sigma} (P_i W_i) \quad . \tag{7.25}$$

However, in the case where N_{cell}=N_c, $\hat{\Sigma} = \tilde{\Sigma}$, $\hat{G} = \tilde{G}$ and the projection matrix is the N_c-by-N_c identity matrix, i.e., $P_i = W_i = I$, resulting in a self-consistency scheme that is exactly analogous to that used in DCA and cDMFT. We note that this consistency

relation is enforced for sites belonging to the same projected cluster space, which does not preclude the calculation of G_{IJ} between sites of different clusters via (7.16) with non-zero $\mathbf{r}_{ij}$. Importantly, we have shown how the cluster variables from $\hat{\mathrm{Z}}[\mathrm{A}]$ are related to the CG lattice variables, allowing us to solve a system of coupled equations.

7.3.3 Solving for Cluster $\hat{\mathrm{G}}$ and $\hat{\Sigma}$

To obtain the cluster $\hat{\mathrm{F}}$, the $\hat{\Sigma}$ and $\hat{\mathrm{G}}$ have to be evaluated. Although one can utilize the iterative scheme in Fig. 7.3, we solved the appropriate equations simultaneously using the '*fsolve*' function in MATLAB [204]. Assuming only that the cluster matrices are symmetric, the number of independent elements of $\hat{\Sigma}$ is

$$M_v = \mathrm{N_c} + \frac{\mathrm{N_c}(\mathrm{N_c}-1)}{2}. \tag{7.26}$$

Hence, with both $\hat{\Sigma}$ and $\hat{G}$, we have $2M_v$ independent variables. From the cluster partition function $\hat{\mathrm{Z}}[\mathrm{A}]$, there are $\mathrm{N_c}$ equations for the m_i (or equivalently, $\hat{G}_{ii}$) and $\mathrm{N_c}(\mathrm{N_c}-1)/2$ equations for the $\hat{G}_{ij}$ (see (7.48)), giving us M_v independent self-consistent equations.

On the other hand, from the cell-partitioning of the Dyson's relation, we use M_v equations from (7.16) that relates the projected part, $P_c\bar{G}P_c'$, to the lattice self-energy $\tilde{\Sigma}$. Combining with those from the cluster approximation, we have $2M_v$ independent equations to solve for the $2M_v$ unknown cluster variables, $\hat{\Sigma}$ and $\hat{\mathrm{G}}$. The lattice variables are dependent variables because their exact mapping to the cluster variables is given by Eqs. (7.24) and (7.25).

Even though our code had not been fully optimized, we find that the method is especially fast when N_c is small ($\mathrm{N}_c < 10$). Use of DCA CG further reduces M_v via the appropriate treatment of translational invariance, where cluster sites belonging to the same sublattice are made equivalent. In the case of FM Ising model, $M_v = \mathrm{N_c}$, speeding up calculations. At second-order FM T_c, the uniform susceptibility $\beta G(\mathbf{K}_n{=}0,\mathbf{k}{=}0)$ diverges, i.e., from (7.17) we have

$$\tilde{\Sigma}(\mathbf{K}_n = 0) + \beta_c J(0) = 0 \tag{7.27}$$

as an extra constraint for determining β_c at criticality.

7.3.4 The Cluster Free Energy

With $\hat{\mathrm{G}}$ and $\hat{\Sigma}$ obtained via DCA CG method, we require the cluster free energy for constructing boundaries between different phases. Via Tokar's field-theory cluster formalism [191] and the definition of pair-correlation energy (7.5), we are able to express the cluster free energy $\hat{\mathrm{F}}$ as

$$\hat{\mathrm{F}} = \mathrm{E}_1 + \hat{\mathrm{E}}_2 - \mathrm{T}\sum_{\mathrm{c}} \hat{\mathrm{S}} - \frac{k_B \mathrm{T}}{2}\left[\ln\det\,\mathrm{G} - \sum_{\mathrm{c}} \ln\det\,\hat{G}\right] \quad . \tag{7.28}$$

Here "c" denotes independent clusters in the lattice and $\hat{\mathrm{S}}$ is the cluster entropy, which reduces to point entropy for $\mathrm{N_c}$=1. The last term gives the Gaussian part of the pair correlations in the lattice relative to those in the cluster (see Section 7.6), where, for $\mathrm{N_c} = \infty$ the free energy is exact and the term in brackets is zero.

7.4 Results and Discussion

We apply cluster methods from various cluster-lattice Fourier transforms to the FM and AFM Ising model (with nearest-neighbor (NN) interactions only) on 1-D and 3-D (FCC) lattices. We discuss results from the DCA (i.e., $\mathrm{N_{cell}} = \mathrm{N_c}$), giving a one-to-one mapping of the cluster variables to the lattice cell variables. We also discuss results with $\mathrm{N_{cell}} > \mathrm{N_c}$ scheme, with $\mathrm{N_{cell}} = \infty$ being the NCG version, which do not exhibit the one-to-one mapping and do not preserve translational invariance but does conserve the sum rules and provide accurate estimates of thermodynamics. We first show the improvement for the estimation of T_c for $\mathrm{N_c}$=1. Then, we discuss DCA results for multisite clusters in various lattices, including finite-size scaling of T_c versus $\mathrm{N_c}$ for the FCC FM and AFM (including tricritical points) that yield exact values at $\mathrm{N_c} \to \infty$. Lastly, we compare results obtained by the DCA and NCG scheme. The NCG version converges thermodynamic quantities

more rapidly versus N_c using significantly less computational time.

7.4.1 Weiss Single-Site MFT

The consistency between $\hat{G}$ estimated from $\hat{Z}[A]$ and G obtained from Dyson's equation is ignored in textbook MFTs (e.g., Weiss, Bethe [83], quasichemical method [205]), where $\hat{Z}[A]$ is formulated without proper treatment of Σ; G_{ii} evaluated via (7.7) violates (7.2b). In the Weiss model [193], spin correlations are completely neglected, as in a disordered phase. With $c_i^{\pm} \equiv (1 \pm m_i)/2$, the free energy is obtained by including the point entropy S_1, i.e.,

$$F_1 = E_1 - T\left[-k_B \sum_i \left(c_i^+ \ln\ c_i^+ + c_i^- \ln\ c_i^-\right)\right] \quad . \tag{7.29}$$

The functional F_1 is minimized with respect to m_i or via (7.9) to obtain m_i from the coupled set of equations

$$m_i = \tanh\left[\beta \sum_j J_{ij} m_j + \beta h\right] \quad . \tag{7.30}$$

Equation (7.30) gives the Weiss result [193,194] and is frequently used to illustrate phase transitions. However, it gives poor quantitative estimates of T_c and phase boundary topology. For the zero-field case, the Weiss model incorrectly predicts FM ordering at $T_c = zJ$ (instead of T_c=0) for the 1-D lattice where z=2. The Weiss model is only correct [31] in the limit of infinite dimensions or at finite dimension for infinite-ranged J's. Estimates are improved with MFTs that extend beyond single-site, such as the Bethe [83] and quasichemical methods [205]. For example, the Bethe approximation correctly predicts the 1-D FM T_c to be zero [85] and improves estimates of T_c at higher dimensions. However, the inaccuracies are exacerbated when describing transitions for frustrated lattices. For AFM on an FCC lattice, the Weiss model fails to predict even qualitatively the correct topology given by MC, see Fig. 7.1. Although the quasichemical methods somewhat improve the topology, the boundary approaches T=0 incorrectly [145, 206].

In the Krivoglaz, Clapp, and Moss (KCM) approximation for the self-energy [207, 208] of the Weiss model

$$\Sigma_{ij}^{KCM} = -\delta_{ij}(1 - m_i^2)^{-1} \quad . \tag{7.31}$$

When (7.31) is substituted into (7.7) it does not satisfy the sum rule [201, 202] in (7.2b), i.e., the Weiss model simply solves the approximate partition function via (7.30) regardless of the value of lattice G_{ii} from (7.7). Thus, to satisfy the sum rule, Σ_{ii} must be "adjusted" such that the resulting value of G_{ii} in (7.7) coincide with that obtained from (7.9) for an approximated Z[A], which satisfies (7.2b) by construction, as is done by Onsager's cavity field theory [195–197] and Brout's spherical model [198, 199, 209]. Results for G via (7.3) can be improved progressively as the approximation for Σ becomes more sophisticated, e.g., the Gamma-Expansion Method (GEM) [190] that includes off-diagonal entries, or the Ring approximation that includes infinite sums of subsets of a diagrammatic expansion [210].

7.4.2 An Accurate Single-Site DCA-like Theory

Estimate of phase transitions for the single-site case is improved via a DCA-like approach. At $\mathrm{N_c} = 1$, applying (7.9) to the cluster $\hat{\mathrm{Z}}$[A] [191], see (7.48), we obtain the better magnetization equation

$$m_i = \tanh\left[\left(\hat{G}_{ii}^{-1} + \Sigma_{ii}\right) m_i + \beta \sum_j J_{ij} m_j + \beta h\right] \tag{7.32}$$

and $\hat{G}_{ii} = 1 - m_i^2$, which has the obvious on-site correction from the sum-rule, c.f. (7.30). We can also derive (7.32) by minimizing (7.28) with respect to m_i, or from (7.1) assuming that J_{ii} is non-zero such that (7.3) is obeyed. This result was also found by Tokar and Tsatskiis [211] by assuming CPA-like embedding and ignoring boundary effects. Thus, for $\mathrm{N_c} = 1$, $\hat{\mathrm{F}}$ in (7.28) simplifies to

$$\mathrm{E}_2 = \frac{k_B \mathrm{T}}{2} \sum_i (1 + \hat{G}_{ii}\hat{\Sigma}_{ii}) \tag{7.33a}$$

$$\sum_{\mathrm{c}} \ln\det\, \hat{G} = \sum_i \ln \hat{G}_{ii} \tag{7.33b}$$

$$\ln\det\, \mathrm{G} = -\frac{\mathrm{N}}{V_{BZ}} \int_{\mathrm{BZ}} d\mathbf{k}\ \ln\left(-\Sigma_{ii} - \beta J(\mathbf{k})\right) \tag{7.33c}$$

and $\sum_i \hat{\mathrm{S}}$ becomes the point entropy S_1. Note that (7.33c) is valid only for single sublattice phases.

To relate correctly the cluster and lattice variables, the $\mathrm{N_c}$=1 DCA sets $\tilde{\Sigma}_{ii} = \hat{\Sigma}_{ii}$ and (7.20) simplifies to (7.7), i.e., $\hat{G}_{ii}$=G_{ii}, satisfying (7.2b). Together with (7.32), we have a coupled set of equations for estimating thermodynamic state variables for the Ising model for a given T and h, utilizing (7.28) with (7.33) to obtain free energies.

First-order AFM ($J = -1$) on FCC Lattice

The free energies of the $\mathrm{L1_0}$ and $\mathrm{L1_2}$ ordered groundstates are compared with the high-T disordered A1 phase, allowing construction of the phase diagram. In Fig. 7.1, the T-h phase diagram for the FCC Ising model obtained via DCA $\mathrm{N_c}$=1 (i.e., (7.2b), (7.7) and (7.32)) is compared with that of the Weiss model [194] and MC (exact). The DCA $\mathrm{N_c}$=1 gives good estimate of the topology from MC, although the tricritical-point temperature is higher compared to MC. Nonetheless, the results are a huge improvement over the the Weiss model, in which the phase boundaries are not even qualitatively close to the exact topology. We emphasize that this results from including self-correlation to the single-site Weiss magnetization, as shown in (7.32).

Second-order FM ($J = 1$) at $h = 0$

Above T_c, (7.32) is automatically satisfied by m_i=0 for all sites, i.e., the paramagnetic state. For a second-order transition, the uniform susceptibility $\beta G(\mathbf{k} = 0)$ diverges at T_c [85]. The denominator of the integrand in (7.7) is thus zero at $\mathbf{k}$=0, i.e., $\Sigma_{ii} = -\beta_c J(\mathbf{k} = 0)$, giving

$$G_{ii} = \frac{1}{\Omega \beta_c J(0)} \int \frac{d\mathbf{k}}{1 - J(\mathbf{k})/J(0)} \quad . \tag{7.34}$$

With G_{ii}=1 (given m_i=0), only β_c must be determined. Although the integrand contains a singularity at $\mathbf{k}$=0, the integral (a lattice Green's function [212]) is convergent [213] for cubic lattices and the numerical values are given in [209]. We have obtained them via numerical integration using MATLAB [204]. In the 1-D case, the integral is divergent, requiring $\beta_c \to \infty$ for G_{ii} to be finite, so the cluster method yields the correct result of $\mathrm{T}_c = 0$ in 1-D.

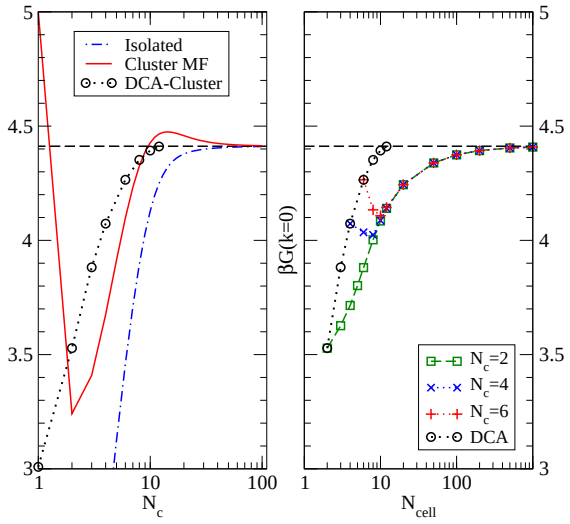

(a) (b)

Figure 7.4: (color online) 1-D FM uniform lattice susceptibility (ULS) for $J = 1$ and at $T = 1.2$ versus (a) N_c and (b) N_{cell}, with exact value at $N_c = \infty$ given by the horizontal (dashed) line. (a) DCA-like ($N_{cell} = N_c$) results are compared with that from the isolated cluster and Cluster MF [185]. (b) Our cMFTs for $N_{cell} > N_c$ ULS vs. N_{cell} is shown for N_c of 2, 4 and 6, yielding the exact result at $N_{cell} \approx 1000$; all results collapse on a single curve for $N_{cell} \gtrsim 2N_c$. DCA-like results are shown (circles joined by dotted line) for comparison.

For the FM FCC case, T_c is only 8.9% lower than the exact result, a significant improvement over the Weiss model (22.5% higher), while retaining the mathematical simplicity. Thus DCA N_c=1 result is equivalent to that found by Tokar [191].

7.4.3 Multisite Cluster CG Theory

FM on 1-D Lattice

For the 1-D chain, we now study the effect of obeying the sum rule in (7.2b) for general cluster sizes. The uniform lattice susceptibilities (ULS), $\beta G(\mathbf{K}_n{=}0,\ \mathbf{k}{=}0)$, at J=1 and T=1.2, obtained by the DCA and Weiss-like MFT are compared in Fig. 7.4(a). The isolated (finite-size) cluster approximation (see (13) in [185]) only takes into account interactions between atoms in an isolated, finite-size cluster whose partition function is calculated via the transfer-matrix method. The Cluster MF approximation (see (14) in [185]) further adds in mean-field contribution to the cluster, with the Weiss model being the single-site Cluster

MF. Both isolated cluster and Cluster MF approximations do not require the lattice G to satisfy (7.2b).

Improvements in accuracy is apparent especially at low cluster size ($N_c < 8$). At fixed N_c cluster size, the inclusion of MFT corrections improve the estimate of ULS (c.f., isolated cluster and Cluster MF methods) and is further improved upon by taking into account of the intensity sum rule (c.f., Cluster MF and DCA). In addition, while DCA MFT shows a monotonic convergence (from below) to the exact value versus N_c, the Cluster MF estimate overshoots the exact value at $N_c = 9$ resulting in a temporary lost in accuracy.

FM on FCC Lattice with Finite-size Scaling

The DCA MFT exhibits finite-size scaling for T_c versus N_c, as we show in Fig. 7.5 using Bett's clusters [192] with $15 \leq N_c \leq 24$ (values are tabulated in Table 7.2). T_c are plotted along with the finite-size scaling law,

$$\|T_c^{\mathrm{DCA}} - T_c^{\mathrm{exact}}\|^{-\nu} \sim L = N_c^{1/3} \quad , \tag{7.35}$$

where $0.625 \lesssim \nu \lesssim 0.63$ for 3-D Ising universality class [214, 215]. We use $\nu = 0.625$, although our findings are not affected by other choices in the range. The scaling curve is extrapolated to $N_c = \infty$, giving a value of $T_c/12J = 0.813$, close to the MC exact result of 0.8167.

AFM on FCC Lattice with Finite-Size Scaling

For the AFM, multiple sublattices are used to describe the $L1_0$ and $L1_2$ states, which exhibit frustration. As a result, the real-space DCA is used, see (7.15) and (7.16). In Fig. 7.6, phase boundaries from single-site DCA (already shown in Fig. 7.1) are compared with those from DCA and cDMFT multisite clusters with N_c=4 or 16 and exact results from MC. Because the single-site estimates of T_c near stoichiometry are already excellent, the improvement with increased cluster size is minor at $h/|J|$=0 and $h/|J| \simeq 7.7$, where only two phases compete. However, at the tricrtical point, T_t, where the three phases ($L1_0$, $L1_2$ and A1) coexist, there is a significant improvement. As N_c increases, T_t progressively

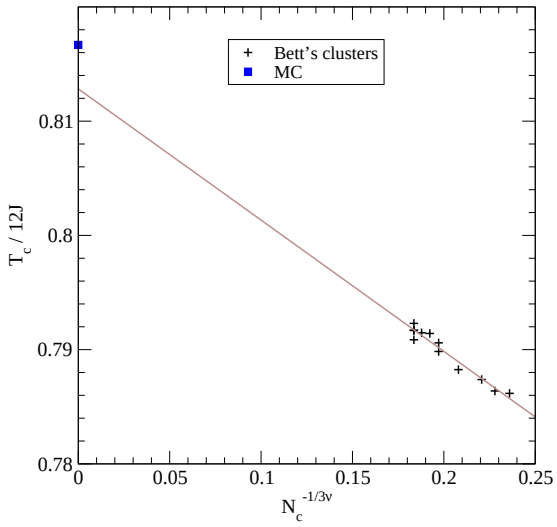

Figure 7.5: (color online) Finite-size scaling (7.35) for FCC FM Ising model with $\nu = 0.625$. The line is a linear fit to T_c^{DCA} using Bett's clusters ('+') for $15 \leq N_c \leq 24$. $T_c/12J = 0.813$ for $N_c = \infty$ compared to 0.8167 from MC (square).

decreases and approaches the MC value of $T_t/|J| \simeq 1$.

A fit to the finite-size scaling (7.35) for T_t using N_c=4 and 16 DCA is shown in Fig. 7.7. Although ideally one would prefer to include larger clusters for scaling, the calculations are computationally expensive for N_c>4 clusters, especially with the multiple sublattices involved, in which case exact MC simulations must be preferred. Nevertheless, the extrapolated result at N_c=∞ ($T_t/|J|$=0.98) is within the error bars of MC data.

7.4.4 NCG versus CG cMFT

To facilitate comparison with other methods, we discuss here the case of $N_{cell} > N_c$, i.e., $\tilde{\Sigma}$ and $\hat{\Sigma}$ are of different sizes. The connection is made via the following

$$\tilde{\Sigma}_{\tilde{I}\tilde{J}} = \begin{cases} \hat{\Sigma}_{IJ} & \text{if } |\mathbf{R}_{\tilde{I}\tilde{J}}| = |\mathbf{R}_{IJ}| \\ 0 & \text{otherwise} \quad , \end{cases} \tag{7.36}$$

i.e., terms belonging to the same nearest-neighbor (NN) distance are equal. For example, the unique NN term $\hat{\Sigma}$ (a 2×2 matrix) is assigned to all NN entries in $\tilde{\Sigma}$ with all entries beyond NN set to zero. The relation in (7.36) can also be achieved via Eq. (7.25), using an appropriately weighed set of projection matrices.

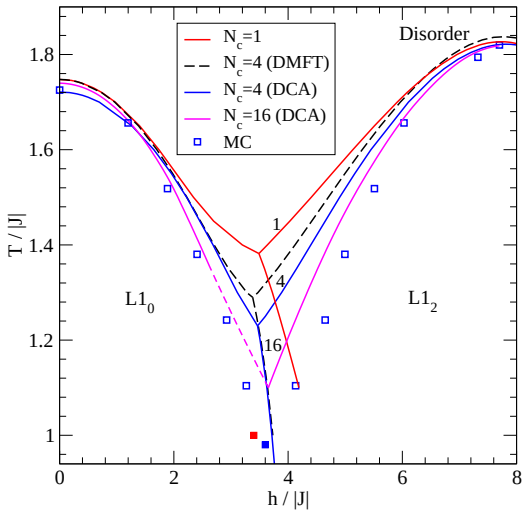

Figure 7.6: (color online) $T-h$ boundaries for FCC AFM, showing A1, $L1_0$ and $L1_2$ phases. CG boundaries for DCA-like $N_c = N_{cell} = 1,\ 4,$ and 16 are labelled, along with cDMFT-like with $N_c = 4$. MC results are marked by squares (unfilled are ours, and filled are tricritical points from [140] and [216]). For $N_c = 16$ DCA, the A1-$L1_0$ boundary below $T/|J|$=1.35 is extrapolated due to poor numerical convergence. The tricritical point approaches the MC result as N_c increases.

To further illustrate this point, we consider the 1-D lattice using a $N_c = 3$ cluster, see Fig. 7.8 (top row). The cluster self-energy is given by

$$\hat{\Sigma} = \begin{bmatrix} s_{11} & s_{12} & s_{13} \\ s_{12} & s_{11} & s_{12} \\ s_{13} & s_{12} & s_{11} \end{bmatrix} , \tag{7.37}$$

where the diagonal terms are equal in the FM case, and the off-diagonal terms are labelled by the separation in the cluster; s_{12} for NN and s_{13} for the next NN (NNN). The assignment to the lattice $\tilde{\Sigma}$ is made via (7.36) and is illustrated in Fig. 7.8 for N_{cell} equal to 3, 4 and ∞. For the DCA, the lattice self-energy is partitioned such that $\tilde{\Sigma}$ for each cell is exactly $\hat{\Sigma}$. We see that the matrix in (7.37) is translational invariant when $s_{12} = s_{13}$. This is possible by virtue of the cluster transforms (7.13) and (7.14), where cluster periodicity requires that the NNN term between sites 1 and 3 in the same cell (see Fig. 7.8 top row) to be the same as the NN term between site 1 (same cell) and site 3 in the left adjacent cell.

Furthermore, Fig. 7.8 shows that the off-diagonal terms are assigned at a higher frequency throughout the lattice when N_{cell} increases. In the case of $N_{cell} = 4$ (middle row of

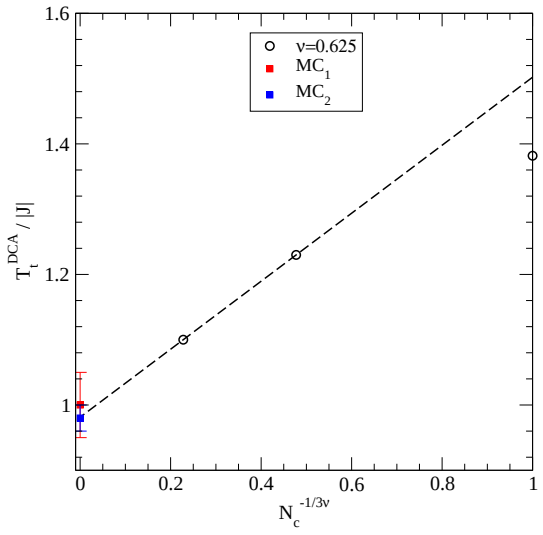

Figure 7.7: (color online) Finite-size scaling (7.35) for tricritical point T_t in Fig. 7.6 for FCC AFM for N_c=1, 4, and 16 DCA (open circles). The dashed line is a fit to $N_{cell} = N_c =$ 4 and 16. The T_t at N_c=∞ is within the error bars of MC data [140] (red/top square) and [216] (blue/bottom square).

Fig. 7.8), the self-energy of the cell is

$$\tilde{\Sigma} = \begin{bmatrix} s_{11} & s_{12} & s_{13} & 0 \\ s_{12} & s_{11} & s_{12} & s_{13} \\ s_{13} & s_{12} & s_{11} & s_{12} \\ 0 & s_{13} & s_{12} & s_{11} \end{bmatrix} , \tag{7.38}$$

and we see that the apparent NNN term between sites 2 and 4 remains NNN even if one of the sites is shifted to an adjacent cell by cluster periodicity. $\tilde{\Sigma}$ is thus site-dependent and, therefore, not translational invariant.

Once $\tilde{\Sigma}$ is assigned, one can follow the steps laid out in 7.3.1 to obtain the CG $\bar{G}$. Using the k-space formulation for illustration, with non-coarse-graining method (NCG), where $N_{cell} = N \to \infty$, Eq. (7.19) is reduced to

$$\begin{aligned} \bar{G}(\mathbf{K}_n) &= \lim_{V_{\bar{\Delta}} \to 0} \frac{1}{V_{\bar{\Delta}}} \int_{\mathbf{K}_n - \frac{1}{2}\Delta}^{\mathbf{K}_n + \frac{1}{2}\Delta} d\mathbf{k}\; G(\mathbf{k} + \mathbf{K}_n) \\ &= \frac{G(\mathbf{K}_n) \times V_{\bar{\Delta}}}{V_{\bar{\Delta}}} = G(\mathbf{K}_n) \quad . \end{aligned} \tag{7.39}$$

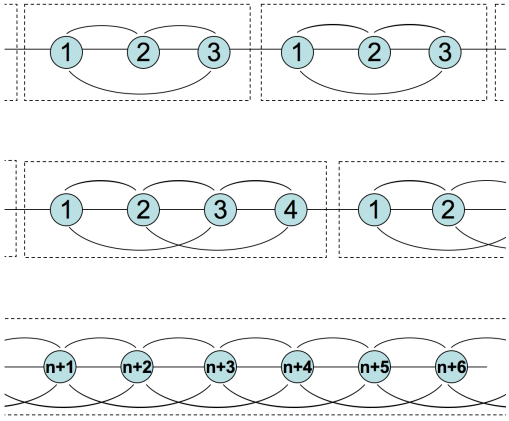

Figure 7.8: Partitioning of the lattice $\tilde{\Sigma}$ into cells with $\mathrm{N_{cell}}$ equal to 3 (top), 4 (middle) and ∞ (bottom). For $\mathrm{N}_c = 3$, the top (bottom) row corresponds to the CG (NCG) scheme. For each row, the upper and lower arrays of connectors represents the NN and NNN self-energy term, respectively. Connectors are missing between cells except for $\mathrm{N_{cell}} = \infty$ case (bottom).

Substituting into Eq. (7.20) we have,

$$\begin{aligned}
\bar{G}_{IJ} &= \lim_{N_{\mathrm{cell}}\to\infty} \frac{1}{N_{\mathrm{cell}}} \sum_{\mathbf{K_n}\in \mathrm{BZ}}^{N_{\mathrm{cell}}} G(\mathbf{K}_n) e^{-i\mathbf{K}_n\cdot\mathbf{R}_{IJ}} \\
&= \frac{1}{V_{\mathrm{BZ}}} \int_{\mathrm{BZ}} d\mathbf{K}\; G(\mathbf{K}) e^{-i\mathbf{K}\cdot\mathbf{R}_{IJ}} \qquad (7.40) \\
&= \frac{1}{V_{\mathrm{BZ}}} \int_{\mathrm{BZ}} d\mathbf{K}\; \left[-\tilde{\Sigma}(\mathbf{K}) - \beta J(\mathbf{K})\right]^{-1} \quad . \qquad (7.41)
\end{aligned}$$

$\bar{\mathrm{G}}$ is thus obtained via a Fourier transform, i.e., no coarse-graining is used. This result was used by Tokar [191] by ignoring the difference between cluster-lattice transforms of matrices J and Σ due to phase factors at the cell boundaries. Again, this relation is the NCG scheme anticipated in the introduction.

FM in 1-D Lattice

To investigate the effect of varying $\mathrm{N_{cell}}$, the ULS of the 1-D lattice (at J=1 and T=1.2) is shown in Fig. 7.4(b) at fixed $\mathrm{N_c} = 2, 4$ and 6 (squares, crosses and pluses, respectively), with comparison to DCA ($\mathrm{N_{cell}} = \mathrm{N_c}$ with $2 \le \mathrm{N_c} \le 12$, given by circles). Except for an initial loss in accuracy (due to loss of translational invariance), the ULS converges

Table 7.1: Relative CPU time for 1-D Ising FM versus N_{cell} for (left) the $N_{cell} = N_c$ DCA, and (right) at fixed cluster size of N_c=2 with $N_{cell} \geq N_c$. For a given row, both methods yield the same value of $\beta G(\mathbf{k} = 0)$, see Fig. 7.4(b).

N_c=N_{cell}		N_c=2	
N_{cell}	CPU Time		N_{cell}
2	1.0	1.0	2
3	1.2	0.3	6
4	2.1	0.4	10
6	7.0	0.7	26
8	28	1.4	58
10	148	4.7	200
12	957	23	1000

monotonically to the exact value and converges at $N_{cell} \approx 1000$. Convergence is reached by the DCA at $N_c \approx 12$, but at the cost of solving for many more degrees of freedom.

In addition, we compare the CPU time for the DCA and the NCG methods with $N_{cell} > N_c$ at fixed values of ULS, i.e., at fixed level of accuracy, as shown in Table 7.1. For example, from Fig. 7.4(b), the ULS for DCA at $N_c = 6$ has the same level of accuracy as that of a $N_c = 2$ with a $N_{cell} = 26$. From Table 7.1 the CPU time is much less for NCG, because the number of independent cluster variables remains at $2N_c$ regardless of N_{cell}. The relationship can also be explained from another perspective. For $N_c = 6$ DCA, we must solve for 12 variables; however, one could trade computation time for accuracy by keeping terms only up to the NN (neglecting the rest), effectively doing a $N_c = 2$ calculation with $N_{cell} = 6$.

FM on FCC Lattice

For the FM transition, T_c on the FCC lattice is also compared and the results are tabulated in Table 7.2, together with exact T_c from MC and series expansion. As shown, at N_c=1 the cluster method (-8.9% deviation) already gives a huge improvement over the single-site Weiss estimation (23% deviation). The DCA and the NCG methods are equivalent at $N_c = 1$. For the DCA, we observe that the T_c progressively approaches the exact value from below as N_c increases. This is in contrast to NCG, where T_c^{exact} approaches monotonically from above and is more rapidly convergent than DCA versus N_c.

Table 7.2: Curie temperature ($T_c/12J$) for various cMFT and cluster sizes on FCC lattice. Percentage deviation from a series expansion (considered exact [217]) and finite-sized scaled MC results are given. CG results (equivalent to DCA) from optimal Bett's clusters (used in Fig. 7.5) are labelled as in [192]. NCG results exhibit faster convergence and agree with that from [191]. CG and NCG are equivalent at $N_c = 1$.

N_c	Label	$T_c/12J$	% Dev.	Method
1		1.0000	+22.5	Weiss
1		0.7437	-8.9	NCG
2		0.8344	+2.2	NCG
3		0.8264	+1.2	NCG
4		0.8200	+0.5	NCG
1		0.7437	-8.9	CG
4		0.7729	-5.3	CG
15	B	0.7862	-3.7	CG
16	A	0.7864	-3.7	CG
17	A	0.7874	-3.5	CG
19	A	0.7883	-3.4	CG
21	A	0.7898	-3.2	CG
21	E	0.7906	-3.1	CG
22	B	0.7914	-3.0	CG
23	A	0.7915	-3.0	CG
24	C	0.7917	-3.0	CG
24	D	0.7909	-3.1	CG
24	F	0.7923	-2.9	CG
24	K	0.7917	-3.0	CG
∞		0.8167	+0.06	MC
∞		0.8162	—	Series exp.

AFM on FCC Lattice

We applied the NCG method to the FCC AFM case with multisite clusters. Although the free energy of the disordered system can be obtained for a given T and h, we failed to get converged multisublattice ordered solutions for $\hat{\Sigma}$ and $\hat{G}$. The free energies of ordered phases could not be obtained and thus transitions could not be predicted. In the NCG scheme, $N_{cell} = \infty$ while a finite N_c cluster is used for the configurational average; hence, $\hat{\Sigma}$ is evaluated only for pairs within the (smaller) cluster, i.e., entries are non-zero in the (larger) cell only up to a certain range. However, from the perspective of DCA where

$N_{cell} = N_c$, all values of $\hat{\Sigma}$ are potentially finite. Although the values of Σ_{ij} decrease rapidly with shell distance for the disordered phase [218] (also observed in our work), this is not the case for ordered system. More investigation is needed to understand the convergence issues for the solution of the NCG method for general symmetry-broken ordered states.

7.5 Summary

From a general cluster-lattice transform with $N_{cell} \geq N_c$, we derived a set of cluster MFTs and applied them to the Ising Hamiltonian (no dynamics). For the case $N_c = N_{cell}$ we recover the same approximations used in the DCA and cDMFT methods. In the DCA-like approach, the lattice partition function Z[A] is simplified by considering only configurations within an N_c-site cluster $\hat{Z}$[A] such that the derived cluster pair correlation $\hat{G}$ is consistent with the lattice G from Dyson's equation (7.3). As a result, G inherently obeys the mathematical sum rules in (7.2) for $i, j \in$ cluster, violated in most other MFTs. The DCA-like formulation can be done in **r**-space or **k**-space and retains the appropriate translational invariance within the cluster, and is therefore applicable to general cases using various cluster sizes.

We extended these concepts to a non-coarse-grained (NCG) variant with $N_{cell} \gg N_c$, $N_{cell} \to \infty$, and showed it was accurate and more computationally efficient, but that does not guarantee translational invariance of the cluster. This limiting case becomes equivalent to a MFT suggested by Tokar [191], using ideas of the CPA that ignored cluster boundary conditions. We applied these cluster MFT to the Ising Hamiltonian to predict phase transitions T_c and $T - h$ boundary topology. Here, using the DCA and NCG version, we studied the FM case in 1-D lattice and both FM and AFM cases on FCC lattice. Predictions of T_c and phase boundaries approaches that of Monte Carlo with increased cluster size, N_c.

Already at $N_c = 1$ for the AFM case the predicted T_c's are quantitative and topologically correct versus external field h; basically the $N_c = 1$ case recovers the conservation of particle number forced within Onsager's cavity theory or Brout's spherical model but has an improved description of free energies for both first- and second-order phase transitions. We extended the concept to generalized clusters, illustrating finite-size scaling on FCC

lattices for the FM T_c versus N_c and for the AFM tricritical-point T_t, both of which agree with MC. For the FCC FM, the NCG variant requires a smaller N_c and, hence, much shorter computation time to achieve the same level of accuracy as the DCA using larger clusters. The NCG method may be useful to tackle larger quantum cluster calculations.

We are extending these concepts to cluster expansions that include multibody interactions by expanding multibody correlations as cumulants and retaining only cumulants involving pairs and single-site. In related work, a first-principles, KKR-DCA has been implemented to improve the ensemble averaging (i.e., beyond the KKR-CPA) and include atomic correlations within the electronic-structure [219, 220]. The results here may help provide a means to predict free energy and directly determine the atomic short-range order in complex alloys.

7.6 Cluster Field-Theory Formalism

Here we summarize the cluster field-theory to solving for cluster $\hat{\Sigma}$, $\hat{G}$ and the cluster free energy. Using vector notation, the partition function in (7.8) for the Ising Hamiltonian (7.1) on an N-site lattice, with vector m denoting magnetization of N sites, is separated into a product of single-site and pair terms as

$$Z[A] = e^{mA} Z_{MF}[m] \det(2\pi G)^{1/2} e^{\frac{1}{2}AGA} R[AG] \ . \tag{7.42}$$

Z_{MF} is $\exp(-\beta E_1)$, where E_1 is the single-site, mean-field energy (Sect. 7.2), $\det(2\pi G)$ arises from factoring out the Gaussian part of the pair correlations, and A is the source field vector (see Tokar [191] for details). The last term, containing information beyond MFT and Gaussian fluctuations, is the generating functional of the S-matrix [221], and is given by [191]

$$\begin{aligned} R[\phi] &= \exp(\frac{1}{2}\partial_\phi G \partial_\phi) \exp[-\frac{1}{2}\phi\Sigma\phi + \beta(\bar{h} + mJ)\phi] \\ &\quad \prod_i [\delta(\phi_i + m_i - 1) + \delta(\phi_i + m_i + 1)]. \end{aligned} \tag{7.43}$$

Delta functions arise due to use of continuous field variables rather than discrete variables ($\sigma_i = \pm 1$) for the derivation. From (7.9) and (7.42), one deduces that

$$\frac{\partial \ln R[AG]}{\partial A_i}\Big|_{A=0} = 0 \quad ; \quad \frac{\partial^2 \ln R[AG]}{\partial A_i \partial A_j}\Big|_{A=0} = 0 \tag{7.44}$$

Setting A=0 in (7.42) the free energy $F = -k_B T \ln Z[0]$ is

$$F = E_1 - \frac{k_B T}{2} \ln \det(2\pi G) - k_B T \ln R[0] \tag{7.45}$$

which is equivalent to Eq. (17) in [191]. With no approximations in the derivation thus far, calculating $R[0]$ amounts to solving the Ising model exactly, which is only tractable in limited cases.

We use the CG methods decribed in the text that maintain Dyson's relation to build in the proper boundary conditions and relation between cluster and lattice variable missing in the original theory. The cMFT divides the lattice into identical non-overlapping, $\mathrm{N_c}$-site clusters, i.e., pair correlations between sites of different clusters are ignored. With the cluster $\hat{\Sigma}$ and $\hat{G}$ given as $\mathrm{N_c} \times \mathrm{N_c}$ matrices, $R[AG]$ is decoupled into products of independent clusters (denoted by 'c'), i.e.,

$$\begin{aligned} R[AG] &\approx e^{-\beta(\bar{h}+mJ)m} \prod_{\mathrm{c}} \det\left(2\pi\hat{G}\right)^{-1/2} \\ &\times e^{-\frac{1}{2}m\left(\hat{G}^{-1}+\hat{\Sigma}\right)m} e^{-\frac{1}{2}A\hat{G}A - mA} \times \hat{\mathrm{Z}}[A], \end{aligned} \tag{7.46}$$

with the cluster partition function given by

$$\begin{aligned} \hat{\mathrm{Z}}[A] = \mathrm{Tr}_{\sigma\in c} \exp\Big\{ &\left[m\left(\hat{G}^{-1}+\hat{\Sigma}\right) + \beta m J\right]\sigma \\ &-\frac{1}{2}\sigma\left(\hat{G}^{-1}+\hat{\Sigma}\right)\sigma + \beta\bar{h}\sigma + A\sigma\Big\} \quad , \end{aligned} \tag{7.47}$$

where the trace is over $\mathrm{N_c}$ cluster sites with σ_i summed over the values, -1 and $+1$. Hence,

Eq. (7.44) becomes

$$\hat{m}_i = \frac{\partial \ln \hat{\mathrm{Z}}[A]}{\partial A_i}\Big|_{A=0} \;\; ; \;\; \hat{G}_{ij} = \frac{\partial^2 \ln \hat{\mathrm{Z}}[A]}{\partial A_i \partial A_j}\Big|_{A=0}, \tag{7.48}$$

from which the cluster $\hat{\mathrm{G}}$ is obtained. The $\hat{\mathrm{G}}$ thus derived satisfy (7.2) naturally for $i, j \in$ cluster.

Alternatively, by expressing the cluster partition function as $\hat{\mathrm{Z}}[\mathrm{A}] \equiv \exp[-\beta(<\hat{\mathrm{E}}> - T\hat{\mathrm{S}})]$, we have expressed the cluster free energy derived from (7.45) and (7.46) more intuitively as in (7.28) where, for equivalent clusters, the cluster sum yields a factor of $\mathrm{N}/\mathrm{N_c}$ (the number of clusters in the lattice). The cluster entropy is given by $\hat{\mathrm{S}} = -k_B \mathrm{Tr}_{\sigma \in c}(P_\sigma \ln P_\sigma)$, which is separable into point, pairs, etc., within the cluster. For $\mathrm{N_c}$=1, (7.48) yields (7.33) and (7.32).

The key to any cluster approximation is then to relate the cluster $\hat{\mathrm{G}}$ and $\hat{\Sigma}$ to the correct lattice G and Σ in (7.3), as is done here via DCA concepts, and use them in the correct cluster $\hat{\mathrm{Z}}[\mathrm{A}]$ for thermodynamics. For example, for a 4-atom cluster, the trace in (7.46) is evaluated for 16 configurations, which inherently includes multisite entropy.

CHAPTER 8

CONCLUSIONS AND FUTURE DEVELOPMENTS

Alloy phase diagrams are of great use in materials design for both scientific and engineering purposes. To prevent compromising the design requirement, it is important to know if the intended alloy phase is stable under the operating conditions, hence the need for alloy phase diagrams. In this work, we detail the cluster expansion (CE) method, which uses first-principles alloy structural energies to construct an effective Hamiltonian, that is suitable for thermodynamics calculations and phase diagram construction of multi-component alloys, via methods such as Monte Carlo (MC) simulations and mean-field theories.

For this purpose, I have developed the Thermodynamics Toolkit (TTK) software package and apply it to study order-disorder phase transitions in various alloys. For the CE to be useful and computationally efficient, it needs to be rapidly convergent with respect to the number of clusters, and the cluster interactions are typically obtained via structural inversion of a subset of structural energies. Existing methods further use statistical measures such as cross-validation to select optimally truncated CE sets, which, however, is often non-unique. We first showcase such current methods to several real alloys, enforcing a physics based rule to ensure compact and locally complete CE basis, which serves to reduce the problem of non-uniqueness by eliminating unphysical choices.

For phase-segregating Ca-Sr and Pd-Rh alloy systems, the CE Hamiltonians were used to construct phase boundaries via MC and a rapid mean-field estimate, both agreeing well with available experimental results. The CE is applied to Ag-Au alloy, which orders at low temperatures. The Ag-Au cluster interactions are dominated by the nearest-neighbor pair interaction, resulting in degenerate structures that lead to an interestingly narrow coexistent regions in the phase diagram. To emphasize their physical meaning, the CE interactions were shown to compare well to those obtained directly via first-principles calculations of

dilute structures, for the Ag-Au alloy.

We then return to address the issue of uniqueness of truncated CE sets. Using fractional factorial design principles, we explain how the choice of structural sets impact the linear dependencies between the cluster basis functions, and how this would result in a bias estimate of the cluster interactions. The bias is minimized when all important interactions are included in the truncated CE. This is achieved by combining our knowledge of the cluster dependencies with a previously proposed cluster hierarchy implemented in TTK. This led to the subspace projection method, which allows the cluster interactions of the truncated CE basis to approach that of the unique and non-truncated one, relying on a minimal set of first-principles structural energies for structural inversion.

Finally, as an alternative to expensive (but exact) Monte Carlo simulations, we highlight a cluster mean-field theory (cMFT), which produces good quantitative estimates of phase boundaries for the Ising Hamiltonian. Using a cluster-lattice Fourier transform with a cluster of size N_c and a lattice coarse-grained (CG) into cells of size N_{cell}, a set of static, self-consistent equations relating cluster and CG lattice correlations are obtained. In the case of $N_c = 1$, the cluster-lattice relation recovers the sum-rule for conserving particle number (or equivalently the self-correlation), which are ignored by most MFTs in the past. The approach closely mirrors the CG techniques and self-consistent requirement utilized in quantum cluster theories such as DCA and cDMFT. The 'new' cMFT improves thermodynamic predictions, recovering Monte Carlo and series expansion results upon finite-size scaling; yet, the method at $N_c = 1$ already predicts well the first- and second-order phase boundary topologies and transition temperatures for frustrated lattices. We also explore forms with $N_{cell} \geq N_c$, especially an NCG version with $N_{cell} \to \infty$, which compared to the $N_c = N_{cell}$ CG case, the NCG version is faster computationally and more accurate at fixed N_c.

8.1 Future Developments

To enable its use in the general CE Hamiltonian, the cMFT, which is directly applicable to Ising Hamiltonians, has to be extended to consider multi-body correlations. A possible

way forward is to express the higher-order correlations into that of pairs (G_{ij}), which are treated well by the cMFT, and higher-order terms, which can be approximated using cumulant expansion.

For the subspace projection method, it is straightfoward to generalize to M-component systems via the representation offered by Chebyshev polynomials, given by $\phi_k(\sigma_i)$ for each site i. Orthogonal multi-site cluster functions are obtained by multiplying $\phi_k(\sigma_i)$ from each site [2]. In the binary case (M=2), it turns out that the two orthogonal single-site cluster functions are $\phi_1(\sigma_i) = 1$ and $\phi_2(\sigma_i) = \sigma_i$, corresponding to the spin variables that are well discussed with $\sigma_i = 1$ or -1. In the complete space, the orthogonal column vectors of the N-site correlation matrix, $\Phi_{2^N \times 2^N}$, are constructed by $\phi_{k_1}(\sigma_{i_1})...\phi_{k_N}(\sigma_{i_N})$. The Hadamard matrix is recovered when the columns are ordered accordingly (see Chapter 6). In the case of M=3, $\phi_1(\sigma_i) = 1$, $\phi_2(\sigma_i) = \sqrt{3/2}\sigma_i$ and $\phi_3(\sigma_i) = \sqrt{2} - 3/\sqrt{2}\sigma_i^2$, with $\sigma_i = 1,\ 0$ or -1. Using $\phi_{k_1}(\sigma_{i_1})...\phi_{k_N}(\sigma_{i_N})$, an orthogonal $\Phi_{3^N \times 3^N}$ is constructed and the concepts from subspace projection can likewise be applied.

In summary, we have developed a CE-based multiscale package for calculating thermodynamic properties of general multicomponent alloys from first-principles. When the new SSP method is made fully functional in TTK, we have a software package that produces a unique and reliable truncated CE using minimal input from first-principles calculations. Because the TTK code is written to treat multi-component alloys (ternaries and beyond) and for general lattices (including those with multiple sublattices), it can be used to study more complex systems in the future, such as for surfaces and nanoclusters. When these techniques are integrated in TTK, we will have a computation toolkit that permit a rapid and reliable approach for characterization and discovery of alloy materials.

REFERENCES

[1] N. Saunders and A. Miodownik, *CALPHAD (Calculation of Phase Diagrams): A Comprehensive Guide, Volume 1*, Pergamon Materials Series (Elsevier Science Ltd., Oxford, UK, 1998).

[2] J.M. Sanchez, F. Ducastelle, and D. Gratias, Physica **128 A**, 334 (1984).

[3] B.D. Krack, V. Ozoliņš, M. Asta, and I. Daruka, Phys. Rev. Lett. **88**, 186101 (2002).

[4] M. Sanati, L.G. Wang, and Alex Zunger, Phys. Rev. Lett. **90**, 045502 (Jan 2003).

[5] J.W.D. Connolly and A.R. Williams, Phys. Rev. B **27**, R5169 (1983).

[6] N.A. Zarkevich and D.D. Johnson, Phys. Rev. Lett. **92**, 255702 (2004).

[7] N.A. Zarkevich, Complexity **11**, 36 (2006).

[8] N.A. Zarkevich, Teck L. Tan, and D.D. Johnson, Phys. Rev. B **75**, 104203 (2007).

[9] M. Asta, C. Wolverton, D. de Fontaine, and H. Dreyssé, Phys. Rev. B **44**, 4907 (1991).

[10] C. Wolverton, M. Asta, H. Dreyssé, and D. de Fontaine, Phys. Rev. B **44**, 4914 (1991).

[11] J.M. Sanchez, Phys. Rev. B **48**, 14013 (1993).

[12] A. van de Walle and G. Ceder, Rev. Mod. Phys. **74**, 11 (2002).

[13] S.V. Barabash, V. Blum, S. Muller, and A. Zunger, Phys. Rev. B **74**, 035108 (2006).

[14] V. Vaithyanathan, C. Wolverton, and L.Q. Chen, Phys. Rev. Lett. **88**, 125503 (2002).

[15] C. Wolverton and V. Ozoliņš, Phys. Rev. Lett. **86**, 5518 (2001).

[16] N.A. Zarkevich and D.D. Johnson, Phys. Rev. B **67**, 064104 (2003).

[17] N.A. Zarkevich, D.D. Johnson, and A.V. Smirnov, Acta Mater. **50**, 2443 (2002).

[18] V. Ozoliņš and M. Asta, Phys. Rev. Lett. **86**, 448 (2001).

[19] A. Van der Ven, G. Ceder, M. Asta, and P.D. Tepesch, Phys. Rev. B **64**, 184307 (2001).

[20] R. Drautz, H. Reichert, M. Fahnle, H. Dosch, and J.M. Sanchez, Phys. Rev. Lett. **87**, 236102 (2001).

[21] G.L.W. Hart and A. Zunger, Phys. Rev. Lett. **87**, 275508 (2001).

[22] S. Müller and A. Zunger, Phys. Rev. Lett. **87**, 165502 (2001).

[23] N.A. Zarkevich and D.D. Johnson, Surf. Sci. Lett. **591**, L292 (2005).

[24] G.J. Xu, N.A. Zarkevich, A. Agrawal, A.W. Signor, B.R. Trenhaile, D.D. Johnson, and J.H. Weaver, Phys. Rev. B **71**, 115332 (2005).

[25] *Desk Handbook: Phase Diagrams for Binary Alloys*, edited by H. Okamoto (ASM Int., Materials Park, Ohio, 2000).

[26] N. W. Ashcroft and N. D. Mermin, *Solid State Physics* (Holt, Rinehart, and Winston, New York, 1976).

[27] R. E. Warren, *X-ray Diffraction* (Addison-Wesley, Reading, MA, 1969).

[28] A. Santoro and A. Mighell, Acta Crystallographica Section A **28**, 284 (1972).

[29] A.G. Khachaturyan, *Theory of Phase Transformations and Structure of Solid Solutions* (Nauka, Moscow, USSR, 1974) in Russian.

[30] J. M. Cowley, Phys. Rev. **77**, 669 (Mar 1950).

[31] F. Ducastelle, *Order and Phase Stability in Alloys* (NorthHolland, New York, 1991).

[32] P. Hohenberg and W. Kohn, Phys. Rev. **136**, B864 (Nov 1964).

[33] T. Lee and C. Yang, Phys. Rev. **87**, 410 (Aug 1952).

[34] G. Kresse and J. Furthmüller, Phys. Rev. B **54**, 11169 (1996).

[35] P. E. Blöchl, Phys. Rev. B **50**, 17953 (Dec 1994).

[36] G. Kresse and D. Joubert, Phys. Rev. B **59**, 1758 (Jan 1999).

[37] N. Harrison, *Introduction to density functional theory*, online article.

[38] Richard M. Martin, *Electronic structure basic theory and practical methods* (Cambridge University Press., Cambridge, UK, 2004).

[39] W. Kohn and L. J. Sham, Phys. Rev. **140**, A1133 (Nov 1965).

[40] D. Ceperley and B. Alder, Phys. Rev. Lett. **45**, 566 (Aug 1980).

[41] J. Perdew and A. Zunger, Phys. Rev. B **23**, 5048 (May 1981).

[42] S.H. Vosko, L. Wilk, and M. Nusair, Canadian Journal of Physics **58**, 1200 (1980).

[43] J.P. Perdew, J.A. Chevary, S.H. Vosko, K.A. Jackson, M.R. Pederson, D.J. Singh, and C. Fiolhais, Phys. Rev. B **46**, 6671 (1992).

[44] W.H. Press, S.A. Teukolsky, W.T. Vetterling, and B.P. Flannery, *Numerical Recipes in C, 2nd Ed.* (Cambridge University Press, Cambridge, UK, 1992).

[45] R. Kikuchi, Phys. Rev. **81**, 988 (1951).

[46] J. M. Sanchez and D. de Fontaine, Phys. Rev. B **17**, 2926 (Apr 1978).

[47] R. Kikuchi and K. Masuda-Jindo, Calphad **28**, 33 (2002).

[48] M. Allen and D. Tildesley, *Computer simulation of liquids* (Oxford University Press Inc., New York, 1987).

[49] D. Frenkel and B. Smit, *Understanding molecular simulation: From algorithms to applications, second edition*, Computational Science Series, Volume 1 (Academic Press, London, UK, 2002).

[50] N. Metropolis, A. Rosenbluth, M. Rosenbluth, A.M. Teller, and E. Teller, J. Chem. Phys. **21**, 1087 (1953).

[51] Z. W. Lu, B. M. Klein, A. Zunger, J. Phase Equilib. **16**, 36 (1995).

[52] Alex Zunger, L.G. Wang, Gus L.W Hart, and Mahdi Sanati, Modelling and Simulation in Materials Science and Engineering **10**, 685 (2002).

[53] A. van de Walle and G. Ceder, J. of Phase Equilibria **23**, 348 (2002).

[54] G. Garbulsky and G. Ceder, Phys. Rev. B **49**, 6327 (1994).

[55] S. H. Wei, A. A. Mbaye, L. G. Ferreira, and A. Zunger, Phys. Rev. B **36**, 4163 (Sep 1987).

[56] N.A. Zarkevich, Teck L. Tan, L.-L. Wang, and D.D. Johnson, Phys. Rev. B **77**, 144208 (2008).

[57] P. Asta, V. Ozolins, and C. Woodward, JOM **53**, 16 (2001).

[58] R. Drautz and A. Díaz-Ortiz, Phys. Rev. B **73**, 224207 (Jun 2006).

[59] Gus L. W. Hart, Volker Blum, Michael J. Walorski, and Alex Zunger, Nature Materials **4**, 391 (2005).

[60] V. Blum, G. L. W. Hart, M. J. Walorski, and A. Zunger, Phys. Rev. B **72**, 165113 (Oct 2005).

[61] B.L. Raktoe, A. Hedayat, and W.T. Federer, *Factorial designs*, Wiley Series in Probability and Mathematical Statistics (John Wiley & Sons, Inc., Canada, 1981).

[62] A.S. Hedayat, N.J.A. Sloane, and John Stufken, *Orthogonal arrays: theory and applications*, Springer Series in Statistics (Springer-Verlag, New York, 1999).

[63] A. van de Walle, *Alloy Theoretic Automated Toolkit (ATAT) webpage*, http://www.its.caltech.edu/ avdw/atat/.

[64] A. van de Walle and M. Asta, Modelling Simul. Mater. Sci. Eng. **10**, 521 (2002).

[65] A. van de Walle(2005), private communications.

[66] L.G. Ferreira, S.H. Wei, and A. Zunger, Int. J. Supercomput. Appl. **5**, 34 (1991).

[67] P.E. Blöchl, Phys. Rev. B **50**, 17953 (1994).

[68] G. Kresse and D. Joubert, Phys. Rev. B **59**, 1758 (1999).

[69] H.J. Monkhorst and J.D. Pack, Phys. Rev. B **13**, 5188 (1976).

[70] D.D. Johnson, Phys. Rev. B **38**, 12807 (1988).

[71] M. Stone, J. Roy. Stat. Soc., B (methodological) **36**, 111 (1974).

[72] D. Allen, Technometrics **16**, 125 (February 1974).

[73] K.-C. Li, Ann. Stat. **15**, 958 (1987).

[74] M.H.F. Sluiter, Y. Watanabe, D. de Fontaine, Y. Kawazoe, Phys. Rev. B **53**, 6137 (1996).

[75] A.A. Rudnitskiy, R.S. Polyakova, and I.I. Tyurin, Izv. Sektora Platiny i Drug. Blagorodn. Metal. **29**, 190 (1955).

[76] E. Raub, H. Beeskow, and D. Menzel, Z. Metallk. **50**, 428 (1959).

[77] J.E. Shield and R.K. Williams, Scr. Metall. **21**, 1475 (1987).

[78] P.E.A. Turchi, G.M. Stocks, W.H. Butler, D.M. Nicholson, and A. Gonis, Phys. Rev. B **37**, 5982 (April 1988).

[79] D.D. Johnson, P.E.A. Turchi, M. Sluiter, D.M. Nicholson, F.J. Pinski, G.M. Stocks, in *Alloy Phase Stability and Design*, Mat. Res. Soc. Symp. Proc., Vol. 186, edited by G.M. Stocks, D.P. Pope, and A.F. Gaimei (Materials Research Society, Pittsburgh, 1991) pp. 21–26.

[80] C. Wolverton, D. de Fontaine, H. Dreyssé, Phys. Rev. B **48**, 5766 (1993).

[81] C.B. Alcock and V.P. Itkin, Bull. Alloy Phase Diagrams **7**, 455 (1986).

[82] A.G. Khachaturyan, *Theory of Structural Transformations in Solids* (Wiley, New York, 1983).

[83] H.A. Bethe, Proc. Roy. Soc. London A **150**, 552 (1935).

[84] G.S. Rushbrooke, Proc. Roy. Soc. London A **166**, 296 (1938).

[85] R. Pathria, *Statistical Mechanics* (Pergamon Press, 1972).

[86] Sergei Galam, Phys. Rev. B **54**, 15991 (1996).

[87] Sergei Galam, J. of Appl. Phys. **87**, 7040 (2000).

[88] N.A. Zarkevich, Teck L. Tan, and D.D. Johnson, "Ttk toolkit," (2006).

[89] A.A. Rudnitskii and A.N. Khotinskaya, Russ. J. Inorg. Chem. **4**, 1160 (1959).

[90] E. Raub, G. Falkenburgh, Z. Metallkd. **55**, 392 (1964).

[91] H. Okamoto, T.B. Massalski, Bull. Alloy Phase Diagrams **5** (1984).

[92] T.B. Massalski, H. Okamoto, L. Brewer, *Phase Diagrams of Binary Gold Alloys* (ASM International, 1987).

[93] S. Curtarolo, D. Morgan, G. Ceder, Computer Coupling of Phase Diagrams and Thermochemistry **29**, 163 (2005).

[94] F. Doerinckel, Z. Anorg. Allg. Chem. **34**, 333 (1907).

[95] C.H. Johnsson, J.O. Linde, Ann. Phys. **5**, 762 (1930).

[96] M. Hansen, K. Anderko, *Constitution of Binary Alloys* (McGraw-Hill, New York, 1958).

[97] H. Okamoto, T.B. Massalski, Bull. Alloy Phase Diagrams **6** (1985).

[98] A.A. Rudnitskii and A.N. Khotinskaya, Russ. J. Inorg. Chem. **4**, 1053 (1959).

[99] I. Barin, O. Knacke, O. Kubaschewski, *Thermodynamical Properties of Inorganic Substances (Suppl.)* (Springer-Verlag, Berlin, 1977).

[100] I. Karakaya and W.T. Thompson, Bull. Alloy Phase Diagrams **7**, 259 (1986).

[101] *CRC Handbook of Chemistry and Physics*, edited by D.R. Lide (CRC Press Inc., Cleveland, OH, 2003).

[102] M.N. Tamashino and S.R. Salinas, Phys. Rev. B **56**, 8241 (1997).

[103] V. Ozolins, C. Wolverton, and A. Zunger, Phys. Rev. B **58**, R5897 (1998).

[104] O. Delaire, T. Swan-Wood, B. Fultz, Phys. Rev. Lett. **93**, 185704 (2004).

[105] P.D. Bogdanoff and B. Fultz, Philos. Mag. B **79**, 753 (1999).

[106] V. L. Moruzzi, J. F. Janak, and K. Schwarz, Phys. Rev. B **37**, 790 (1988).

[107] M. Asta and V. Ozoliņš, Phys. Rev. B **64**, 094104 (2001).

[108] O. Delaire, B. Fultz, Phys. Rev. Lett. **97**, 245701 (2006).

[109] P. D. Bogdanoff and B. Fultz, Phil. Mag. B **79**, 753 (1999).

[110] P. D. Bogdanoff and B. Fultz, Phil. Mag. B **81**, 299 (2001).

[111] K.A. Gschneider, in *Solid State Physics*, edited by F. Seitz and D. Turnbull (Academic, New Yoirk, New York, 1967) p. 275.

[112] Dayong Cheng, Shaoqing Wang, and Hengqiang Ye, Phys. Rev. B **64**, 024107 (2001).

[113] F.J. Pinski, B.Ginatempo, D.D.Johnson, J.B. Staunton, G.M. Stocks, and B.L. Gyorffy, Phys. Rev. Lett. **66**, 766 (1991).

[114] F.J. Pinski, B.Ginatempo, D.D.Johnson, J.B. Staunton, G.M. Stocks, and B.L. Gyorffy, Phys. Rev. Lett. **68**, 1962 (1992).

[115] I. S. Hagemann, Q. Huang, X. P. A. Gao, A. P. Ramirez, and R. J. Cava, Phys. Rev. Lett. **86**, 894 (Jan 2001).

[116] C. Rossel, Y. Maeno, and I. Morgenstern, Phys. Rev. Lett. **62**, 681 (Feb 1989).

[117] S. R. McKay, A. N. Berker, and S. Kirkpatrick, Phys. Rev. Lett. **48**, 767 (Mar 1982).

[118] B. Pannetier, J. Chaussy, R. Rammal, and J. C. Villegier, Phys. Rev. Lett. **53**, 1845 (Nov 1984).

[119] A. J. Bray and M. A. Moore, Phys. Rev. Lett. **58**, 57 (Jan 1987).

[120] P. Chandra, P. Coleman, and A. I. Larkin, Phys. Rev. Lett. **64**, 88 (Jan 1990).

[121] A. P. Ramirez, G. P. Espinosa, and A. S. Cooper, Phys. Rev. Lett. **64**, 2070 (Apr 1990).

[122] C. M. Newman and D. L. Stein, Phys. Rev. Lett. **72**, 2286 (Apr 1994).

[123] P. Schiffer, A. P. Ramirez, D. A. Huse, P. L. Gammel, U. Yaron, D. J. Bishop, and A. J. Valentino, Phys. Rev. Lett. **74**, 2379 (Mar 1995).

[124] M. V. Feigelman and L. B. Ioffe, Phys. Rev. Lett. **74**, 3447 (Apr 1995).

[125] P. Chandra, L. B. Ioffe, and D. Sherrington, Phys. Rev. Lett. **75**, 713 (Jul 1995).

[126] M. J. Harris, S. T. Bramwell, D. F. McMorrow, T. Zeiske, and K. W. Godfrey, Phys. Rev. Lett. **79**, 2554 (Sep 1997).

[127] S. I. Matveenko and S. I. Mukhin, Phys. Rev. Lett. **84**, 6066 (Jun 2000).

[128] M. García-Hernández, J. L. Martínez, M. J. Martínez-Lope, M. T. Casais, and J. A. Alonso, Phys. Rev. Lett. **86**, 2443 (Mar 2001).

[129] A. Keren and J. S. Gardner, Phys. Rev. Lett. **87**, 177201 (Oct 2001).

[130] F. Becca and F. Mila, Phys. Rev. Lett. **89**, 037204 (Jul 2002).

[131] G. Ceder, M. De Graef, L. Delaey, J. Kulik, and D. de Fontaine, Phys. Rev. B **39**, 381 (Jan 1989).

[132] N. M. Rosengaard and H. L. Skriver, Phys. Rev. B **49**, 14666 (May 1994).

[133] J. Kulik and D. de Fontaine, J. Phys. C: Solid State Phys. **21**, L291 (1988).

[134] D. deFontaine, J. Kulik, Acta Metall. **33**, 145 (2001).

[135] J. Kulik, S. Takeda, D. De Fontaine, Acta Metall. **35**, 1137 (2001).

[136] D. Broddin, G. Van Tendeloo, Van Landuyt, Philos. Mag. A **54**, 395 (1986).

[137] G. Ceder, D. de Fontaine, H. Dreyssé, D.M. Nicholson, G.M. Stocks, B.L. Gyorffy, Acta Metall. **38**, 2299 (1990).

[138] T. Nakano, A. Negishi, K. Hayashi, Y. Umakoshi, Acta Materialia **47**, 1091 (1999).

[139] M. Hirabayashi, K. Hiraga and D. Shindo, J. Appl. Cryst. **14**, 169 (1981).

[140] H. T. Diep, A. Ghazali, B. Berge, and P. Lallemand, Europhysics Letters **2**, 603 (1986).

[141] Joel L. Lebowitz, Mohan K. Phani, and Daniel F. Styer, J. of Stat. Phys. **38**, 413 (1985).

[142] U. Gahn, J. Phys. Chem. Solids **47**, 1153 (1986).

[143] D. C. Chrzan and L. M. Falicov, Phys. Rev. B **37**, 3894 (Mar 1988).

[144] D. C. Chrzan and L. M. Falicov, Phys. Rev. B **40**, 8194 (Oct 1989).

[145] K. Binder, Phys. Rev. Lett. **45**, 811 (Sep 1980).

[146] K. S. Kammerer, B. Dunweg and M. d'Onorio de Meo, Phys. Rev. B **53**, 2345 (1996).

[147] C.M. van Baal, Physics (Utrecht) **64**, 571 (1973).

[148] R. Kikuchi, J. Chem. Phys. **60**, 1071 (1974).

[149] R. Kikuchi, J.M. Sanchez, D. de Fontaine, H. Yamauchi, Acta Metall. **28**, 651 (1980).

[150] V. Ozoliņš, C. Wolverton, and A. Zunger, Phys. Rev. B **57**, 6427 (1998).

[151] Z. W. Lu, B. M. Klein, and A. Zunger, Modelling Simul. Mater. Sci. Eng. **3**, 753 (1995).

[152] K. Terakura, T. Oguchi, T. Mohri, and K. Watanabe, Phys. Rev. B **35**, 2169 (Feb 1987).

[153] R. Drautz, M. Fahnle, and J.M. Sanchez, J. Phys.: Condens. Matter **16**, 3834 (2004).

[154] Daniel F. Styer, Mohan K. Phani, and Joel L. Lebowitz, Phys. Rev. B **34**, 3361 (Sep 1986).

[155] A. Finel and F. Ducastelle, Europhys. Lett. **1**, 135 (1986).

[156] H.T. Diep, A. Ghazali, B. Berge, and P. Lallemand, Europhys. Lett. **2**, 603 (1986).

[157] A.D. Beath and D.H. Ryan, Phys. Rev. B **73**, 214445 (2006).

[158] H. T. Diep and H. Kawamura, Phys. Rev. B **40**, 7019 (Oct 1989).

[159] P. Turchi, M. Sluiter, and D. de Fontaine, Phys. Rev. B **36**, 3161 (Aug 1987).

[160] J. Sadoc and R. Mosseri, *Geometrical Frustration* (Cambridge University Press, 1999).

[161] M. Elhajal, B. Canals, C. Lacroix, Journal of Magnetism and Magnetic Materials **226-230**, 379 (2001).

[162] G. Ceder, G. D. Garbulsky, D. Avis, and K. Fukuda, Phys. Rev. B **49**, 1 (Jan 1994).

[163] R. Tetot, A. Finel, and F. Ducastelle, J. of Stat. Phys. **61**, 121 (1990).

[164] D. de Fontaine, Solid State Phys. **47**, 33 (1994).

[165] A. Zunger, in *Statics and Dynamics of Alloy Phase Transformations*, edited by P. Turchi and A. Gonis (NATO ASI Series, Plenum, New York, 1994) p. 361.

[166] D.D. Johnson, in *Encyclopedia of Materials: Science & Technology*, edited by K.H.J. Buschow et al. (Elsevier, NY, 2001).

[167] B.L. Gyorffy and G.M. Stocks, Phys. Rev. Lett. **50**, 374 (1983).

[168] F. Ducastelle and F. Gautier, J. Phys. F **6**, 2039 (1976).

[169] F. Ducastelle and G. Treglia, J. Phys. F **10**, 2137 (1980).

[170] H. Dreyessé, A. Berera, L.T. Wille, and D. de Fontaine, Phys. Rev. B **39**, 2442 (1989).

[171] M. Sluiter and P. Turchi, Phys. Rev. B **40**, 11215 (1989).

[172] M. Sluiter and P. Turchi, Phys. Rev. B **36**, 4630 (1987).

[173] A. C. Tamhane, *Statistical analysis of designed experiments*, Wiley Series in Probability and Mathematical Statistics (John Wiley & Sons, Inc., Hoboken, New Jersey, 2009).

[174] NIST/SEMATECH, http://www.itl.nist.gov/div898/handbook/.

[175] K. Horadam, *Hadamard matrices and their applications* (Princeton University Press, Princeton, 2007).

[176] George E. P. Box and R. Daniel Meyer, Technometrics **28**, pp. 11 (1986).

[177] Rahul Mukerjee and C.F. Jeff Wu, *A modern theory of factorial designs*, Springer Series in Statistics (Springer Science+Business Media, Inc., New York, 2006).

[178] M. Hamada and C.F.J. Wu, Journal of Quality Technology **24**, 130 (1992).

[179] Gus L.W. Hart and Rodney W. Forcade, Phys. Rev. B **80**, 014120 (Jul 2009).

[180] F. Cyrot-Lackmann, Journal of Physics and Chemistry of Solids **29**, 1235 (1968).

[181] F. Ducastelle and F. Cyrot-Lackmann, Journal of Physics and Chemistry of Solids **31**, 1295 (1970).

[182] F. Ducastelle and F. Cyrot-Lackmann, Journal of Physics and Chemistry of Solids **32**, 285 (1971).

[183] L. Onsager, Phys. Rev. **65**, 117 (Feb 1944).

[184] G. Biroli, O. Parcollet, and G. Kotliar, Phys. Rev. B **69**, 205108 (May 2004).

[185] T. Maier, M. Jarrell, T. Pruschke, and M. H. Hettler, Rev. Mod. Phys. **77**, 1027 (Oct 2005).

[186] P. Soven, Phys. Rev. **156**, 809 (Apr 1967).

[187] D. W. Taylor, Phys. Rev. **156**, 1017 (Apr 1967).

[188] M. Jarrell and H. R. Krishnamurthy, Phys. Rev. B **63**, 125102 (Mar 2001).

[189] P. R. C. Kent, M. Jarrell, T. A. Maier, and T. Pruschke, Phys. Rev. B **72**, 060411 (Aug 2005).

[190] V. I. Tokar, Physics Letters A **110**, 453 (1985).

[191] V. I. Tokar, Computational Materials Science **8**, 8 (1997).

[192] G. E. Stewart, D. D. Betts and J. S. Flynn, J. Phys. Soc. Jpn. **66**, 3231 (1997).

[193] P. Weiss, J. de Phys. **6**, 661 (1907).

[194] W. Shockley, Journal of Chemical Physics **6**, 130 (1938).

[195] L. Onsager, J. Am. Chem. Soc. **58**, 1486 (1936).

[196] J. B. Staunton and B. L. Györffy, Phys. Rev. Lett. **69**, 371 (Jul 1992).

[197] J. B. Staunton, D. D. Johnson, and F. J. Pinski, Phys. Rev. B **50**, 1450 (Jul 1994).

[198] R. Brout, Phys. Rev. **122**, 469 (1961).

[199] R. Brout, *Phase Transitions* (Benjamin, New York, 1965).

[200] Yu. A. Izyumov and Yu. N. Skryabin, *Statistical Mechanics of Magnetically Ordered Systems* (Consultants Bureau, New York and London, 1988).

[201] D. D. Johnson, J. B. Staunton, and F. J. Pinski, "Computation of diffuse intensities in alloys," in *Methods in Materials Science*, edited by E. Kaufmann and J. Sanchez (Wiley, NY, 2000).

[202] I. Tsatskis, "Non-mean-field theories of short range order and diffuse scattering anomalies in disordered alloys," in *Local Structure from Diffraction* (Springer US, 2002) pp. 207–231.

[203] D. A. Rowlands, J. B. Staunton, and B. L. Györffy, Phys. Rev. B **67**, 115109 (Mar 2003).

[204] The MathWorks. Inc, Natick, M. A., *MATLAB (R2008b)*.

[205] Y. Y. Li, J. Chem. Phys. **17**, 447 (1949).

[206] A. D. Beath and D. H. Ryan, Phys. Rev. B **72**, 014455 (2005).

[207] P. C. Clapp and S. C. Moss, Phys. Rev. **171**, 754 (Jul 1968).

[208] P. C. Clapp and S. C. Moss, Phys. Rev. **142**, 418 (Feb 1966).

[209] G. S. Joyce, "Critical properties of the spherical model," in *Phase Transitions and Critical Phenomena*, Vol. 2, edited by C. Domb and M. S. Green (Academic, New York, 1972) Chap. 10, pp. 375–442.

[210] R. V. Chepulskii and V. N. Bugaev, Journal of Physics: Condensed Matter **10**, 7309 (1998).

[211] V. I. Tokar and I. Tsatskis(1995), unpublished.

[212] S. Katsura, T. Morita, S. Inawashiro, T. Horiguchi, and Y. Abe, J. Math. Phys. **12**, 892 (1971).

[213] G. N. Watson, Q. J. Math. **os-10**, 266 (1939).

[214] C. F. Baillie, R. Gupta, K. A. Hawick, and G. S. Pawley, Phys. Rev. B **45**, 10438 (May 1992).

[215] R. Gupta and P. Tamayo, http://arxiv.org/abs/cond-mat/9601048v1 (1996).

[216] S. Kämmerer, B. Dünweg, K. Binder, and M. d'Onorio de Meo, Phys. Rev. B **53**, 2345 (Feb 1996).

[217] M. E. Fisher, Reports on Progress in Physics **30**, 615 (1967).

[218] V. I. Tokar and I. V. Masanskii and T. A. Grishchenko, J. Phys.: Condens. Matter **2** (1990).

[219] D. A. Biava, S. Ghosh, D. D. Johnson, W. A. Shelton, and A. V. Smirnov, Phys. Rev. B **72**, 113105 (Sep 2005).

[220] S. Ghosh, D. A. Biava, W. A. Shelton, and D. D. Johnson, Phys. Rev. B **73**, 085106 (Feb 2006).

[221] A. N. Vassiliev, *Functional Methods in Quantum Field Theory and Statistics* (Leningrad State University Press, Leningrad, 1976).